

Fredrik Rian

Hydraulic properties of the Excavation damage zone

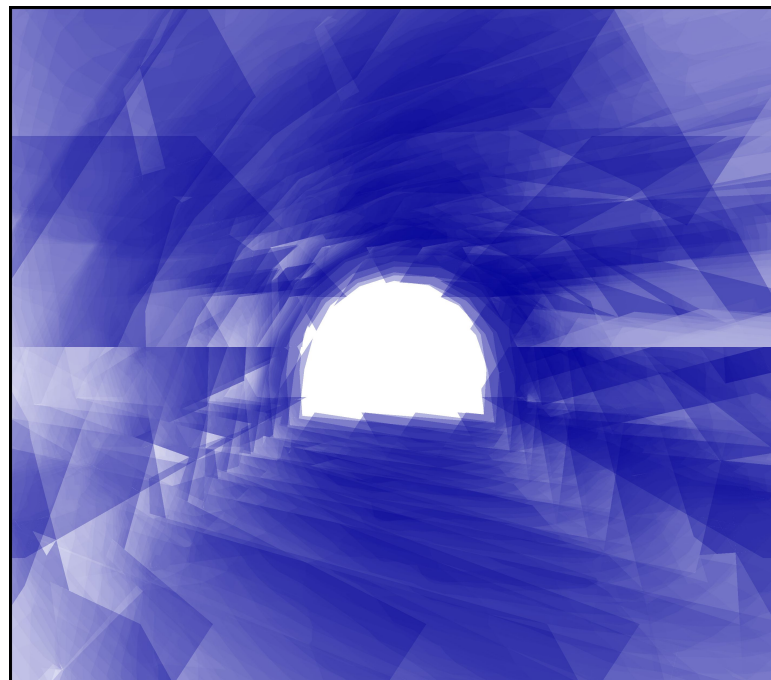
Investigations and numerical simulations of joint transmissivities, groundwater pressures and groundwater flow in the Hestnes railroad tunnel, Norway

Masteroppgave i Tekniske Geofag

Veileder: Karl Gunnar Holter

Medveileder: Eirik Nilsen

Juni 2023



Fredrik Rian

Hydraulic properties of the Excavation damage zone

Investigations and numerical simulations of joint transmissivities, groundwater pressures and groundwater flow in the Hestnes railroad tunnel, Norway

Masteroppgave i Tekniske Geofag
Veileder: Karl Gunnar Holter
Medveileder: Eirik Nilsen
Juni 2023

Norges teknisk-naturvitenskapelige universitet
Fakultet for ingeniørvitenskap
Institutt for geovitenskap og petroleum



Kunnskap for en bedre verden

Acknowledgements

This thesis marks the end of five years of education at NTNU. These years have involved a fair share of hard work and tiresome periods. During these five years, I have gained new relations I would not be without. I want to highlight my classmates, with whom we have had a fantastic study environment, especially the last two years after covid restrictions were lifted. I look forward to the future, be it social happenings or work-related.

I want to thank my parents for their unwavering support during my time as a student. You were dependable, always. I would like to thank Gunnar Vistnes and Jon Runar Drotninghaug at the rock mechanics laboratory of the Department of Geoscience and Petroleum at NTNU. You were flexible, helpful, and professional during my time at the lab. I want to thank all the site geologists working at Veidekke. You were all very helpful during my site visits. I thank co-supervisor Eirik Nilsen for valuable input to the numerical modeling and as a sparring partner for 3DEC questions.

Finally, a big thanks is sent to my supervisor Karl Gunnar Holter. A man with enormous enthusiasm and insight that inspired me to give my best in an exciting topic that I am happy to have contributed.

Abstract

This thesis investigates the hydraulic properties of the excavation damage zone (EDZ). The work includes numerical simulations of a new tunneling concept with respect to water and frost protection that is currently carried out at Hestnes railroad tunnel. The concept is to achieve a functional dry tunnel by a differentiated grouting procedure with colloidal silica in the walls and the crown, and only micro cement in the invert. The concept is that a higher degree of tightness is achieved in the zone grouted with colloidal silica, and the resulting contrast in hydraulic conductivity between the grouted zones diverts water flow towards the invert. Increased joint transmissivities in the EDZ can increase the draining effect close to the tunnel excavation and reduce groundwater pressure acting on the rock support. Because of its low hydraulic conductivity, shotcrete is planned as a sufficient water barrier for the remaining flow.

Water pressure testing was carried out to assess the joint transmissivities in the excavation damage zone in the Hestnes railroad tunnel. A review of previously conducted water pressure testing in the Gevingåsen and Drammen railroad tunnels was also conducted to investigate joint transmissivity in the EDZ. Geological mapping and 2D doorstopper stress measurements were conducted to find input parameters for a 2D FEM matrix flow analysis in RS2 and 3D DEM joint flow analysis in 3DEC. The RS2 and 3DEC analysis included the same scenarios to assess the influence of the different parts of the tunnel concept; the excavation damage zone, the grouted zone, and the shotcrete. The 3DEC model included stress-induced aperture changes only and not blasting-induced damage.

The main findings in Gevingåsen and Drammen show that the first 0.5 m from the excavation boundary have a higher frequency of high joint transmissivity than further out in the rock mass. Water pressure testing in the Hestnes project had few valid measurements in the EDZ. Difficulties with pressure build-up and leakage out of nearby holes indicate that the joints are open and conductive. The numerical results show that water flow is significantly altered towards the invert and that significantly less flow occurs where colloidal silica is used. The 3DEC model shows that stress-induced aperture changes influence fluid flow around the tunnel excavation and that joint pressures are reduced in the zone grouted with colloidal silica and the EDZ. Due to large horizontal stresses, most joints open in the walls and close towards the corners of the invert and the crown. Horizontal joints tend to open in the crown and invert. The RS2 analysis shows that the shotcrete diverts flow towards the invert and is close to impermeable. Future work should evaluate the EDZ and the influence of stress and blasting-induced changes to assess flow connectivity from the crown to the invert.

Sammendrag

Denne avhandlingen undersøker de hydrauliske egenskapene i sprengningsskadesonen. Arbeidet inkluderer numeriske modelleringer av et nytt tunnelkonsept med tanke på vann og frostsikring som utføres ved Hestnes jernbanetunnel. Konseptet går ut på å oppnå en funksjonelt tørr tunnel ved å bruke en differensiert injeksjonsprosedyre med kolloidal silika og mikrosement i heng og tak, og kun mikrosement i sålen. Konseptet innebærer at man oppnår høyere grad av tetthet i sonen som injiseres med kolloidal silika og at kontrasten mellom sonen injisert med kolloidal silika og kun mikrosement fører til at grunnvannsstrømmen reduseres i heng og tak og ledes mot sålen. Økt hydraulisk transmissivitet i sprekker i sprengningsskadesonen kan øke vanddrenering og redusere vanntrykket på sprøytebetongen som er utført som en del av bergsikringen. Sprøytebetongen er planlagt som eneste form for vannsikring på grunn av dens lave hydrauliske konduktivitet.

Vanntapsmålinger ble utført i Hestnes jernbanetunnel for å undersøke sprekke-transmissiviteten i sprengningsskadesonen. Sprekke-transmissivitet ble også undersøkt i tidligere utført vanntapsmålinger i to tunnelprosjekter: Gevingåsen og Drammen. I Hestnesstunnelen ble det utført geologisk fertkartlegging og 2D-doorstopper spenningsmålinger for å finne inngangsparametere for en 2D FEM vannstrømningsanalyse i RS2 og 3D DEM vannstrømningsanalyse på sprekker i 3DEC. De numeriske analysene inkluderte de samme scenariene for å undersøke effekten på grunnvannsstrømning og vanntrykk for tunnelkonseptet; sprengningsskadesonen, injisert sone og sprøytebetong. 3DEC modellen inneholdt kun spenningsinduserte sprekkeåpningsforandringer.

Hovedfunnene i Gevingåsen og Drammen prosjektene viser at de første 0.5 m i sprengningsskadesonen har en høyere frekvens av høy-transmissive sprekker. Vanntapsmålingene i Hestnesprosjektet hadde få gyldige målinger i sprengningsskadesonen, vanskeligheter med trykkoppbygging og lekkasjer ut av nabohull tyder på at sprekke i sprengningsskadesonen er åpne og har stor transmissivitet. De numeriske simuleringene viser at grunnvannstrømning blir betraktelig redusert i sone injisert med kolloidal silika og vannet ledes mot sålen og at grunnvannstrykket reduseres i sone injisert med kolloidal silika og i sprengningsskadesonen. På grunn av høye horisontale spenninger så åpner sprekke mest i vegg og lukkes i såle og tak generelt sett. Det horisontale sprekkesettet åpner i heng og såle. RS2 analysen viser at intakt sprøytebetong er nærmest impermeabel og leder vann mot sålen. For å videre verifisere tunnelkonseptet må framtidige undersøkelser se om vannstrømning fra heng til såle er sammenkoblet for både spenning- og sprengningsinduserte forandringer i sprengningsskadesonen.

Contents

Figures	VIII
Tables	VIII
1 Introduction	1
1.1 Background	1
1.2 Research objectives	2
1.3 Scope	3
1.4 Limitations of scope	4
1.5 Outline and structure of this thesis	5
2 Working Method	6
2.1 Technical background and general theory	6
2.2 Review of previous investigations	7
2.3 Field work	7
2.4 Laboratory work	7
2.5 Numerical simulations	8
3 Technical background: the concept of a drained and functionally dry tunnel	9
3.1 Conceptual tunnel model	9
3.2 Tunnels as draining structures	10
3.3 Traditional water and frost protection in road and railroad tunnels	11
3.3.1 Cast-in-place concrete with membrane	11
3.3.2 Waterproof sprayed concrete lining	12
3.3.3 Shield structures	13
3.4 Grouting materials	14
3.5 Shotcrete properties: water transport and durability	15
4 General theory and background	17
4.1 Water flow in rock	17
4.1.1 Water flow in joints	17
4.1.2 Influence of rock type on water flow	19
4.1.3 Analytical solutions for calculating water inflow in tunnels	19
4.2 Water pressure testing	20
4.2.1 Estimating transmissivity from water pressure testing	20
4.3 Mechanical behavior of rock	21
4.3.1 Isotropic elastic model	21
4.4 Constitutive models for rock failure and joint slip	22

4.4.1	Mohr-Coloumb	23
4.4.2	Barton-Bandis criterion	23
4.4.3	Residual friction angle and basic friction angle	24
4.4.4	Joint normal and shear stiffness	25
4.5	Q-system	27
4.6	Excavation damaged zone	28
4.6.1	Stress-induced excavation damage	29
4.6.2	Construction induced damage	29
4.6.3	Hydraulic properties of the EDZ	29
4.7	Numerical methods	31
4.7.1	Finite element method	31
4.7.2	Distinct element method	32
4.7.3	3DEC	32
4.8	Statistical description of joint transmissivity	32
4.8.1	General statistical terms	33
4.8.2	Cumulative distribution function diagram	33
4.8.3	Pareto distribution	33
4.9	Summary and discussion of theory and background	34
5	Case study description: Hestnes railroad tunnel	35
5.1	Rock mass description	35
5.2	Tunnel design with respect to water and frost protection	36
5.3	Grouting procedure at Hestnes tunnel	37
5.4	Expected tightness	37
6	Review of previous investigations	39
6.1	Review of WPT data in Gevingåsen and Drammen	39
6.2	Review of in-situ stress measurements at the Ulvintunnel by Pöyry	39
7	Executed work	41
8	Field work	42
8.1	Rock mass description	42
8.1.1	Rock mass quality	44
8.2	Joint mapping	45
8.2.1	Joint orientations	45
8.3	JRC and JCS investigations	51
8.3.1	Joint roughness number (JRC)	51
8.3.2	Joint wall compressive strength (JCS)	54
8.4	Rock core extraction and water pressure testing	58

8.4.1	Rock core drilling	58
8.4.2	Water pressure testing	58
9	Laboratory work	60
9.1	Rock core-logging of the Drammen and Gevingnåsen projects	60
9.2	Rock core-logging of the Hestnes Project	60
9.3	Transmissivity estimations	61
9.4	Method - Rock mechanical testing	61
9.4.1	Specimen preparation	61
9.4.2	UCS-testing	63
9.4.3	Tilt-testing	64
10	Analysis and results from field and laboratory investigations	66
10.1	Results of corelogging	66
10.1.1	Transmissivity and aperture distribution	66
10.2	Results in the Hestnes project: transmissivity and aperture estimations .	68
10.3	Results from rock mechanical testing	70
10.3.1	UCS-testing	70
10.3.2	Tilt testing	70
10.4	Joint properties estimation	73
10.4.1	Residual friction angle	73
10.5	Discussion of joint transmissivity in Gevingåsen, Drammen, and Hestnes	74
10.6	Discussion of lab results: rock mechanical properties	75
10.7	Conclusions regarding rock joint transmissivities and rock mechanical properties	76
11	Numerical simulations	77
11.1	Analysis of in-situ stress and fluid flow in RS2	77
11.2	Back-calculating of insitu-stress	77
11.2.1	Method	77
11.2.2	Influence of topography	78
11.2.3	Input parameters and assumptions	78
11.2.4	Geometry and boundary conditions	78
11.3	Fluid flow model	79
11.3.1	Flow scenarios	80
11.3.2	Geometry and boundary conditions	80
11.3.3	Analytical prediction of water inflow and hydraulic conductivity	80
11.3.4	Input parameters and assumptions	82
11.4	Results of in-situ stress back calculating	84
11.5	Results of fluid flow analysis	84

11.6	Discussion of in-situ stress analysis	88
11.7	Discussion of flow analysis	88
11.8	Conclusions regarding in-situ stress and flow analysis	89
11.9	3DEC setup	90
11.9.1	Model scenarios	90
11.9.2	Geometry and model size	90
11.9.3	Mesh setup	90
11.9.4	Joint representation	91
11.9.5	Mechanical and flow boundary conditions	92
11.9.6	In-situ stress	93
11.9.7	Rock mechanical properties	94
11.9.8	Joint mechanical properties	94
11.9.9	Rock support	95
11.9.10	Hydraulic apertures in the model	96
11.9.11	Hydromechanical coupling	97
11.9.12	Simulation stages	98
11.9.13	Model optimizations	98
11.10	3DEC results	99
11.11	Results scenario 1: Stress-induced EDZ in gneiss	100
11.12	Results scenario 2: Homogenous gneiss with grouted zone	105
11.13	Results scenario 3: Homogenous gneiss with grouted zone and impermeable shotcrete	107
12	Discussion	109
12.1	Validity of joint properties	109
12.2	Implementation of the grouted zone	110
12.3	Implementation of the EDZ	110
12.4	Comparison between RS2 and 3DEC analysis	111
12.5	Stress-induced aperture and joint pressure changes in the EDZ	111
12.6	Numerical simulations versus in-situ measurements in the EDZ	112
12.7	Evaluation of the findings concerning the tunnel concept	112
12.8	Verification of conceptual model	114
13	Limitations	116
14	Conclusions	117
15	Recommendations for future work	119
	Appendix	127

A	IN-SITU STRESS MEASUREMENTS BY PÖYRY	127
B	FIELD MAPPING RESULTS	128
C	CORE LOGGING GEVINGÅSEN	129
D	CORE LOGGING DRAMMEN	134
E	CORE LOGGING HESTNES	140
F	LABORATORY RESULTS - ROCK MECHANICAL TESTING	148

List of Figures

3.1	Functional dry tunnel concept	10
3.2	Conceptual view of different water protection systems.	11
3.3	Cast-in-place concrete with waterproof membrane	12
3.4	Sprayed concrete lining with embedded waterproof membrane	13
3.5	Water and frost protection solutions in road tunnels with low and intermediate traffic levels	14
3.6	Conceptual water transport through shotcrete lining in a tunnel.	16
4.1	Categorization of different zones in the EDZ	28
4.2	Section transmissivity plotted against depth for mapped joints	31
5.1	Overview of KS-1 Hestnes tunnel	35
5.2	Rock types at the construction site	36
8.1	Amphibolite with a dyke-like appearance in the gneiss	43
8.2	Strongly tectonized vertical amphibolite dyke	43
8.3	Joint pole plot for the measured joint orientations.	47
8.4	Joint rosette	47
8.5	Examples of mapped joint sets	48
8.6	J2 joint set visible in the gneiss	48
8.7	Example of joints from surface mapping	49
8.8	Foliation in amphibolite	49
8.9	Example of sub-horizontal joint set j3	50
8.10	Surface joint mapping examples	50
8.11	Steel profilometer that was used to measure JRC. Length is 15 cm.	52
8.12	Combined JRC values for measurements in both rock types	53
8.13	JRC values for the measurements taken in the gneiss	53
8.14	JRC values for the measurements taken in the amphibolite	53
8.15	JCS measurements	55
8.16	Normalized schmidthammer values	57
8.17	WPT equipment setup (SINTEF 2023)	59
8.18	Coredrilling and packer setup.	59
9.1	Borehole 2 from field investigations in the Hestnes project	60
9.2	Prepared gneiss cores	62
9.3	Prepared amphibolite cores	62
9.4	GCTS RTR-4000 testing apparatus used in the UCS testing.	65
9.5	Tilt testing setup.	65
10.1	Example of blasting damage in two boreholes and corresponding cores.	66
10.2	Scatterplot of transmissivity data in the Hestnes, Gevingåsen, and Drammen projects.	67

10.3	Scatterplot of estimated hydraulic aperture in the Hestnes, Gevingåsen, and Drammen projects.	68
10.4	Pareto distribution for estimated joint transmissivities in the amphibolite.	69
10.5	Stress-strain curves for the different rock cores belonging to gneiss, from the uniaxial compressive test.	71
10.6	Stress-strain curves for the different rock cores belonging to amphibolite, from the uniaxial compressive test.	72
10.7	Yielded cores in the gneiss after UCS-testing.	72
10.8	Yielded cores in the amphibolite after UCS-testing.	73
11.1	RS2 model setup. Scale in meters.	79
11.2	RS3 model for scenario 3 showing zones with different hydraulic conductivities.	83
11.3	RS2 stress analysis result. Scale in meters.	84
11.4	Pore pressure distribution for scenario 1 in RS2.	85
11.5	Total head and flowlines with discharge in invert for scenario 1 in RS2.	85
11.6	Pore pressure distribution for scenario 2 in RS2.	86
11.7	Total head and flowlines with discharge in invert for scenario 2 in RS2.	86
11.8	Pore pressure distribution for scenario 3 in RS2.	87
11.9	Total head and flowlines with discharge in invert for scenario 3 in RS2.	87
11.10	Geometry of the 3DEC model with mesh. Scale in meters.	91
11.11	Fluid boundary conditions	93
11.12	Grouted zones in the 3DEC model before excavation.	97
11.13	Sigma 1 stress distribution for scenario 1.	101
11.14	Displacement for scenario 1	101
11.15	Ortopgraphic view of hydraulic apertures close to the excavation for scenario 1.	102
11.16	Perspective view of hydraulic apertures for scenario 1.	102
11.17	Crossection of hydraulic apertures for scenario 1.	103
11.18	Ortopgraphic view of joint pressures for scenario 1.	103
11.19	Cross-section of joint pressures for scenario 1.	104
11.20	Discharge illustrated as lines for scenario 1.	104
11.21	Ortopgraphic view of the joint pore pressures in Scenario 2.	105
11.22	Cross-sectional view of joint pressure for scenario 2	106
11.23	Discharge illustrated as lines for scenario 2.	106
11.24	Ortopgraphic of the joint pore pressures in Scenario 3.	107
11.25	Cross-section of joint pressures for scenario 3.	108
11.26	Discharge illustrated as lines for scenario 3.	108

12.1 Comparison of the tunnel concept and the numerical results	115
---	-----

List of Tables

4.1 Analytical solutions for inflow.	20
6.1 Estimations of horizontal and vertical stress, from Pöyry.	40
7.1 Overview of the main parts of the executed work	41
8.1 Mapped Q-values at the Hestnes tunnel site.	45
8.2 Joint orientations.	46
8.3 Rebound values.	56
8.4 Adjusted rebound values and calculated JCS values.	56
9.1 Descriptives of test specimens used in UCS testing and tilt-testing . . .	63
10.1 Transmissivity and aperture estimations for The Hestnes project in the EDZ	68
10.2 Transmissivity distribution Hestnes.	69
10.3 Results of the tilt-testing	70
10.4 UCS-testing results.	71
10.5 Residual friction angle.	74
11.1 Stress measurements at Hestnes.	77
11.2 Input parameters used in the RS2 model.	79
11.3 Predicted inflow.	81
11.4 Different hydraulic conductivity and the equivalent aperture for differ- ent zones in the RS2 model	82
11.5 In-situ stress.	94
11.6 Rock mechanical properties.	94
11.7 Estimated joint parameters for the Gneiss.	95
11.8 Estimated joint parameters for the Amphibolite.	95
11.9 Rock support parameters and source.	96
B.1 Table of all JRC values from field investigations.	128
F.1 Results from the tilt testing	148

Nomenclature

ΔH	Change in pressure head	m
δ	Skin factor	
μ	Viscosity of water	Pa s
ϕ	Friction angle	
ϕ_b	Basic friction angle	
ϕ_r	Residual friction angle	
ρ	Density	g/cm ³
σ_1	Maximum principal stress	Pa
σ_2	Intermediate principal stress	Pa
σ_3	Minimum principal stress	Pa
σ_H	Maximum horizontal stress	Pa
σ_h	Minimum horizontal stress	Pa
σ_n	Normal stress	Pa
σ_v	Vertical stress	Pa
τ	Rock joint shear strength	Pa
c	Cohesion	Pa
<i>CDZ</i>	Construction damage zone	
<i>CS</i>	Colloidal silica	
<i>DEM</i>	Distinct element method	
E	Physical aperture	m
E	Young's modulus	GPa
e	Hydraulic aperture	m
<i>EDZ</i>	Excavation damage zone	
<i>FEM</i>	Finite element method	
G	Shear modulus	GPa
g	Acceleration due to gravity	9.81 m/s ²
H	Tunnel depth	m
<i>ISRM</i>	International Society for Rock Mechanics	
J_a	Joint alteration number	
J_n	Joint set number	

J_r	Joint roughness number	
J_w	Joint water reduction factor	
K	Hydraulic Conductivity	m/s
K_g	Conductivity the grouted zone	m/s
K_n	Joint normal stiffness	GPa/m
K_s	Joint shear stiffness	GPa/m
K_{bulk}	Bulk modulus	GPa
$K_{n(mism.)}$	Mismatched joint shear stiffness	GPa/m
L	Length	m
MC	Micro cement	
PEG	Pre-excavation grouting	
Q	Q-value	
r_t	Tunnel radius	m
RQD	Rock Quality Designation	
S	Mean joint spacing	m
SRF	Stress Reduction Factor	
T	Transmissivity	m ² /s
t	Thickness of the grouted zone	m
UCS	Uniaxial compressive strength	Pa
WPT	Water pressure testing	

1 Introduction

1.1 Background

The primary purpose of this thesis is to investigate the hydraulic properties of the excavation damage zone (EDZ). The context which is investigated in this study is blast-excavated tunnels in hard rock. The main goal of this study is to increase the knowledge of the effects of the EDZ on water inflow, in-situ groundwater pressure when a tunnel is pre-grouted with the requirement of achieving a functionally dry interior of the rock support surface.

Studies show that the hydraulic properties are significantly altered in EDZ and that joint transmissivity increases upto several magnitudes compared to in-situ rock (Aas 2020; Ericsson et al. 2015; Martino and Chandler 2004). The effect the EDZ has on hydraulic properties is important because increased hydraulic conductivity in the EDZ can reduce the groundwater pressure acting on elements such as water- and frost protection or rock support in partially drained or drained tunnels (Holter 2015). Hestnes railroad tunnel, currently under construction, aims to achieve a functional dry tunnel by pre-grouting, so the remaining inflow can be drained through the invert, and traditional water and frost protection is not necessary.

The Hestnes project utilizes colloidal silica, a low-viscous grout material that has proven effective in sealing finer apertures than cement-based based grout (Boden and Sievaenen 2005; Funehag 2008; Hölttä et al. 2008; Krokedal 2022). The shotcrete applied in the crown and wall as part of the rock reinforcement is planned to be a sufficient water barrier for the remaining inflow. Measurements in shotcrete by Holter and Geving (2016) show that shotcrete has very low hydraulic conductivity, around 5×10^{-14} m/s.

More knowledge of hydraulic properties in the EDZ is important so innovative concepts like the one at Hestnes can succeed. The potential is significant; for Hestnes the reduction in CO₂-emission is estimated to be around 80 % and cost-reduction is estimated around 50 % compared to a full cast-in-place concrete lining water protection system (Resset 2023).

1.2 Research objectives

The overall research objective of this thesis is to assess the hydraulic properties of the excavation damage zone. The goal is to add knowledge about groundwater flow and in-situ groundwater pressures to verify a conceptual model for a functionally dry tunnel in hard rock achieved by pre-grouting. The research objective encompasses investigations of a partially drained and grouted tunnel called the Hestnes tunnel, which serves as a case study.

The overall research objective can be divided into three sub-objectives.

Objective one: investigations of the excavation damage zone

- Field and lab investigations to assess joint transmissivities and estimate hydraulic apertures in the excavation damage zone
- Numerical simulations of stress-induced aperture changes and its effect on water flow and pressure in the case study

Objective two: combined effect of EDZ and grouted zone

- Numerical simulations of the case study, which includes EDZ and grouted zone. See the effect on water flow and pressure.

Objective three: combined effect of EDZ, grouted zone, and a shotcrete layer with reduced permeability.

- Numerical simulations of the case study, which include EDZ, grouted zone, and shotcrete. See the effect on water flow and pressure.

1.3 Scope

The primary scope of this thesis is the hydraulic properties of the EDZ. The scope includes investigations of a tunnel concept on a functionally dry rock support surface achieved entirely by pre-grouting. Particular interest is given to joint transmissivity, groundwater pressures, and water flow around a tunnel for scenarios that include the EDZ, the grouted zone, and a shotcrete lining. Numerical simulations are done in RS2 (Rockscience 2021) and the distinct element method (DEM) software 3DEC, developed by Itasca (Cundall 1988).

The main case study in this thesis is a railroad tunnel called the Hestnestunnel that was under construction as the thesis was written. The work includes field and laboratory investigations to find representative values for the rock mass and the joint system. Hydraulic apertures were estimated based on joint transmissivity data from water pressure testing (WPT) conducted at the construction site. The gathered data replicates the case study in a 3D model in 3DEC. The objective of the 3D model was to investigate how the grouted zone, shotcrete, and EDZ influence joint flow and pressure around the tunnel. The same simulations were done in RS2 to have a reference scenario. Back-calculating of in-situ stress was also done in RS2.

In addition to the main case study, previously conducted water pressure tests (WPT) in two other railroad tunnels were investigated; Gevingåsen and Drammen. The invested work in these projects served as useful practice in preparation for the main case study and to investigate the hydraulic properties of the EDZ.

1.4 Limitations of scope

One of the research objectives is to investigate the combined effect of the EDZ and grouted zone. Due to tunnel excavation circumstances, the work could not include hydraulic conductivity measurements in the grouted zone. Therefore, the predicted tightness of the grouted zone is based on literature and experience in other projects when included in the numerical simulations.

Water pressure testing conducted as part of the thesis had few valid measurements close to the tunnel boundary, which is susceptible to blasting damage. Consequently, data were lacking to replicate the blasting-induced damage in the excavation zone. The numerical simulations only include stress-induced changes because of this.

Another limitation lies in the numerical software used to simulate the scenarios. In 3DEC, the rock reinforcement does not participate in the fluid flow calculations. Therefore, a permeable shotcrete lining was simulated by a discharge boundary condition, which is a compromise and not the ideal representation of the lining—very long solving times prevented experimenting with workaround solutions.

The thesis includes several comprehensive topics that would result in a very long thesis if all topics were elaborated. Consequently, the theory section and background information elaborate only on the most relevant theory. Pre-excavation grouting (PEG) is a topic from which specific elements are used as part of the thesis but not elaborated upon in the theory section because it is not the main constituent of the thesis. Aspects of the topic are consecutively explained as needed.

1.5 Outline and structure of this thesis

This thesis is divided into 14 chapters. Chapter 1 introduces the thesis. Chapter 2 includes the working method in the thesis. Chapter 3 presents the technical background of the tunnel concept. Chapter 4 presents relevant theory and background information used throughout the thesis. Chapter 5 presents the main case study; Hestnes railroad tunnel. Chapter 6 includes a review of relevant previous studies. Chapter 7 consists of an overview of the executed work. Chapter 8 includes field work. Chapter 9 includes laboratory work. Chapter 10 presents the results and analysis of field and laboratory work.

Chapter 11 presents the numerical simulations. The first sections include simulations done in RS2 on the in-situ stress and flow analysis of the case study. After this, the numerical modeling chapters include work done in 3DEC, the model's build-up, assumptions, calculations, and choices taken regarding input parameters before the results are presented. Chapters 12-14 have the thesis's final discussion, limitations, conclusions, and recommendations for future work.

2 Working Method

The executed work in this thesis includes investigations of the hydraulic properties in the EDZ and numerical simulations of a partially drained and grouted tunnel. The Hestnes railroad tunnel was chosen as an investigation case. The Hestness tunnel served as an ideal case for several reasons. First, it is the first railroad tunnel in Norway that aims to achieve a functional dry tunnel through the pre-grouting and not use the standard water- and frost protection measures, such as cast-in-place concrete with waterproof membranes or sprayed membrane solutions. Instead, the applied shotcrete is planned to be a sufficient hydrological barrier in the wall and crown, with a drained invert. Second, the tunnel was under construction when this thesis was written, allowing for back-calculating and predicting of hydrogeological properties. Another favorable aspect is that it allowed for continuous geological mapping underground on available rock surfaces that otherwise would be covered in shotcrete.

The following main topics will be presented in this study:

1. Technical background
2. General theory and background
3. Review of previous investigations
4. Field work
5. Laboratory work
6. Numerical simulations

The included work in the different topics will be described below.

2.1 Technical background and general theory

Technical background first introduces the tunnel concept that is carried out at Hestnes. After follows a presentation of water- and frost protection measures in today's railroad tunnels. Tunnels as draining structures are also reviewed. Then relevant grout materials are presented. The general theory chapter is a presentation of the theory used directly or indirectly in the work of this thesis.

2.2 Review of previous investigations

As part of the work in this thesis, relevant studies were reviewed. These include investigations of raw WPT data of the EDZ in two projects;

- Drammen: Kobbervikdalen railroad tunnel, contract UDK01, currently under construction
- Gevingåsen: Gevingås railroad tunnel, constructed 2009-2011

The data was used for core logging and joint transmissivity estimations. The review also includes in-situ measurements by Pöyry. These measurements were used to find the principal stresses in the 3D model.

2.3 Field work

The field investigations in this thesis were carried out at different locations in the Hestnes railroad tunnel in two periods. 15-17.01.2023 and 01.03-03.03.2023. The data collected in the field investigations were used for finding input parameters in the numerical model and in the analysis of the hydraulic properties of the rock mass. The investigations included rock core drilling, WPT, and geological mapping. Core drilling and WPT were carried out in collaboration with Sintef. Geological mapping was carried out to investigate the joint system, orientations, spacing, persistence, and joint surface conditions. Joint properties such as roughness (JRC), joint compressive strength (JCS), and general rock mass properties were also mapped.

2.4 Laboratory work

All the laboratory work was carried out at the rock mechanics laboratory of the Department of Geoscience and Petroleum at NTNU. Laboratory investigations were carried out mainly because of two reasons. First, examine the joint transmissivities of the EDZ in three different tunneling projects; Drammen, Gevingåsen, and Hestnes. Rock cores were logged and coupled to WPT data to estimate transmissivity and joint aperture for individual joints. The last part of the laboratory investigations was conducted to find input parameters in the numerical model for the rock types at the Hestnes site. Properties of intact rock were found through uniaxial compressive testing, and the basic frictional properties of the joint were found through tilt testing. Two rock types were tested. A gneiss and amphibolite.

2.5 Numerical simulations

The field and laboratory investigations' results were used to find input parameters in the numerical models. A distinct element software called 3DEC was used to simulate joint water flow. 3DEC was used because the software can fully simulate hydromechanical coupling between the rock and fluid flow. A 3D model was considered the most appropriate because of the non-symmetry of the joints and flow directions. A simplified analysis of the scenarios was done in RS2 and also back-calculating of in-situ stress. The stress-induced excavation damage and its influence on joint pressure were investigated for different scenarios that included a non-grouted tunnel, grouted tunnel, and also grouted tunnel with shotcrete with reduced permeability. Shotcrete permeability was set to zero because software limitations did not allow rock reinforcements to participate in the flow calculations.

3 Technical background: the concept of a drained and functionally dry tunnel

This chapter aims to present the background of the concept of a functionally dry tunnel in relation to the case study, Hestnes railroad tunnel. First, the tunnel concept is elaborated. Then tunnels as draining structures and traditional water- and frost protection measures are reviewed, followed by a brief introduction of grout material. Shotcrete properties in terms of water transport and durability are elaborated last.

3.1 Conceptual tunnel model

The concept of a drained and functional dry tunnel is illustrated in figure 3.1 and is based on the injecting procedure at Hestnes (Holter and Strømsvik 2023). The concept includes a differentiated grouting procedure with colloidal silica (CS), micro cement (MC) in the walls and crown, and MC in the invert. Since CS can grout finer joint apertures than MC, the zone grouted with CS has lower hydraulic transmissivity than the MC grouted zone, and inflow is reduced in the walls and the crown. The contrast in hydraulic transmissivity between the two zones diverts flow through the invert. The EDZ near the excavation has larger hydraulic transmissivities because of stress and blasting-induced damage. The increased hydraulic transmissivity in the EDZ increases the draining of water towards the invert. Shotcrete applied as part of permanent rock support has low hydraulic conductivity and acts as a water barrier for remaining inflow.

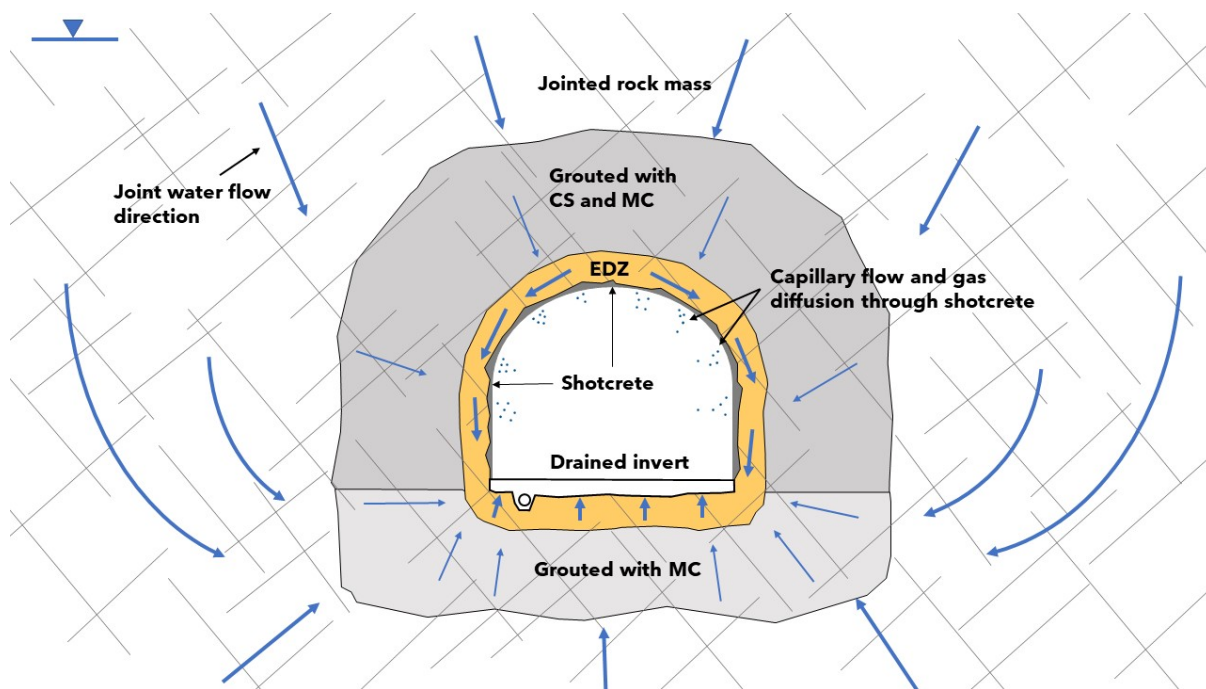


Figure 3.1: Concept of a functional dry tunnel, with a drained invert and a grouted zone around the tunnel. The invert is grouted with MC, and the walls and the crown are grouted with CS and MC. Shotcrete as part of rock reinforcement is planned to be a sufficient water barrier for the remaining inflow. Increased hydraulic transmissivity in the EDZ increases drainage towards the invert. The blue arrows show joint water flow; thickness indicates flow magnitude. CS = colloidal silica, MC = micro cement.

3.2 Tunnels as draining structures

Excavating structures underground allows water to be drained into the now exposed free surface. Water drawdown is unwanted for both external and internal consequences. Water control usually starts with pre-grouting excavating (PEG) of the rock mass. In the case of modern railroad tunnels, it is required to have water- and frost protection (BaneNOR 2022). The solutions can be either drained, undrained, or partially drained. In a drained structure, the water protection is drained so that the hydrostatic pressure is reduced. The opposite is undrained, where full hydrostatic pressure acts on the water protection system. In a partially drained system, the wall and crown can be undrained, and the invert drained. A conceptual view of tunnels as draining structures can be seen in figure 3.2.

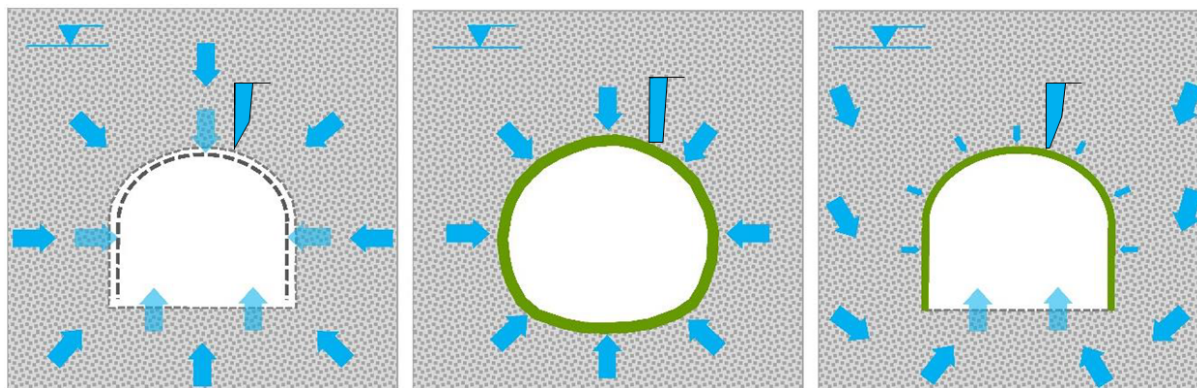


Figure 3.2: Figure shows a conceptual view of how different water protection influences water flow and groundwater pressure. From the left; a drained tunnel, an undrained tunnel, and a partially drained tunnel. After Holter (2015).

3.3 Traditional water and frost protection in road and railroad tunnels

Road and railroad tunnels in Norway must have a water protection structure to protect the traffic area from water leakage and ice formation. The design must be waterproof and lead water to a frost-secure draining system. The structure must cover the entire length of the tunnel at the whole cross-section of the tunnel, with the exception being the invert (BaneNOR 2022; NRA 2022).

There are different requirements for roads and railroads. Bane NOR allows only the following water- and frost-protection structures (BaneNOR 2022).

1. Cast-in-place concrete with lining
2. Waterproof sprayed concrete lining (SCL)

As an alternative measure, PEG can also be performed so that water- and frost protection is only needed above the rail tracks and around technical installations.

3.3.1 Cast-in-place concrete with membrane

Cast-in-place concrete solutions have a waterproof membrane and a geotextile cladded outside the concrete slabs. The geotextile drains the structure. The structure is constructed with no air gaps. Between the permanent rock support layer of shotcrete and the membrane, another layer of shotcrete is installed to ensure a smooth surface for the membrane. Figure 3.3 shows a conceptual view of the structure.

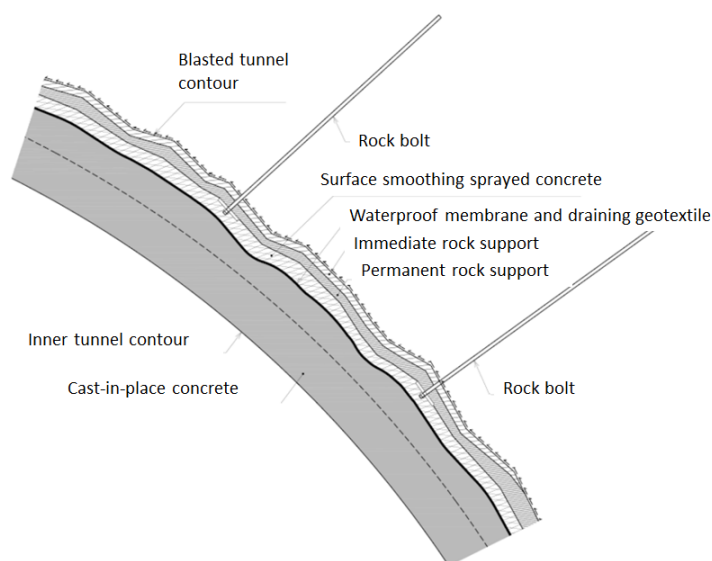


Figure 3.3: Cast-in-place concrete with waterproof membrane and geogrid. Translated and obtained from BaneNOR (2022)

3.3.2 Waterproof sprayed concrete lining

Using a waterproof SCL as a part of the rock support and water protection is a concept that has gained popularity and seen more use since 2000 (Holter 2015). Instead of having a separate layer of water protection, a waterproof membrane is sprayed on as a layer in the shotcrete. The membrane is elastic and can deform together with the SCL. Similar to the cast-in-place solution, a smoothing layer of shotcrete is required to ensure an even surface for the membrane. A conceptual view can be seen in figure 3.4. The system is undrained unless the invert is drained.

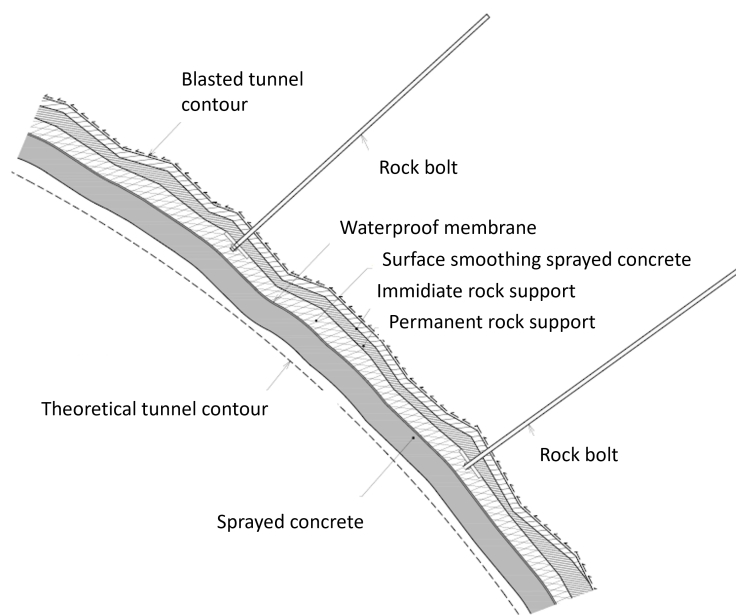


Figure 3.4: Sprayed concrete lining with embedded waterproof membrane. Translated and obtained from BaneNOR (2022)

3.3.3 Shield structures

The shield structure is a water and frost protection system for low to medium-traffic density road tunnels. Shield structures are completely drained. It is not one of the allowed solutions for railroad tunnels (BaneNOR 2022), but dispensations can be given for specific projects (Holter et al. 2013). As seen in figure 3.5 the structures can either be thermally insulated cast-in-place concrete elements or thermal insulation with a PE-sheet covered with shotcrete. The shield structure is an inner shell that catches water and drains it towards the invert. The shield structures only have a waterproofing function and are not part of the rock reinforcement (Holter et al. 2013).

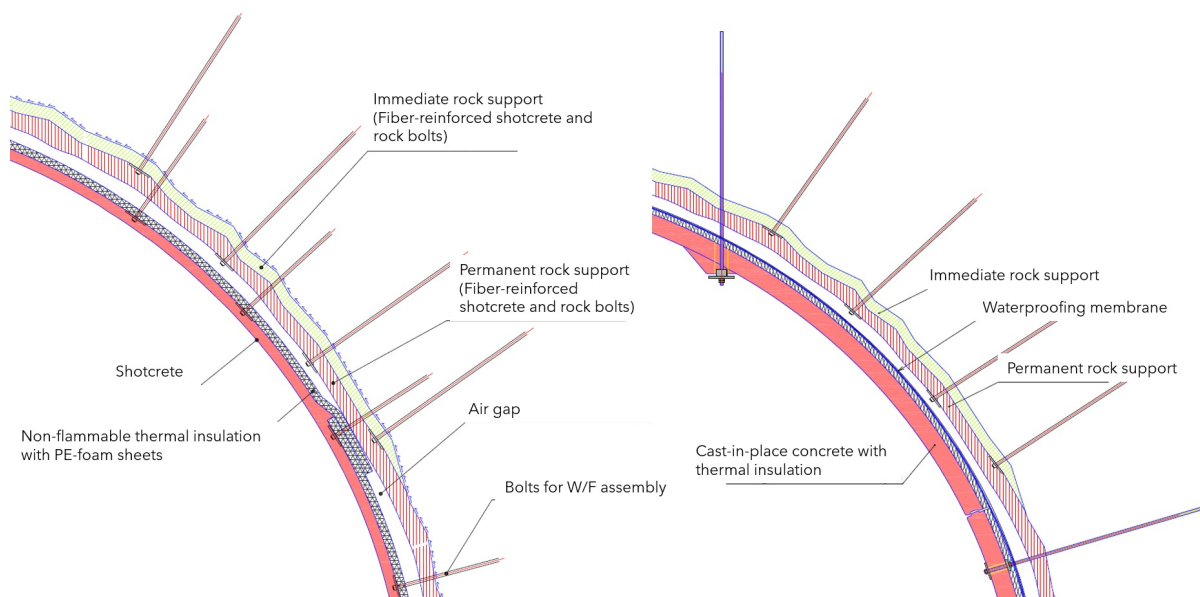


Figure 3.5: Water and frost protection solutions in road tunnels with low and medium traffic density. After NRA (2012).

3.4 Grouting materials

PEG is a procedure where grout material is injected into the rock mass ahead of the excavation face to seal water-bearing joints. The grouting materials can generally be categorized into cement-based or non-cement-based materials. The choice of grouting material depends on the inflow requirements and functional requirements. Cement-based grout is the most common (Hognestad et al. 2010). Cement-based materials can be sorted from industry cement to micro and ultrafine cement. The penetrability decreases with increased coarseness, and finer cement is required for grouting finer apertures. Categorization is usually done by grain size, d_{95} . Industry cement is defined by $d_{95} > 25 \mu\text{m}$, microfine $d_{95} < 25 \mu\text{m}$, and ultrafine $d_{95} < 13 \mu\text{m}$ (NRA 2014).

Colloidal silica (CS) is a non-cement-based low-viscosity injection material. CS consists of small particles around $0.016 \mu\text{m}$ dissolved in water and is suitable in situations with high water tightness requirements (Hognestad et al. 2010).

Accelerators can be used as an additive to the grout mixture for controlled grout curing. Controlled curing can help pressure-build towards the end of grouting and limit grouting time and material use (Hognestad et al. 2010). Alkali-free accelerators are commonly used for cement-based grout; salt water is used for colloidal silica.

3.5 Shotcrete properties: water transport and durability

For shotcrete to act as water- and frost protection, it must act as a water barrier and withstand the wear and tear from factors such as temperature changes, freeze-thaw and chemical reactions so that the lining has an acceptable service life. A view of the different processes acting in the rock-lining-free surface interface can be seen in figure 3.6.

Considering flow properties, shotcrete can, with today's technology, be considered a nearly impervious material. Water transport occurs in three different ways (Holter and Geving 2016):

- Capillary flow
- Vapor transport
- Flow through cracks in the shotcrete

Capillary flow occurs in the matrix of the shotcrete and is dependent on the pores' porosity and size. In an adequately applied shotcrete without cracks, shotcrete is close to impermeable. In testing conducted by Holter and Geving (2016), the results showed that the hydraulic conductivity of shotcrete was lower than 5×10^{-14} m/s if correctly applied and without flaws.

Vapor transport occurs regardless of the water pressure acting on the lining surface. It is, therefore, a constant transport mechanism through the shotcrete that occurs in combination with the capillary flow. The combined moisture transport by both capillary flow and vapor transport has been measured to be 3 cm³ per day for a lining thickness of 25-35 cm by Holter and Geving (2016). Vapor is believed to be the predominant transport mechanism because of the low hydraulic conductivity of shotcrete.

Flow through shotcrete can be significantly increased if cracks are formed in the shotcrete. Cracks can develop because of low quality, poor installment, or large displacements in the rock mass. The main source of seepage through the shotcrete is cracks forming due to shrinkage of the shotcrete (Holter et al. 2023).

The durability of the shotcrete is essential so that degeneration of the shotcrete due to freeze-thaw effects, temperature variations, chemical reactions, and other effects do not alter the service life beyond what is acceptable.

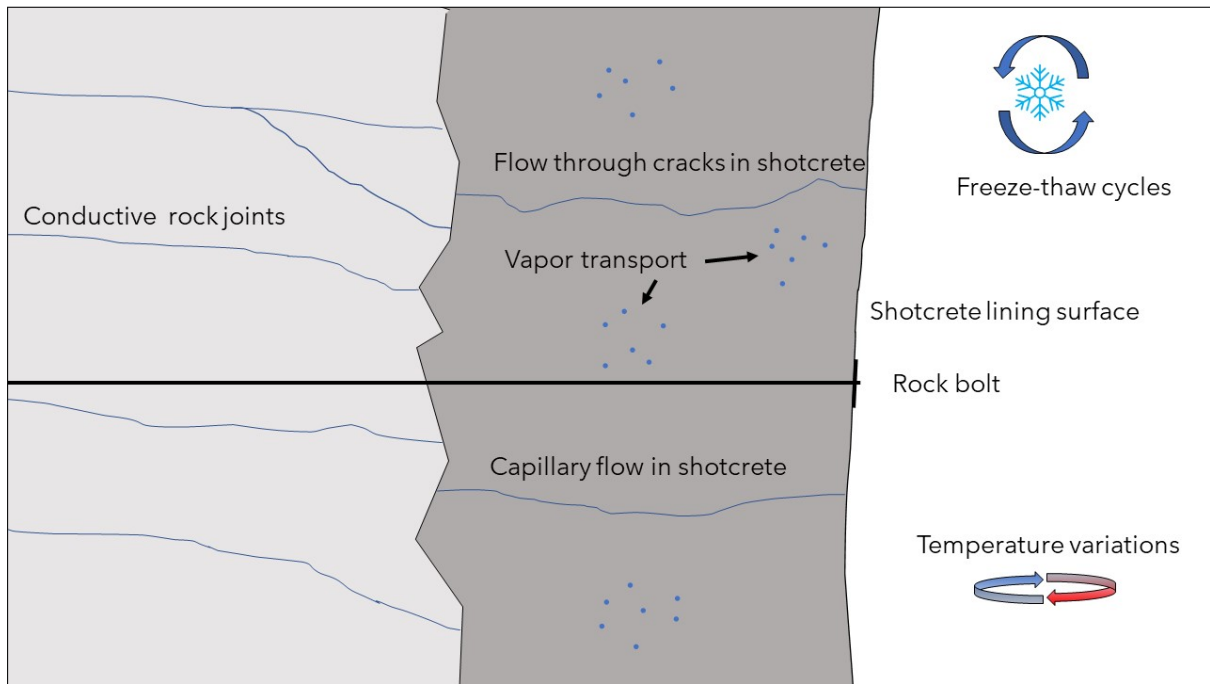


Figure 3.6: Conceptual water transport through shotcrete lining in a tunnel.

4 General theory and background

4.1 Water flow in rock

Water flow in rock can be modeled as either a matrix flow or flow on rock joints. Matrix flow depends on the porosity and how the pores interconnect, while joint flow depends on the joint properties, such as orientation, spacing, frequency, and apertures. Some sedimentary rock types have large porosity and permeability in Norway, and these are usually young and found on the continental shelf. An exception is the Brumunddal sandstone. Mainland Norway is known as a hard-rock province with nearly impermeable rock such as pre-Cambrian gneisses and metamorphic rock from the Caledonian orogeny with little porosity (Ramberg et al. 2013). Therefore, water flow in rock can be considered a function of the joint system and not the rock matrix on mainland Norway.

Darcy's law can express matrix flow through the rock. Assuming laminar flow, the specific flow through a media can be expressed as below (Darcy 1856):

$$q = -\frac{dh}{dl} \cdot K \quad (4.1)$$

According to Darcy's law, the specific flow (q) is proportional to the hydraulic gradient (dh/dl). The hydraulic conductivity is given by K (m/s). Equation 4.2 defines the water head.

$$h = \frac{P}{\rho_w g} + z \quad (4.2)$$

4.1.1 Water flow in joints

Joints often appear as planar structures with persistence much greater than the joint aperture. Because of this, joint fluid flow is usually considered between two parallel planes with a constant aperture slot. The aperture is called the hydraulic aperture (e) and is defined as the aperture that gives the mean flow of the physical aperture. This system can be solved for a Newtonian fluid with shear stress τ , shear velocity γ , density ρ , and viscosity μ . Transmissivity (T) of the rock joint can then be expressed as seen in equation 4.4.

$$T = \frac{\rho g}{\mu} \cdot \frac{e^3}{12} \quad (4.3)$$

The relationship in equation 4.4 also allows for estimations of the hydraulic aperture, e . By solving for e , the hydraulic aperture can be expressed as below:

$$e = \sqrt[3]{\frac{12\mu T_f}{\rho g}} \quad (4.4)$$

The assumption of flat planar joint surfaces is a simplification, and the actual physical aperture varies over the joint plane. In some parts, the joint planes are in contact. Zimmerman and Bodvarsson (1996) expressed the hydraulic aperture as a function of the mean physical aperture (E), the variance σ and contact area (c). This relation can be seen below in equation 4.5:

$$e^3 = E^3(1 - 1.5 \cdot \sigma^2 / E^2) \cdot (1 - 2c) \quad (4.5)$$

In a typical impermeable rock, water flows through the joints, not the matrix. The hydraulic conductivity of the rock mass is, therefore, a function of the joint system, its joint frequency, and the aperture of the joints. A common way to analyze flow in the rock mass is given by Snow (1969). In Snow's method, water flow occurs in a joint network with a constant mean joint spacing (S) for a network of perpendicular joints. The joints are assumed as smooth, planar, and parallel with a constant hydraulic aperture (e). With regards to the physical aperture, the hydraulic aperture is always bigger or close to equal due to the roughness of the natural joints (Barton and Lindström 2003). According to Snow (1969), the hydraulic conductivity of the rock mass in a 3D joint network can be expressed as:

$$k = \frac{e^3 g \rho}{6S\mu} \quad (4.6)$$

Here g (m/s^2) is the gravitational acceleration, ρ (kg/m^3) is the density of water and μ (Pa s) is the dynamic viscosity of water. The equation of Snow assumes that in a cubic joint network with a parallel flow, the water will only flow in two of the joints.

A usual assumption regarding joint fluid flow is laminar flow, which is also the assumption in the numerical model. In most cases, this can be considered a valid assumption, but the likelihood of turbulent flow grows when the joint aperture increases. Especially in joints close to tunnel contours or boreholes, the turbulent component should be considered (Gustafson and Walke 2012). Reynold's number can express

the transition from laminar to turbulent flow:

$$\frac{dh}{dl} < 13800 \cdot \frac{\mu^2}{g\rho^2b^4} \quad (4.7)$$

4.1.2 Influence of rock type on water flow

Generally, brittle rock types tend to be more jointed than soft rock, in which rock joints are more often sealed. A distinction can be made between rocks of felsic and basic origin. Felsic igneous rocks are more resilient to decomposition and weathering than basic rocks because of mineral stability. Especially quartz is one of the most stable minerals and a larger component of felsic rock compared to olivin or amphibole. Joints tend to be more open in felsic rock types than in basic rock, where joints are more likely to be filled with weathered and decomposed material. Basic rock also tends to have lower Young's modulus and higher tensile strength than felsic rock types, which are more brittle. For example, one would expect coarse-grained granite to have a higher joint transmissivity than soft phyllite. Even so, variation within the rock mass is greater than the variation between the rock types (Gustafson and Walke 2012).

4.1.3 Analytical solutions for calculating water inflow in tunnels

Estimating water inflow into tunnels is important to predict or verify water inflow, compare inflow requirements, help design decisions, or input parameters in a numerical model. The effect of grouting and corresponding inflow can also be estimated. There are several analytical solutions available for estimating water inflow into a tunnel. Table 4.1 shows some of the solutions provided by different authors: El Tani (2003), El Tani (1999), Gustafson and Walke (2012), and Karlsrud et al. (2014). Notably, El Tani (2003) provides an exact solution for inflow into a tunnel in an isotropic homogenous rock mass tunnel with a constant water head. As seen in the formulas presented in table 4.1, inflow is dependent on the radius (r), water head (h), and the hydraulic conductivity (k) of the rock mass. To estimate inflow (Q) in a tunnel with a grouted rock mass, the two solutions are given by Gustafson and Walke (2012) and Karlsrud et al. (2014). Here t is the thickness of the grouted zone, k_g is the conductivity of the grouted zone, and δ is the skin factor.

Table 4.1: Some analytical solutions for water inflow into a tunnel with constant water head. Q is given as volumetric inflow per unit length of the tunnel.

Reference	Formula	Description
Karlsruud et al. (2014)	$Q = 2\pi k \frac{h}{\ln(\frac{2h}{r}-1)}$	Non-grouted
Lei (1999)	$Q = 2\pi k \frac{h}{\ln\left(\frac{h}{r} + \sqrt{\frac{h^2}{r^2} - 1}\right)}$	Non-grouted
El Tani (1999)	$Q = 2\pi K \frac{1 - 3\left(\frac{r}{2h}\right)^2}{\left(1 - \left(\frac{r}{2h}\right)\right)^2 \left(\ln\left(\frac{2h}{r} - \frac{r}{2h}\right)\right)^2}$	Non-grouted
El Tani (2003)	$Q = 2\pi k \frac{\lambda^2 - 1}{\lambda^2 + 1} \frac{h}{\ln \lambda}, \lambda = \frac{h}{r} - \sqrt{\frac{h^2}{r^2} - 1}$	Non-grouted
Karlsruud et al. (2014)	$Q = 2\pi k_g \frac{h}{\ln\left(\frac{r+t}{r}\right)}$	Grouted
Gustafson and Walke (2012)	$Q = \frac{2\pi k h L}{\ln\left(\frac{2h}{r}\right) \left(\frac{k}{k_g}\right) \ln\left(1 + \frac{t}{r}\right) + \delta}$	Grouted

4.2 Water pressure testing

A common method used to acquire information about the hydraulic properties of rock mass is water pressure tests (WPT). Since the hydraulic system is mainly a function of the joint system, WPT is a good way to assess joints and their transmissivities. The joint apertures can then be estimated by using equation 4.4. The tests are usually performed by isolating sections with packers. Then water is pumped into the section at a constant overpressure. The measured outflow of the section is then recorded.

4.2.1 Estimating transmissivity from water pressure testing

As section 4.1 outlines, water flows primarily through the joint system. WPT can be used to estimate joint transmissivity. If large sections are used, the calculated transmissivity is a function of all the water-bearing joints of the section. If a joint has a significantly higher transmissivity than the other joints, it can be hard to distinguish since the calculated transmissivity will be the average of all the joints. If a single joint is tested, the specific joint transmissivity is found.

A common method to estimate section transmissivity in a borehole is Moye's Formula, given in equation 4.8. Another approach is suggested by Gustafson and Walke (2012) as seen in equation 4.9 is derived using other assumptions but gives nearly the same answer as Moye's equation.

$$T = \frac{Q\rho g}{2\pi\Delta p} \cdot \ln\left(1 + \frac{L}{2r_w}\right) \quad (4.8)$$

$$T = \frac{Q}{2\pi\Delta h} \cdot \ln\left(\frac{L}{r_w}\right) \quad (4.9)$$

In the case of a short transmissive joint where the conductivity is significantly higher than the surrounding rock, pressure loss can be neglected, and transmissivity can be estimated as shown in equation equation 4.10 (Gustafson and Walke 2012).

$$T = \frac{QL}{2\pi R\Delta h} \quad (4.10)$$

In the above equations, T is the transmissivity, Q is the water flow out of the borehole, L is the length of the tested section, r_w is the borehole diameter, Δh is the pressure head, ΔP is the overhead pressure and R is the joint persistence.

4.3 Mechanical behavior of rock

Rock behavior is usually described by an elastic or a plastic model for numerical purposes. Rock generally shows a linear relationship between strain and stress up to failure during compressional testing. Because of this, an elastic model is considered a good way to model rock behavior when deformation is reversible. Plastic models can be used to describe rock behavior after failure. In rock mechanics, the plastic model is generally an elastoplastic model where the rock is considered elastic until failure and plastic as further deformation occurs. In this thesis, an isotropic-elastic model is assumed. Rock failure is not expected to occur frequently in the tunnel and will be considered a function of the discontinuities.

4.3.1 Isotropic elastic model

The well-known Hooks law can be applied to describe an isotropic elastic material. The law states that the force applied to a spring object is proportional and opposite to the displacement. The law has been expanded for numerical modeling and rock material use. The law can be expressed as a combination of the volumetric and deviatoric stress tensors for an isotropic continuous medium, as shown below in equation 4.11.

$$\Delta\sigma_{ij} = 2G\Delta\epsilon_{ij} + \left(K_{bulk} - \frac{2}{3}G\right) \Delta\epsilon_{kk}\delta_{ij} \quad (4.11)$$

In the equation, new stress increments are a function of strain increments and material parameters. G is the shear modulus of the material, K_{bulk} is the bulk modulus, δ_{ij} is the kroenecker delta, where $\delta_{ij} = 1$ if $j = i$ and 0 if $j \neq i$. $\Delta\epsilon$ is the strain increment, and $\Delta\sigma_{ij}$ is the stress increment. Subtext i, j , and k refer to orthogonal vector coordinates for the tensor coordinate system ($i, j, k = 1, 2, 3$). For $i \neq j$, ij refers to the i plane with a shear vector acting in the j direction. For $i = j$, ij refers to the normal vector to the i plane. kk refers to the normal vector to the k plane.

New stress values can be obtained from the relation:

$$\Delta\sigma_{ij}^N = \sigma_{ij} + \Delta\sigma_{ij} \quad (4.12)$$

The parameters of bulk modulus, shear modulus, Poisson's ratio (ν), and Young's Modulus (E) can be expressed in relation to each other as shown in equation 4.13-4.16.

$$K_{bulk} = \frac{E}{3(1 - 2\nu)} \quad (4.13)$$

$$G = \frac{E}{2(1 + \nu)} \quad (4.14)$$

$$E = \frac{9K_{bulk}G}{3K_{bulk} + G} \quad (4.15)$$

$$\nu = \frac{3K_{bulk} - 2G}{2(3K_{bulk} + G)} \quad (4.16)$$

4.4 Constitutive models for rock failure and joint slip

An essential part of rock mechanics is to predict rock mass behavior by applying relevant constitutive models. The models are usually analytical or empirical, or a combination. Since rock mass is a heterogenous and anisotropic material, such models will always be a simplification. Therefore, the model must reflect the physical problem realistically so that results can be trusted. This is especially important in numerical modeling, where the model tries to replicate a physical problem. Many different models have been developed today. The Mohr-Coloumb and Hoek-brown criteria are well-known and established. Barton-Bandis criterion is a common model for joint slip (Barton and Choubey 1977).

4.4.1 Mohr-Coloumb

A common way to describe rock failure or joint slip is the Mohr-Coloumb criterion (MC). According to ISRM, it is a good first approximation of rock behavior when all principal stresses are compressive, and the range of the mean stresses is limited (Labuz and Zang 2012). The MC describes the conditions of how an isotropic material will fail. The criterion, shown in equation 4.17, indicates that there is a linear relationship between the shear stress (τ) on the failure plane, the cohesion (c), normal stress (σ_n), and friction angle (ϕ).

$$\tau = c + \sigma_n \tan \phi \quad (4.17)$$

MC considers the maximum and minimum principal stresses. The failure envelope can be constructed with a circle as a function of σ_1 and σ_3 . The radius is equal to the shear stress (equation 4.18), and the origin is equal to the mean stress (equation 4.19).

$$\tau_m = \frac{\sigma_1 - \sigma_3}{2} \quad (4.18)$$

$$\sigma_m = \frac{\sigma_1 + \sigma_3}{2} \quad (4.19)$$

Cohesion is simply the intercept on the τ axis and, therefore, a curve-fitting parameter. It can be seen as a function of the joint frictional properties, but its physical meaning is disputed Barton (2013). The residual value is often set to zero. The residual value of the friction angle ϕ can be found from tilt testing.

4.4.2 Barton-Bandis criterion

It has been shown that rock joint shear strength has a non-linear relationship with normal pressure (Barton 1973). This is because of the asperities in the joint plane. The roughness of the joint influences the interlocking of the joint and prevents shear movement. Increased normal stress is associated with more crushing of asperities. Thus, the joint shear strength depends on the joint's frictional properties and the strength of intact rock material. The Barton-Bandis criterion (Barton and Choubey 1977) is an empirical equation that incorporates joint roughness, joint compressive strength, and the effect of normal pressure. It is formulated as shown below in equation 4.20.

$$\tau = \sigma_n \tan \left(JRC \log \left(\frac{JCS}{\sigma_n} \right) + \phi_r \right) \quad (4.20)$$

Here τ is the rock joint shear strength, σ_n is the normal stress and JRC is the joint roughness coefficient and is usually measured with a profile gauge or as a function of joint amplitude using empirical diagrams. JCS is the joint compressive strength measured with a schmidthammer and estimated using the rebound values. For unweathered and undisturbed joint surfaces, the value is equal to the UCS values of the rock. ϕ_b is the basic friction angle, usually measured with a tilt test using sawn-off pieces.

In this thesis, parameters for the Barton-Bandis criteria will be collected in the field and estimated in the laboratory. Since Mohr-Coloumb is the constitutive joint slip model in 3DEC, cohesion and friction angle values are found by linearizing Mohr-Coloumb. The procedure given by Hoek (2000) will be used.

4.4.3 Residual friction angle and basic friction angle

After post-peak shear strength in the joint is reached, asperities in the joint are gradually crushed because of the shearing and displacement involved, and eventually, the roughness (i.e., JRC) will reach zero. Thus, the frictional angle at zero roughness can be defined as the residual friction angle (Barton 1982). The value is important when modeling the joint behavior before and after shear failure, and it can be found by performing in-situ or laboratory testing on joint surfaces. The common approach is to approximate ϕ_r using the empirical relation in equation 4.21 by Barton and Choubey (1977).

$$\phi_r = 20 + r/R(20 - \phi_b) \quad (4.21)$$

Where:

R = Is the rebound value of a schmidthammer on an unweathered joint surface

r = Is the rebound value of a schmidthammer on a weathered joint surface

ϕ_b = Basic friction angle

The basic friction angle can be found by tilt-testing on sawn fresh rock surfaces in the laboratory. Theoretically, the roughness should be zero along the surface so that the measured sliding angle is only a function of the mineralogic properties of the rock type (Li et al. 2019). Since UCS testing is often done parallel to tilt testing, a natural way

to measure the basic friction angle is to use the rock cores from UCS testing. Using the three-core method, the basic friction angle can be estimated by the equation 4.22, given by (Li et al. 2019).

$$\phi_b = \arctan(0.866 \tan \alpha) \quad (4.22)$$

α is in the above equation the tilt angle.

4.4.4 Joint normal and shear stiffness

Joint shear and normal stiffness are necessary parameters to predict joint displacement. There are no established guidelines to find these parameters in the literature, and several methods are available. Kulatilake et al. (2016) defines joint normal stiffness (K_n) and joint shear stiffness (K_s) as the ratio of normal (σ) and shear stress (τ) acting on a joint with respect to normal (u) and shear (v) deformation. The relationship is non-linear and can therefore be expressed as in equation 4.23 and 4.24 below.

$$d\sigma = K_n du \quad (4.23)$$

$$d\tau = K_s dv \quad (4.24)$$

Bandis et al. (1983) found that a hyperbolic function correlates to experimental data to estimate K_n and K_s . Two input parameters are required to fit the hyperbolic curve; initial normal joint stiffness and maximum joint closure. Kulatilake et al. (2016) suggests that K_n and K_s can be estimated by comparing laboratory results from axial and shear stress testing and displacement of intact and jointed rock specimens.

Joint normal stiffness can also be estimated by assuming that deformation in the rock mass is the sum of the deformation of intact rock and the joints in the rock mass. The solution is presented in equation 4.25, from Barton (1972).

$$k_n = \frac{E_i E_{rm}}{L(E_i - E_{rm})} \quad (4.25)$$

Here, k_n is the joint normal stiffness. E_i and E_{rm} are Young's modulus of intact rock and rock mass. L is the mean joint spacing. Analogous to equation 4.25, joint shear stiffness can be expressed by equation 4.26.

$$k_s = \frac{G_i G_{rm}}{L(G_i - G_{rm})} \quad (4.26)$$

K_s is joint shear stiffness, and G_i and G_{rm} are the shear modulus of intact rock and rock mass.

Based on laboratory experiments of shear and normal displacements of joints, Barton (1972) formulated empirical relations, which are presented below in equation 4.27-4.31. Here k_{ni} is the initial joint normal stiffness. V_m is the average maximum closure of joints. a_j is the average aperture thickness. Equation 4.30 shows a relation between interlocked and mismatched joint normal stiffness.

$$k_n = k_{ni} \left(1 - \frac{\sigma_n}{V_m k_{ni} + \sigma_n} \right)^{-2} \quad (4.27)$$

$$V_m = -0.2960 - 0.0056JRC - 0.2450 \left(\frac{JCS}{a_j} \right)^{-0.2450} \quad (4.28)$$

$$k_{ni} = -7.15 + 1.76JRC + 0.02 \left(\frac{JCS}{a_j} \right) \quad (4.29)$$

$$\frac{k_{n(int.)}}{k_{n(mism.)}} \approx 2 + \frac{JRC \cdot JCS \cdot \sigma_n}{2500} \quad (4.30)$$

$$a_j = \frac{JRC}{5} (0.2 \frac{\sigma_c}{JCS} - 1) \quad (4.31)$$

Barton and Choubey (1977) suggest that equation 4.32 can be used to estimate joint shear stiffness (K_s). The equation is based on a rule of thumb that says peak shear strength is reached when shear displacement is approximate 1 % of the joint length (L). L has an upper boundary value called the critical joint length (L_c). This is the mean joint spacing of cross joints.

$$k_s = \frac{100}{L} \sigma_n \tan \left(JRC \log \left(\frac{JCS}{\sigma_n} + \phi_r \right) \right) \quad (4.32)$$

For the 3DEC model, equation 4.27-4.32 will be used to find the input parameters for shear and normal joint stiffness.

Also, for numerical purposes, Itasca advises that joint normal and shear stiffness is not greater than ten times the equivalent stiffness of adjacent zones. The below equation will be used to verify this.

$$k_n < 10 \left(\max \left(\frac{K_{bulk} + 4/3G}{\Delta z_{min}} \right) \right) \quad (4.33)$$

4.5 Q-system

Rock mass classification systems enable the geologist to quickly assess the quality of the rock mass by simple inspection and easy-to-measure parameters. Based on the classifications, design decisions can be made by correlating classifications with designs in previous projects. In this thesis, the Q-system will be used.

The Q-system was first introduced by (Barton et al. 1974) and is a popular rock mass classification system in Norway. The Norwegian Geotechnical Institute (NGI) is responsible for the system. It has seen continuous revisions over the years, last updated in 2002, including now a database of over 2000 tunnels. The latest updates have incorporated new advances in rock support, such as concrete arches and energy absorption.

The three most important factors for rock mass quality are the degree of fracturing, the frictional properties of the joints, and the stress situation. The Q-system consists of 6 parameters that, when combined, give the Q-value, which is a numerical value that ranges from 0.001 to 1000. The equation can be seen in equation 4.34.

$$Q = \frac{RQD}{J_n} \cdot \frac{J_r}{J_a} \cdot \frac{J_w}{SRF} \quad (4.34)$$

where;

RQD = Rock quality designation

J_n = Joint set number

J_r = Joint roughness number

J_a = Joint alteration number

J_w = Joint water number

SRF = Stress reduction factor

Each fraction in the equation expresses the three main components crucial for underground excavation stability.

$\frac{RQD}{J_n}$ = Degree of fracturing

$$\frac{J_r}{J_a} = \text{Frictional properties of the joint}$$

$$\frac{SRF}{J_w} = \text{Stress situation}$$

To find the recommended rock support, the span of the excavation and the excavation support ratio can be used together with the Q-value in the diagram given by NGI (2022). The rock support diagram is empirical and based on previous projects.

4.6 Excavation damaged zone

The rock mass surrounding an underground excavation is adversely affected by the excavation; this zone is called the excavation damage zone (EDZ). According to Tsang et al. (2005), the EDZ can be defined as a “zone in which hydromechanical and geochemical modifications induce significant changes in flow and transport properties. These changes can, for example, include one or more orders-of-magnitude increases in flow permeability”. Other definitions by Martino and Chandler (2004) define the EDZ by “measurable and permanent changes to the mechanical and hydraulic transport properties of the rock surrounding the excavation”.

A conceptualized view of the EDZ according to Siren et al. (2015) can be seen in figure 4.1. The excavation damage in the EDZ comprises, according to Siren et al. (2015) of two different causes:

- Reversible and irreversible property changes due to stress redistribution after excavation.
- A Construction damage zone depending on the excavation method.

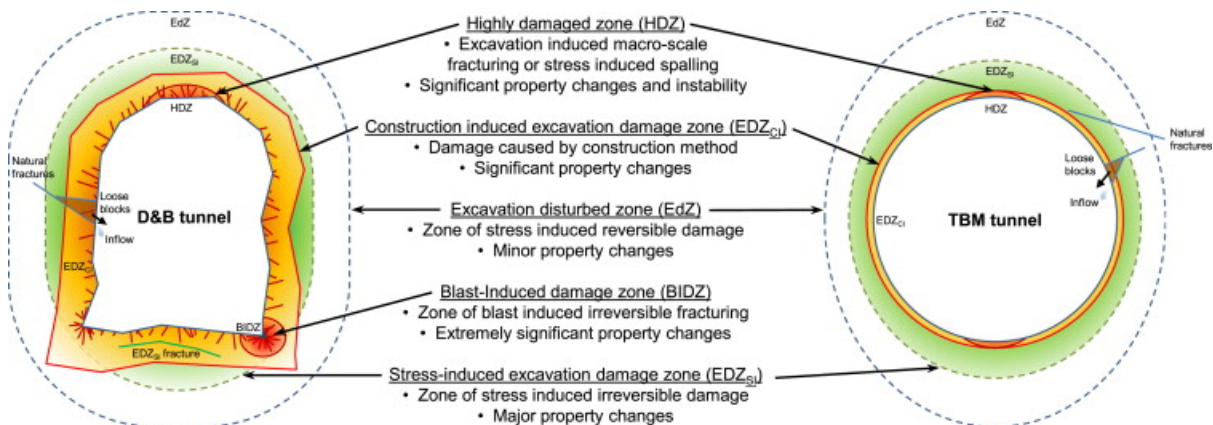


Figure 4.1: Categorization of different zones in the EDZ, according to Siren et al. (2015)

4.6.1 Stress-induced excavation damage

After excavation, the in-situ stresses will redistribute around the opening. Some regions experience stress concentrations, and others stress relief. The resulting stress redistribution affects the extent of the EDZ and can lead to compressive or tension forces working on the joints, affecting the joint aperture and the hydraulic properties. Microcracks might also form due the rock strength being compromised in either compressive or tensile strength. The extent of the EDZ is highly dependent on the nature of stress concentrations around the tunnel, especially the ratio of σ_1/σ_3 and orientation of the tunnel axis relative principal stresses (Read and Chandler 1999). Previously conducted research shows that the extent of the EDZ is higher in both zones of high deviatoric stress or low confining stress (Martino and Chandler 2004; Read and Chandler 1999; Souley et al. 2001). The studies involved assessments of the EDZ by several methods, including visual observation. Numerical modelling and measurements of transmissivity, permeability, and seismic velocity.

4.6.2 Construction induced damage

The excavation method also influences the EDZ. The zone which is damaged from the excavation method is called the construction damage zone (CDZ). Blasting is more likely to form microcracks, open existing joints, and activate healed joints (Siren et al. 2015). The extent of the EDZ can in a drill and blasted tunnel can range from 0.1 to 1.5 m (Tsang et al. 2005). Several studies have investigated the influence of drill and blast on intact rock properties. Siren et al. (2015) found that the mean value of Young's modulus was 10 % lower in a blasted tunnel compared to a tunnel excavated with TBM in the same rock type. The rock samples were obtained at a distance of 0.5-1 m from the tunnel boundary. Tveit (2018) found no conclusive evidence that Young's modulus is significantly different when comparing rock cores from a blasted and TBM excavated tunnel in the same rock mass.

4.6.3 Hydraulic properties of the EDZ

Research shows that the EDZ significantly alters the hydraulic properties of the rock mass. Water pressure measurements as a function of distance from the tunnel boundary by Holter (2015) show that the water pressure decreases close to the excavation. The extent of induced changes in hydraulic properties will vary around the tunnel boundary as a function of the excavation method and induced stress. Permeability measurements by Souley et al. (2001) show permeability was significantly higher in the crown and invert compared to the walls in a high horizontal stress situation with spalling. Transmissivity measurements by Martino and Chandler (2004) found that the

regions associated with reduced compression had a larger depth up to 1 m compared to undisturbed rock, indicating that reduced compressive stress allowed microcracks or joints to be open.

A study by Tveit (2018) compared the EDZ around a TBM excavated with blast excavated tunnel in the same rock mass. This study showed a significantly higher hydraulic transmissivity in the immediate rock mass around the blast-excavated tunnel than the TBM-excavated tunnel. The water flow pumped during the outer sections of the test holes was so high, that it was outside the range for the measuring equipment for water flow during the pumping tests. Hence a significantly higher transmissivity in the first 0.5 m in this study was observed but could not be precisely quantified.

According to Ericsson et al. (2015), changes caused by blasting can impact transmissivity in three ways: Enlarging of existing joints, re-activation of healed joints, and induced microcracks. Figure 4.2 show how joint transmissivity is increased close to the excavation. The charging amount of explosives affects the EDZ, and the rock mass will absorb more energy if the charging amount increases. Naturally, this is also expected to increase the joint frequency and permeability near the charge. Ericsson et al. (2015) found that hydraulic conductivity around the bottom charge in a borehole was higher than in the sections of the column charge. Because the invert generally is charged heavier than the wall, the EDZ zone is expected to be larger in the invert. The study by Ericsson et al. (2015) found that the extent of the EDZ occurred up to 0.3 m for sections charges with a column charge (0.5/km) and 0.5 m for sections charges with the bottom order (1.8/km). These findings correspond well with a review of the EDZ by Bäckblom (2008). One of the studies in this review estimated that the EDZ of the foot, which is charged heavier, had a depth of 0.8 m compared to 0.3 m in the wall.

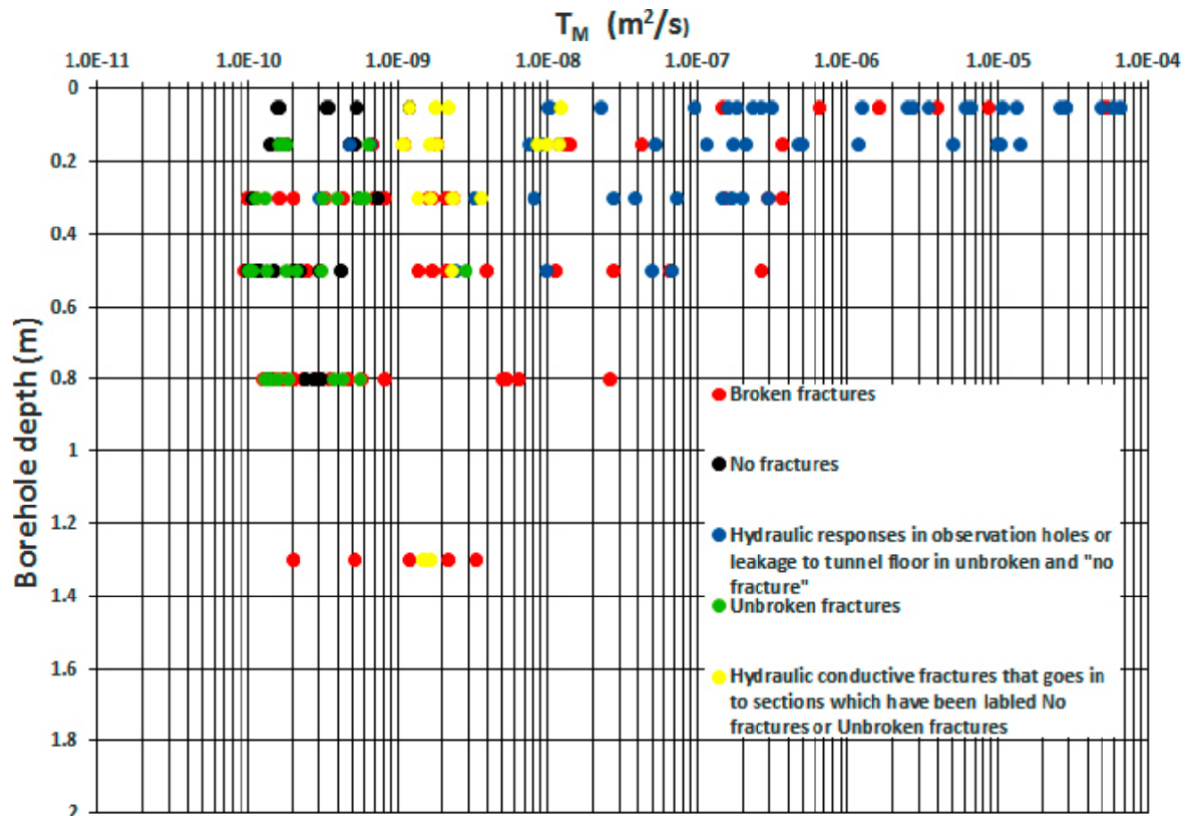


Figure 4.2: Section transmissivity plotted against depth for mapped joints put into different groups (Ericsson et al. 2015).

4.7 Numerical methods

This thesis uses numerical modeling to simulate different scenarios of the Hestnes railroad tunnel case study. Generally, there is a distinction between a continuous and a discontinuous approach when modeling rock mass. The finite element method (FEM) is a common solving scheme to model the first, and the distinct element method (DEM) is used for the latter. Both these models will be used in this thesis.

4.7.1 Finite element method

FEM is a continuous approach that models rock mass as either free of discontinuities or an equivalent jointed rock mass. In FEM, the model geometry is seen as a domain divided into small subdomains called finite elements (Reddy 2019). The full discretization of subdomains is usually called a mesh and is a collection of finite elements with nodes at their boundaries. Interaction between each finite element is determined by algebraic relations between element nodes that describe the physical problem to be solved (e.g., displacement and stresses). Finite elements can, for example, be constructed by triangles or tetrahedra.

4.7.2 Distinct element method

In DEM programs, the rock mass is treated as a medium divided into a finite number of discrete interacting blocks. The blocks are separated by interfaces and contacts that make up the domain. DEM allows for finite displacements between contacts, and the blocks can rotate and detach. Another feature is that new contacts are automatically recognized as the calculation progress (Cundall 1988). The blocks themselves can be either rigid or deformable.

4.7.3 3DEC

First introduced as a numerical software in 1988 (Cundall 1988), 3DEC has been continuously developed for over 40 years by Itasca Corporation, with the latest version (7.0) released in 2020. Although 3DEC is usually referred to as a discontinuous method, it is, in fact, a hybrid of continuum and discontinuous methods. The model is built up of blocks that are split by joints. The blocks can be modeled as rigid or deformable (e.g., a continuum). The joints are connected through contacts and can be given a constitutive joint model and mimic discontinuous behavior by allowing displacements between the contact points. 3DEC allows for fully hydromechanical coupling in the calculations of joint flow and the modeling of aperture changes. This is done by alternating mechanical and fluid calculations. 3DEC uses an explicit time-marching scheme, meaning that the simulation travels through time until a steady-state solution is achieved, unlike an implicit solving scheme that RS2 uses, which arrives at the solution. This is particularly useful when dealing with physical instabilities or nonlinear constitutive behavior in the model. Itasca also has a built-in programming language called FISH, which enables users to customize their own features in the model.

4.8 Statistical description of joint transmissivity

Statistical distributions are powerful tools that can be used to find representative values to be used in the numerical model. As part of the fieldwork in this thesis, water pressure testing was performed to assess the joint transmissivity in boreholes. The joint transmissivities were used to estimate the hydraulic aperture, which was later used in the 3DEC model. The theory behind these estimations will be presented below.

4.8.1 General statistical terms

In this section, some general statistical terms will be introduced. The most common statistical measure can be said to be the arithmetic mean. The mean of a value is defined as the sum of all values divided by the number as shown.

$$\bar{x} = 1/N \cdot \sum_{n=1}^N x_n \quad (4.35)$$

The variance gives the spread of data. It is found by taking the sum of the square of differences between the values and the expected value divided by the number of values minus 1. Show below in equation 4.36. The standard deviation, σ_x , can be approximated by taking the square root of s^2 .

$$s^2 = \frac{\sum x^2}{N-1} - \frac{N \cdot \bar{x}^2}{N-1} \quad (4.36)$$

The expected value is the value the mean approaches as the ensemble grows. It can be defined as the sum of the value times the probability of occurrence for that value.

$$E(x) = \sum_{n=1}^N x \cdot f(x) \quad (4.37)$$

4.8.2 Cumulative distribution function diagram

When plotting the statistical distribution of transmissivities, a cumulative distribution function (CDF) can be used (Gustafson and Walke 2012). A CDF shows the probability that a measured value is below or equal to a given value ($P(T \leq T_i)$). Weibull's formula can give the probability:

$$p(T \leq T_i) = \frac{n_i}{N+1} \quad (4.38)$$

The x-axis scale is often set to logarithmic because transmissivity values can vary between many orders of magnitude.

4.8.3 Pareto distribution

Another alternative to describe joint distribution is the Pareto distribution, also called the power-law distribution. For general theory and application on the Pareto distribution, see Adamic (2000). The Pareto distribution has been shown to describe calcu-

lated values well, whereas, for example, the log-normal distribution often has larger discrepancies at the endpoints (Gustafson and Walke 2012). Gustafson and Fransson (2006) proposed that the Pareto distribution for calculated data can be expressed as below in eq. 4.39. Here T_n is an arbitrary transmissivity value. In a log-log plot, the Pareto distribution follows a power line with a slope of $-k$. The line intersection gives the minimum transmissivity T_{min} with the $1 - P(T_n)$ line. Maximum joint transmissivity T_{max} is given by eq. 4.40.

$$\log(1 - P(T_n)) = \log(T_{max}^k / (N + 1) - K \log(T_n)) \quad (4.39)$$

$$T_{min}^k = \frac{T_{max}^k}{N + 1} \quad (4.40)$$

The work conducted by Gustafson and Fransson (2006) shows that the Pareto distribution is a valid method to assess transmissivity distribution for borehole intervals. It also confirms the common tendency that a few conductive joints contribute the most to the borehole transmissivity and that other joints have a low transmissivity. According to Gustafson and Fransson (2006) and Fransson (2002), data for the less transmissive joints are harder to obtain since the measurements are less reliable.

4.9 Summary and discussion of theory and background

The tunnel concept described in section 3 is a composed topic involving aspects of; flow characteristic of rock, material properties of shotcrete, grouting technology, and functional requirements and rule work. Limiting the amount of theory involved in describing these different aspects was necessary. Consequently, the most focus was given to presenting theories regarding the hydrogeological properties of rock, the excavation damage zone, and the background related to today's water- and frost protection practice.

Most of the theory presented in the chapter is directly applied to the conducted work. However, some theory is also given to make the reader aware that alternative approaches have been evaluated. Some of the theories regarding numerical work are only used in the software itself. In this case, the most important theory is elaborated so that the physical coupling between the real world and a numerical model is understood.

5 Case study description: Hestnes railroad tunnel

Hestnes railroad tunnel, currently under construction, is a 3.1 km drill-and-blast excavated hard rock tunnel between Kleverud and Espa. The project is a turnkey contract with special regulations of the pre-excitation grouting works where Veidekke is the main contractor and Bane NOR is the project owner. The tunnel is planned as a single tunnel with a double-tracked railroad. The height of the tunnel is around 10.5 m with a diameter of 14 m. The tunnel will have a cross-cut for each 1000 m with lengths of 340 m and 610 m (BaneNOR 2019). It is due to be completed in 2024. Figure 5.1 shows an overview of the project. The tunnel starts south at Kleverud, marked with a red -TB in figure 5.1. Two crosscuts are marked with numbers two and three. Number four is the northern face at Espa.

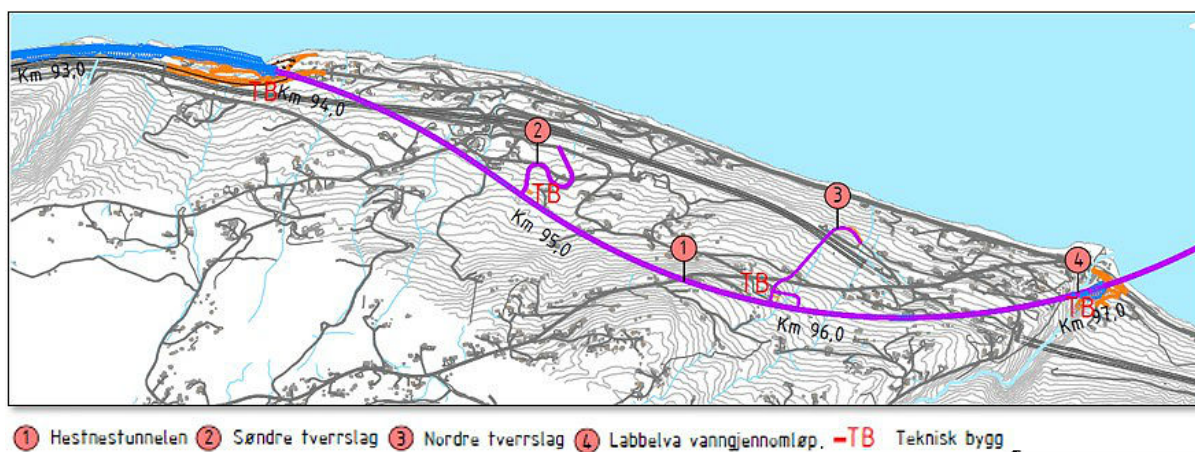


Figure 5.1: Overview of KS-1 Hestnes tunnel. Obtained from BaneNOR (2019)

5.1 Rock mass description

A view of the mapped rock types in the region by NGU (2022) can be seen in figure 5.2. The area is not mapped in detail and only on a 1:250 000 scale. The rock types in the area belong to the tectonic unit of the Sveconorwegian belt, which was created due to metamorphic, magmatic, and tectonic events around 1150-950 Ma at the southwestern margin of Fennoscandia (Slagstad et al. 2020). Figure 5.2 shows that there are primarily two main rock units with a range of different rock types inside each. According to NGU (2022), the following rock types can be found inside each unit:

- A unit consisting of mica slate, greywacke, quartzite, meta-arkose, meta-rhyolite and amphibolite/hornblende schist.
- A unit consisting of granitic- and/or augen gneiss, in places mylonitic.

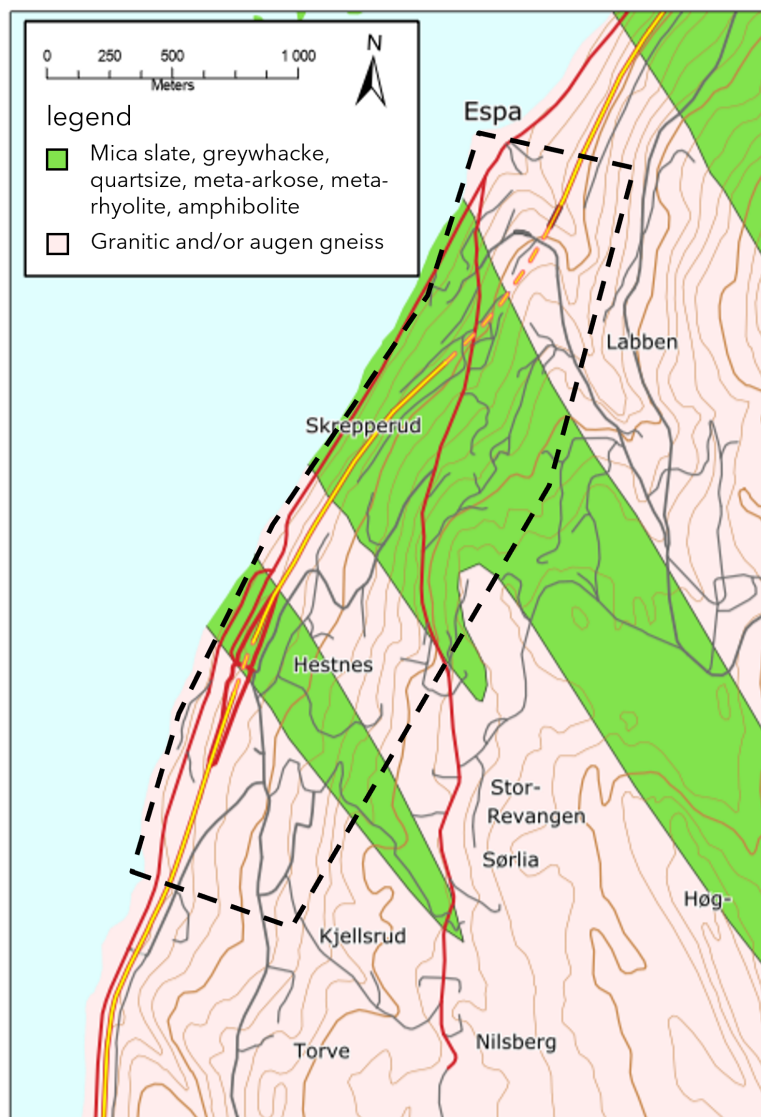


Figure 5.2: Rock types at the construction site. The black dashed area is the approximate location of the tunnel. The map is based on available maps from NGU (2022). The scale is 1:250 000.

5.2 Tunnel design with respect to water and frost protection

Water- and frost protection was initially planned as a drained structure with cast-in-place concrete lining, drainage geotextile, and sheet membrane waterproofing. The design included a waterproof membrane clad outside the concrete to make the structure waterproof with a geotextile to drain the surrounding rock mass towards the drainage system in the invert. The updated water- and frost-protection design regarding the grouting procedure is elaborated on in the upcoming section. The shotcrete is planned as a water barrier where inflow is sufficiently low following the grouting. If the desired inflow is not achieved, these areas can be covered by the traditional

water- and frost protection measures, like a sprayed-on membrane, PE-membrane, PVC-membrane or PP-membrane (Holter and Strømsvik 2023).

5.3 Grouting procedure at Hestnes tunnel

Below is a description of the grouting works at Hestnes, from Holter and Strømsvik (2023).

The grouting works at Hestnes are performed in three separate grouting fans:

- Fan one: Consist of MC and is performed around the whole tunnel. Accelerator is added for controlled curing. Stop criteria is either 20-70 bar or 300-800 L depending on overburden and rock mass conditions. Fan number one is meant to seal the coarser joint apertures and limit the use of CS.
- Fan two: Consists of CS with an added accelerator of saltwater for controlled curing. The fan is performed in the crown and the walls but not in the invert. Stop criteria is either 15-60 bar or 400 L depending on overburden and rock mass conditions. The purpose of fan number two is to fill the smaller joint apertures not penetrated by the MC.
- Fan three: A second fan of CS is performed to seal seepage from rock bolts puncturing the grouted zone in critical areas with overlap.

Stop criterion is reached when grout flow during pumping is reduced to 2 L/min for a sustained period of 30 s. The length of each fan is 24 m but reduced for challenging rock mass conditions.

5.4 Expected tightness

Estimations of the penetrability of the grout can be related to the grout materials used as part of the grouting procedure. Regarding micro cement, penetrability is related to particle size. Studies show that clogging of joints starts at grain sizes five times the physical aperture opening, and the smallest groutable aperture is three times the particle size (Axelsson et al. 2009; Mitchell 1982). In Hestnes, the largest particle size (d_{95}) is around 25 μm in the micro cement. An estimate on the smallest physical joint aperture that can be grouted can also be made by using a thumb of rule $4 \times d_{95}$, as suggested by (Barton and Roald 2023). The smallest groutable aperture is then estimated as $4 \times d_{95} = 100 \mu\text{m}$.

For colloidal silica, the behavior is not the same as for micro cement. Colloidal silica is commonly used for grouting smaller apertures. Experience and testing show that colloidal silica can grout joint apertures in the range of 10-170 μm (Boden and Sievaenen 2005; Funehag 2008; Hölttä et al. 2008)). Findings in the master's thesis by Krokedal (2022) showed that the measured rock mass conductivity after grouting with colloidal silica was around 10^{-10} m/s. The grouting works in this project were a part of the Fornebu commuter tunnel project. The procedure included two injection screens, one with micro cement and one with colloidal silica, similar to the grouting procedure at Hestnes.

Expected tightness can be summarized as follows:

- The MC can likely penetrate physical joint apertures down to around 100 μm .
- Joints apertures down to 10 μm is expected to be grouted by the colloidal silica.
- Hydraulic conductivity of the CS grouted rock mass is expected to be around 10^{-10} m/s.

Calculations to predict inflow before and after grouting in the Hestnes project will be presented in section 11.9. The analyses relied on gathered field and laboratory data and are not presented here.

6 Review of previous investigations

As part of the work in this thesis, previous investigations related to the excavation damage zone and in-situ stress measurements were reviewed. These include:

- WPT data from Gevingåsen and Drammen railroad tunnel.
- In-situ stress measurements at the Ulvintunnel.

6.1 Review of WPT data in Gevingåsen and Drammen

Sintef conducted the water pressure testing in two railroad tunnels; in Drammen around 24.07.2022 and Gevingåsen 25.02.2022. The purpose of the testing was to assess the hydraulic properties of the excavation damage zone. These projects have rock mass and tunneling conditions similar to that of Hestnes and are ideal for comparison. The data from the Drammen test site and the WPT data were unprocessed and core material was unlogged. The data from the Gevingåsen rail tunnel were included in the study in order to provide a larger data basis. As a part of the work in this thesis, the core material in these projects was logged, and the data from the WPT was used to investigate the effect of the excavation damage zone on joint transmissivity. The analysis is included in the lab work.

6.2 Review of in-situ stress measurements at the Ulvintunnel by Pöyry

In 2013 Pöyry (Afry from 2019) carried out 3D overcoring in-situ stress measurements in the Ulvin railroad tunnel, approximately 15 km south of the Hestnes tunnel site. The tunnel is relatively close to the Hestnes tunnel on the same side of Mjøsa. This makes the measured data ideal for in-situ stress analysis because there are no drastic changes in the topography between the locations, and the rock mass is similar. Since only 2D doorstopper measurements have been conducted at the Hestnesstunnel, the data from Pöyry are essential for analyzing the in-situ stress situation so that representable principal stresses are used in the 3DEC model.

Table 6.1 shows the summarized data of estimated horizontal and vertical stresses at the Ulvintunnel. It can be seen that the ratio σ_H/σ_v varies between 1.7-2.4, and the ratio of σ_h/σ_v varies between 0.8-2.4. The mean of σ_H is 7.1 MPa with a bearing of 138° , the mean of σ_h is 2.6 MPa with a 228° bearing. The mean of σ_v is 1.7 MPa. When comparing the bearings of the measured horizontal stresses, one can see the orientations and magnitude coincide with expected horizontal stress directions above Oslo area (Myrvang 2001).

Table 6.1: Estimations of horizontal and vertical stress, from Pöyry.

Hole depth	σ_H	σ_H bearing	σ_h	σ_h bearing	σ_v
[m]	[MPa]	[°]	[MPa]	[°]	[MPa]
31.59	8.2	154	1.6	244	1.5
31.59	10.5	135	3.6	225	4.4
32.63	5.6	141	1.9	231	0.8
Mean	7.1	138	2.6	228	1.7

Based on the measurements done by Pöyry, the following assessments can be made:

- Measured σ_h in this area has a horizontal-to-vertical ratio between 0.8-2.4, with a bearing between 226-244°.
- Measured σ_H in this area has a horizontal-to-vertical ratio between 2.4-8, with a bearing between 135-154°.

7 Executed work

A summary of the conducted work is given before the work is presented. The primary purpose of the work was to assess the hydraulic properties of the EDZ and to evaluate the conceptual tunnel model presented in section 3. The work was done in a stepwise effort where field work laid the foundations for the lab work, and the gathered data culminated into a numerical model. The work can be divided into three parts: field work, laboratory work, and numerical simulations. An overview and description of the main items can be seen in table 7.1.

Table 7.1: Overview of the main parts of the executed work

Executed work	Description	Section
Field work	Mapping of geological conditions at the construction site of the case study. Water pressure testing, rock-core extraction, and in-situ stress measurements.	8
Laboratory work	Core logging, transmissivity estimations from WPT data, and rock mechanical testing.	9
Numerical simulations:	Simulations in RS2: <ol style="list-style-type: none"> 1. Back-calculating of in-situ stress. 2. Fluid flow analysis of the EDZ, grouted zone, and shotcrete. Simulations of three scenarios in 3DEC: <ol style="list-style-type: none"> 1. Stress-induced EDZ. 2. Grouted tunnel with EDZ. 3. Grouted tunnel with shotcrete and EDZ. 	11

8 Field work

To find the necessary data for the input parameters in the 3DEC model, field investigations were conducted several times at the Hestnes construction site. The investigations were carried out in the periods of 16-17.02.2023 and 01-03.03.2023. Rock mass investigations, Q-system mapping, joint mapping, joint roughness (JRC), and joint compressive strength (JCS) measurements were carried out as part of the investigations. Rock core drilling and water pressure testing in 8 boreholes was conducted in collaboration with SINTEF between 16-17.02.2023 to gather information regarding the transmissivity of the excavation zone. The measurements also included in-situ stress measurements.

8.1 Rock mass description

Two different rock types were observed at the site, a massive pre-Cambrian bedrock gneiss and an amphibolite. The gneiss was observed as the main geological body at the site. The matrix consisted of fine material with varying color pink/red to dark/grey nuances in some locations. Inside the matrix was porphyroclastic feldspar of different sizes, in places forming characteristic augen. At other places, the gneiss had a more granitic appearance. Some shearing with mylonitic bands was also observed. The amphibolite is interpreted as originally a diabase, which is a dark-colored fine-grained igneous rock. The diabase has penetrated the gneiss as dykes and later been transformed into amphibolite following metamorphosis. This can be seen in figure 8.1. The amphibolite appeared in the field with a dark/black color and a fine-grained matrix. Repeated tectonic events have given the amphibolite a chaotic appearance with hydrothermal quartz veins. At some locations, it is smeared into the augen gneiss, which can be observed in figure 8.2.



Figure 8.1: Amphibolite with a dyke-like appearance in the gneiss. The amphibolite dips steeply 70 degrees into the tunnel face. The picture is taken at the Kleverud tunnel face.



Figure 8.2: Strongly tectonized vertical amphibolite dyke with surrounding gneiss. The Picture was taken at the Espa tunnel face.

8.1.1 Rock mass quality

Using the Q-value classification system, the rock mass quality was investigated at three locations (Espa tunnel face, Cross-cut, Kleverud tunnel face). The guidelines given by NGI (2022) were followed. Q-mapping was carried out after each blasting round whenever possible. In the project, rock support depends on the rock support class given by the Q-value. For this thesis, Q-mapping was done to assess the rock mass quality and to understand the rock mass in the area. In each blasted section, attention was given to the most critical area in terms of stability, to assess the Q-parameters. The mapped parameters and corresponding Q-value are presented in table 8.1.

The highest mapped Q-value was 9, and the lowest was 0.14, a range from C to E in rock support classes according to the Q-system (NGI 2022). Generally, the rock mass in the project had a massive appearance with high RQDs of 75-90. The exceptions were location-specific amphibolite with higher joint intensity (figure 8.2) and areas with bands of crushed rock. Most locations were mapped with three joint sets plus random joints. Intermediate-scale joint features were generally planar to undulating with rough and smooth small-scale surfaces. The joint fillings showed larger variations. Observations included bands of crushed rock with sandy/silty particles and joints of hydrothermal quartz-filled veins. The presence of clay particles in some zones of crushed rock was assessed as probable but not confirmed by physical investigation other than visual observation. Physical confirmation was hard to achieve because of no rock support in the crown or ongoing works at the tunnel face.

Very little water inflow was observed in the field. One bolt leaked water, and one probing hole leaked a small amount, less than 1 L/min. The mapped areas were pre-grouted (except the cross-cut tunnel), so minor inflow was expected. There is low overburden at the Espa and Kleverud tunnel face, as low as 5 m in connection with the Kleverud tunnel start. The low overburden gives an SRF value of 2.5 in most of the tunnel. The exception is the cross-cut where the overburden is around 70 m, and a value of 1 is given.

Table 8.1: Mapped Q-values at the Hestnes tunnel site.

Site location	RQD	J_n	J_r	J_a	J_w	SRF	Q-value
Espa face	75	12	1	6	1	2.5	0.25
Espa face	90	6	1	1.5	1	2.5	9
Kleverud face	70	12	1.5	1	1	2.5	3.75
Espa face	40	12	1.5	3	1	2.5	0.67
Kleverud face	80	12	1.5	2	1	2.5	2
Cross cut towards Espa	90	6	3	2	1	1	22.5
Cross cut towards Kleverud	30	3*12	3	6	1	1	0.14
Kleverud	40	12	1.5	4	1	2.5	0.5

8.2 Joint mapping

Joint parameters mapped during field investigations include joint orientation, persistence, spacing, and JRC and JCS. The joint properties are essential input parameters in the numerical model.

8.2.1 Joint orientations

A total of 64 joint orientation measurements were done as part of the joint mapping. The measurements are presented as a pole plot and joint rosette in figure 8.3 and 8.4. The joint system varied in orientation and appearance, depending on the location. This is also evident in the spread of measurements in the pole plot. A total of 3 main joint sets were found with a significant amount of random joints and, locally, less systematic joint systems. This also coincides with the Q-mapping, where a J_n value of 12 (3 joints plus random joints) was the most common observation.

Table 8.2 summarizes the joint set characteristics. Figure 8.7 shows joint spacing and persistence observations. Of the three main orientations, two joint sets (J1 and J2) are dipping steeply in the NE and SW directions, respectively. The last joint set (J3) is sub-horizontal with a varying dip direction and dip between 0-30°.

A foliation was in places visible in the amphibolite (see figure 8.8) with a steep fall in the NE direction, coinciding with J1 joint orientation. The same foliation direction was found in the gneiss from rock cuts on the surface. The jointing appeared chaotic at the site, especially in the amphibolite. Even so, the main joint orientations were consistent throughout the tunnel route. The joint sets were observed to be persistent through both rock types, as illustrated in figure 8.5a and observations of the joint sets in both rock types (see figure 8.5b and 8.10). Figure 8.6 and 8.7 show typical joint set spacing observations.

As shown by the Q-mapping in table 8.1, the joints were generally planar and undulating in the intermediate scale with rough or smooth surfaces small scale. Some joint infillings of crushed sandy/silty and possibly clay material was also observed in some joints.

Table 8.2: Joint orientation characteristics for the three main joint set observations.

Joint set	Dip/dipdirection (°)	Spacing (m)	Persistence (m)
J1	69/64	0.5-5 m	>7 m
J2	61/258	0.5-3 m	>7 m
J3	9/9	2-4 m	>10 m

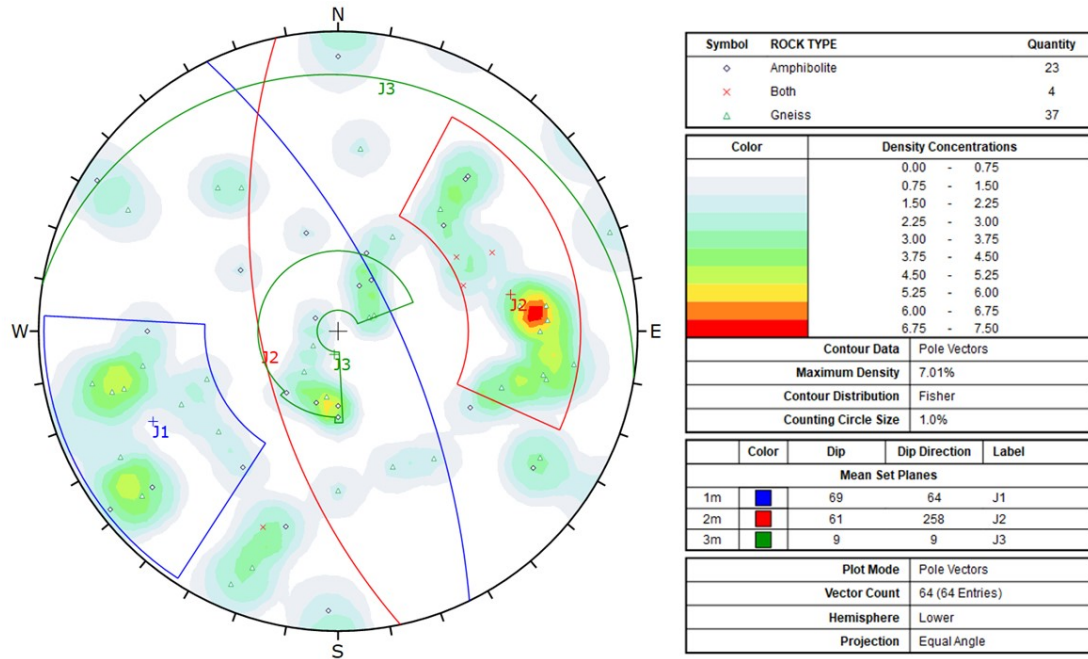


Figure 8.3: Joint pole plot for the measured joint orientations.

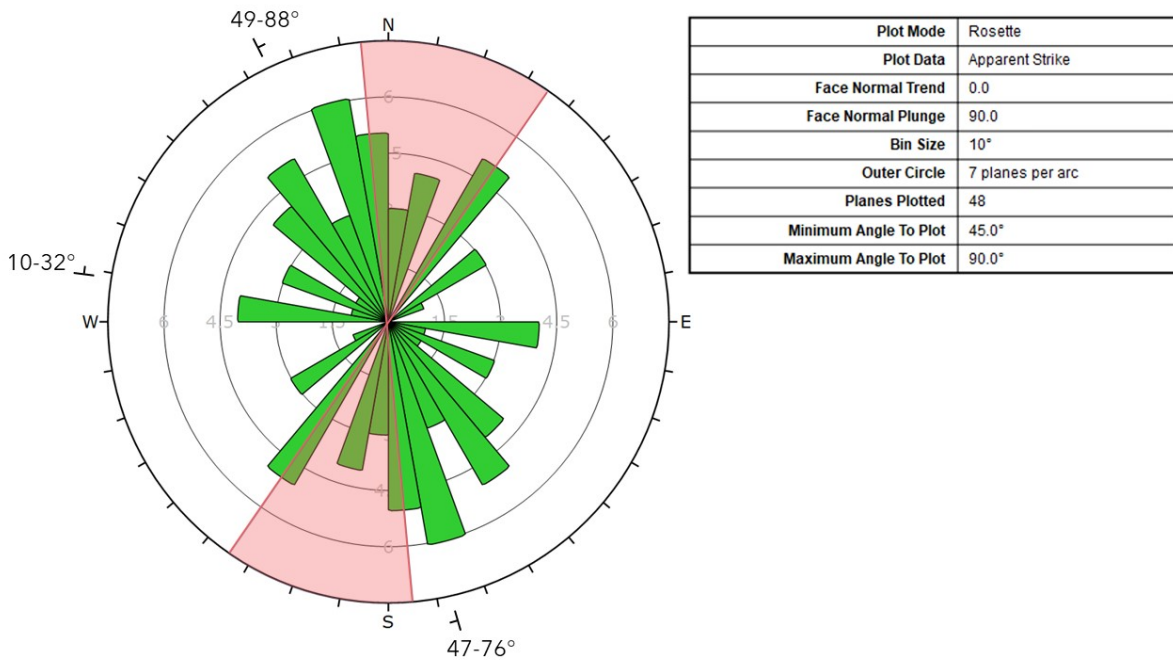
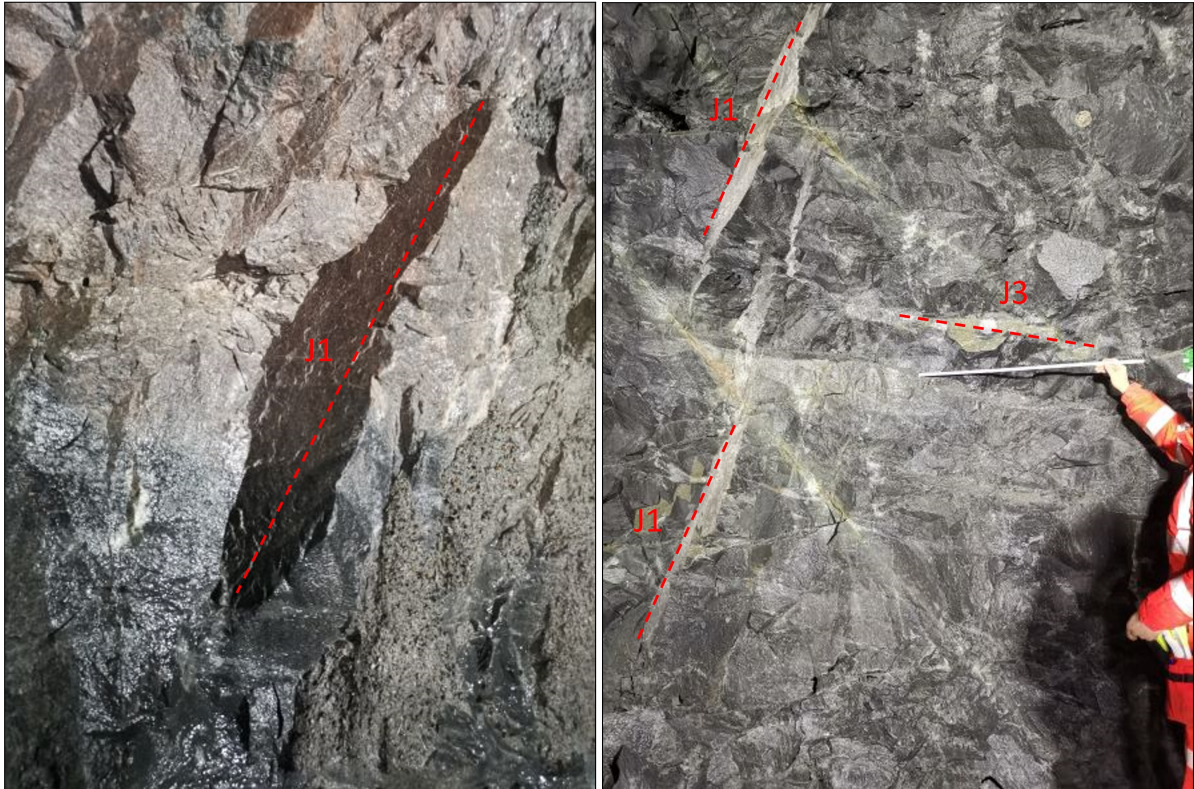


Figure 8.4: Joint rosette. The red-shaded area shows variations in tunnel alignment.

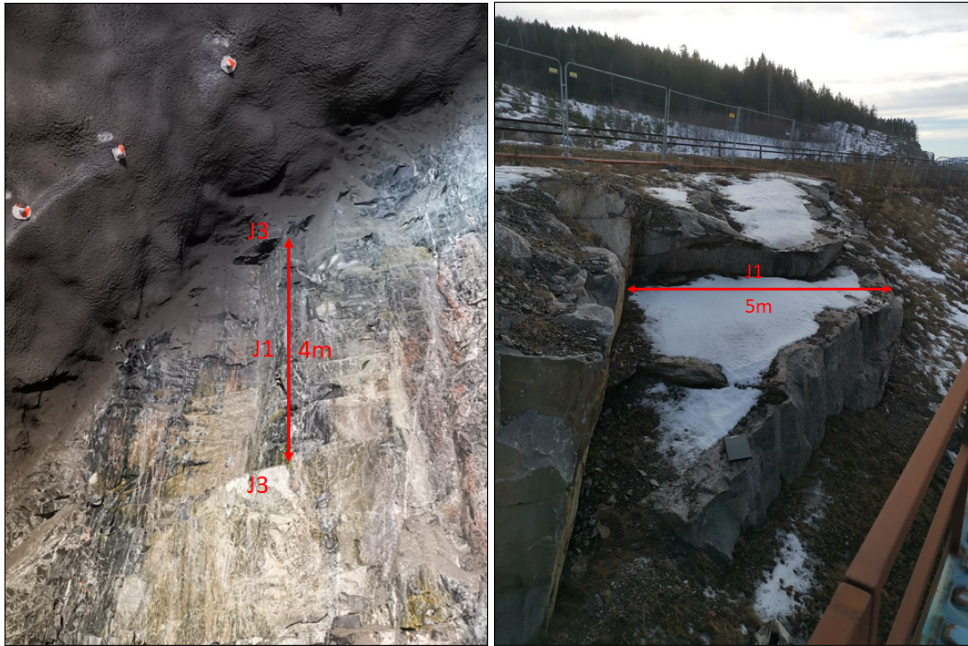


(a) Joint set J1 with persistence through both rock types. The picture was taken at the Kleverud tunnel face. (b) Joint set J1 and J3 visible in the amphibolite. The picture was taken at the Kleverud tunnel face. Scale of ruler is 1 m.

Figure 8.5



Figure 8.6: J2 joint set visible in the gneiss on the left-hand side. Joint spacing 0.5-3 m



(a) Example of the sub-horizontal joint set, J3, with an approximate spacing of 4m. Measured strike dip is 130/30NE (J3) and 142/88NE (J1). (b) Joint sets in the gneiss with a spacing of 5 m belonging to J1. Strike dip measured as 165/76E.

Figure 8.7: Example of joints from surface mapping



Figure 8.8: Amphibolite (left side) with a visible foliation parallel with the bedding with a strike/dip of 180/65SE. The picture was taken at Espa tunnel face.



Figure 8.9: Example of the sub-horizontal joint set J3 in the amphibolite, picture taken at the same location as in figure 8.8. Strike/dip is 030/10W. Folding ruler for scale, 0.4 m.



(a) Example of the sub-horizontal joint set J3 in a gneiss rock cut south of Kleverud.
(b) Example of joint set J1 in a gneiss rock cut south of Kleverud.

Figure 8.10

8.3 JRC and JCS investigations

JRC and JCS describe the rock joint's roughness and compressive strength. They are used in the equations to estimate rock joint shear strength, rock joint shear, and normal stiffness. Data on JRC and JCS was gathered during all field investigations, with the method described in the sections below.

8.3.1 Joint roughness number (JRC)

JRC was measured using a steel profilometer; see figure 8.11. First, the most probable slip direction was identified, and the comb was pressed down in this direction. Afterward, the profile is drawn down using a pencil and a clean sheet. The JRC value is later found by comparing the drawn profile with available JRC tables from (Barton and Choubey 1977). Great care was taken to identify the most critical joint surfaces, especially systematic joint sets. This was done to ensure that the measured JRC represents the joint system of the rock mass that would later be represented in the 3DEC joint model. Measurements were done on joints for both rock types since different values in the 3DEC model will represent them.

A total of 22 measurements were done. 13 in the gneiss and 9 in the amphibolite. The corresponding JRC values can be viewed in figure 8.12, 8.13 and 8.14. Individual JRC values and their respective strike/dip can be seen in table B.1 in appendix B.

Based on JRC measurements on the respective joint surfaces in both rock types, the following JRC values are given to the respective joint sets:

Gneiss:

- J1: 3
- J2: 7
- J3: 5

Amphibolite:

- J1: 6
- J2: 4
- J3: 4

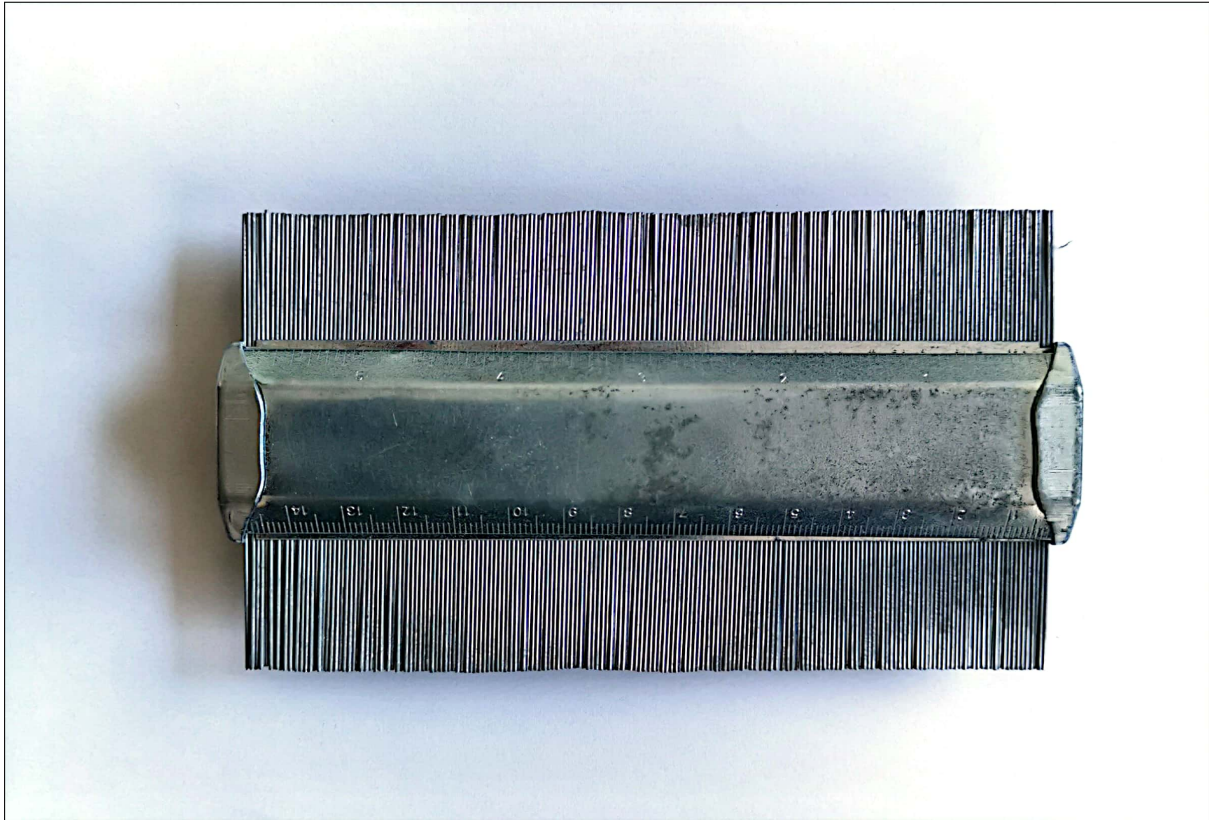


Figure 8.11: Steel profilometer that was used to measure JRC. Length is 15 cm.

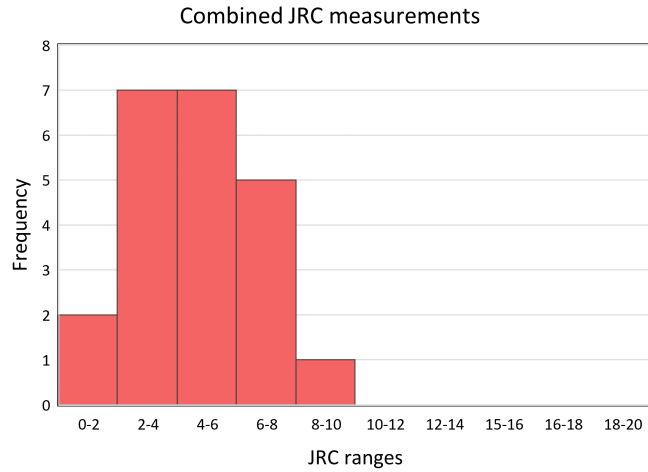


Figure 8.12: Combined JRC values for measurements in both rock types. n=22.

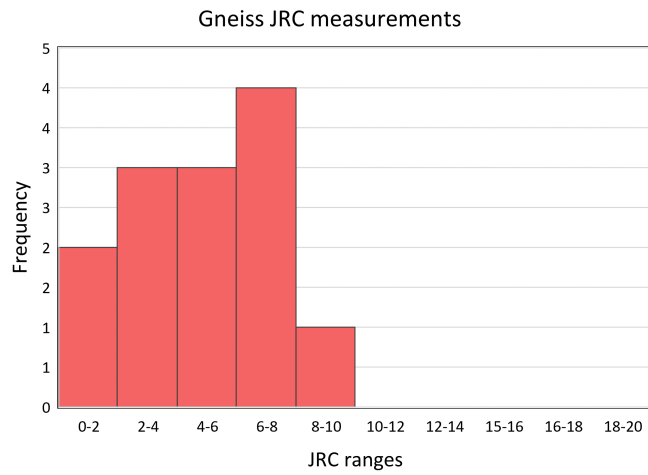


Figure 8.13: JRC values for the measurements taken in the gneiss. n=13.

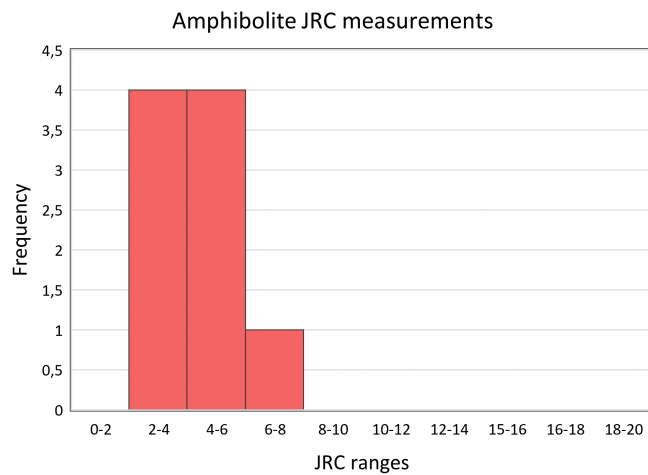


Figure 8.14: JRC values for the measurements taken in the amphibolite. n=9.

8.3.2 Joint wall compressive strength (JCS)

JCS was measured with an L-type schmidthammer by following the guidelines given by ISRM (Aydin 2015). The measurements were done as illustrated in figure 8.15a. The schmidthammer was held perpendicular to the joint, then pressed down, and then the measured value was read. Twenty measurements were done on each joint surface, and the mean was used in calculating the JCS value. Obvious measurement errors, e.g., measurements on a loose rock due to blasting, dirty rock surfaces, or bad contact between the hammer and rock, were thrown away, and a new measurement was done. According to Aydin (2015) all values are to be kept; however, in an environment with a lot of direct and indirect influence of ongoing construction works, keeping measurements that did not reflect the rock mass made no sense.

During the field investigations, an attempt was made to measure an unweathered joint surface of each rock type for later correlations of UCS. Depending on the site conditions, joint surfaces that appeared representative were tested as much as possible. Not all joint surfaces that later will be used in the 3DEC model were tested, and this is due to the nature of a tunnel under construction. Often there was limited time to do measurements at the tunnel face, and not all joint sets presented themselves with a good testing surface, making it difficult to get all the measurements one ideally would want for each joint surface.

A statistical description of the recorded rebound values for the respective joint surfaces is summarized in table 8.3. The normalized rebound values for the respective joint surfaces can be viewed in figure 8.16.

Rebound values were adjusted to downwards facing according to the corrections given by Barton and Choubey (1977). The rebound value had to be correlated to the UCS value found in the laboratory testing to find the JCS. In a study by Aydin and Basu (2005), who reviewed correlation equations for UCS and Young's modulus found in other studies, they found that the correlation between UCS, Young's modulus, and the rebound value can be expressed by either of the two following pair of equations.

$$UCS = a \cdot e^{(b \cdot R)} \quad \& \quad E = c \cdot e^{(d \cdot R)} \quad (8.1)$$

$$UCS = a \cdot R^b \quad \& \quad E = c \cdot R^d \quad (8.2)$$

To find a proper way of estimating JCS, the best fit of the UCS value and the highest

rebound value was found by comparing the results of different studies. The best fit was found in the correlation equation given by Karaman and Kesimal (2015), given in equation 8.3. This study reviewed 47 different rock samples. A UCS value of 173 MPa was estimated by using the highest adjusted mean rebound value taken in the amphibolite (table 8.4) and the correlation equation found by Karaman and Kesimal (2015), which is very close to the 170 MPa measured in the lab (Section 10.3.1). The rebound value of 60 is also assumed to represent an unweathered joint surface, which in theory, should be the same as the UCS value.

$$JCS = 0.1383 \cdot R^{1.743} \quad (8.3)$$

Here JCS is the joint compressive strength (MPa), and R is the rebound value from the schmidthammer. The results of the JCS calculations are presented in table 8.4.

Based on the orientations of the tested joint surfaces, the following JCS values are assigned to the different joint sets and rock types:

Gneiss:

- J1: 140 MPa
- J2: 97 MPa
- J3: 159 MPa

Amphibolite:

- J1: 105 MPa
- J2: 105 MPa
- J3: 105 MPa

Since no JCS measurements were done on the joint surfaces J1 and J2 in the amphibolite, these joint sets are given the value of joint set J3.



(a) JCS testing on a joint surface in the augen gneiss. (b) JCS testing on a joint surface in the amphibolite.

Figure 8.15

Table 8.3: Statistical description for the schmidthammer rebound values from the field investigations.

Strike/dip	Mean	Median	Mode	Minimum	Maximum	Range	Rock type
177/70W	53	55	58	39	62	23	Gneiss
178/69W	47	48	48	35	53	18	Gneiss
168/80E	53	55	58	39	62	23	Gneiss
096/32N	57	57	58	49	66	17	Gneiss
140/81E	48	48	47	47	51	4	Gneiss
030/54NW	43	41	40	32	60	28	Amphibolite
030/10SW	46	45	45	38	55	17	Amphibolite
083/70N	60	62	62	45	70	25	Amphibolite

Table 8.4: Adjusted rebound values and calculated JCS values.

Strike/dip	Rebound value	Adjusted rebound value	JCS (MPa)	Rock type
177/70W	53	49	122	Gneiss
178/69W	47	43	97	Gneiss
168/80E	53	53	140	Gneiss
096/32N	57	57	159	Gneiss
140/81E	48	48	118	Gneiss
030/54NW	43	37	75	Amphibolite
030/10SW	46	45	105	Amphibolite
083/70N	60	60	174	Amphibolite

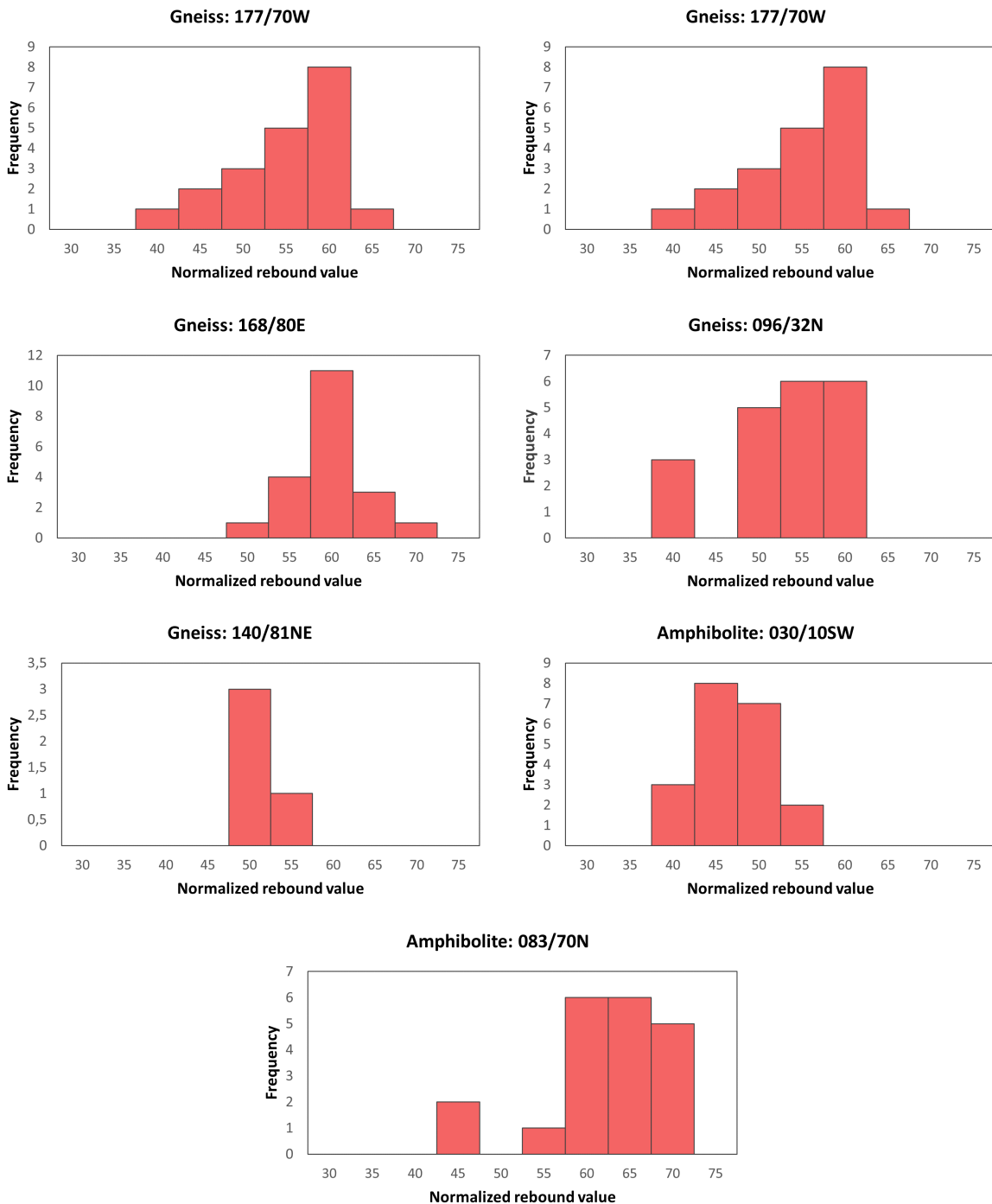


Figure 8.16: Normalized schmidhammer values. The figure shows the value for different joints in both gneiss and amphibolite, distinguished by strike/dip.

8.4 Rock core extraction and water pressure testing

Rock core drilling and water pressure testing (WPT) were conducted in collaboration with Sintef in two different periods (figure 8.17). 16-19.02.23 and 10-17.04.23. Drilling and WPT were done in both the gneiss and amphibolite. The rock cores were later mapped in the laboratory, together with the results of the WPT.

8.4.1 Rock core drilling

The holes were drilled in the cross-cut of the tunnel right before the split (Location 2 in figure 5.1 into the two main tunnel directions during the first investigation round from 16-19.02.2023. The holes were elevated around 1.5 m above the tunnel foot and drilled with about 2 m spacing using a 62 mm drill. Figure 8.18a shows a picture of the setup. A total of 8 holes were drilled with a borehole length of around 3 m.

8.4.2 Water pressure testing

The rock cores from the rock core drilling were inspected, and the depth of the individual joints was identified and tested to find the joint transmissivity along the borehole length. Individual joints were isolated using double-inflated packers with a test section length of 15 cm. Figure 8.17 shows the setup of the WPT equipment. Figure 8.18b shows a view of the packer setup. Test section pressure, hydrostatic pressure, and water flow out of the borehole were recorded for each test section. Testing of individual joints was done through a three-step pressure build-up to confirm linearity between pressure and water flow. In the first meter of one borehole, water leaked out of an adjacent borehole, and no joints were measured in the first meter of these two boreholes.

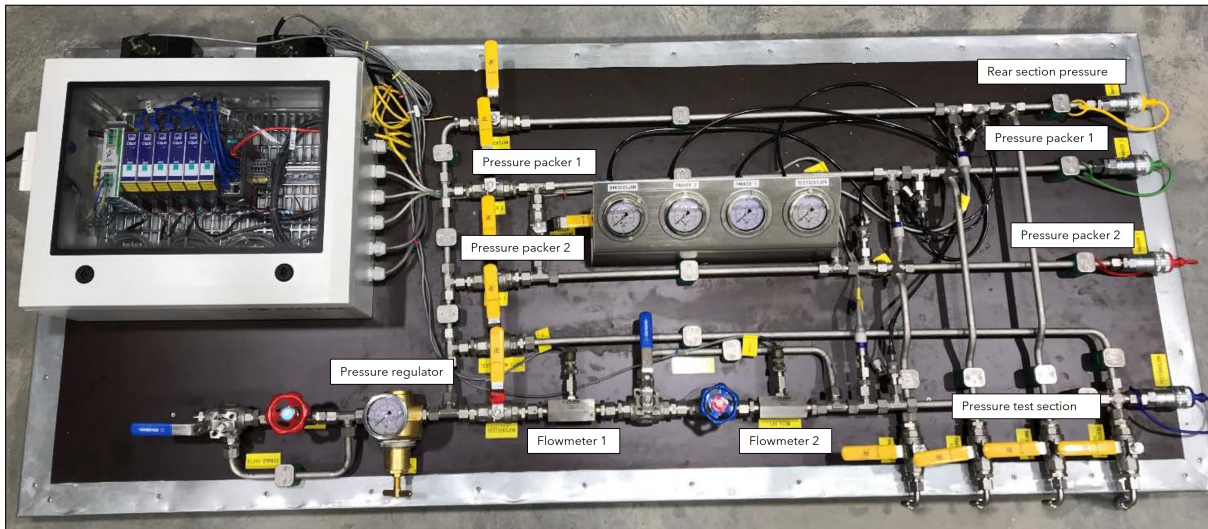


Figure 8.17: WPT equipment setup (SINTEF 2023)



(a) Setup of the drilling of rock cores and holes (b) Setup of the double packers with a 15 cm test section later used for WPT.

Figure 8.18

9 Laboratory work

9.1 Rock core-logging of the Drammen and Gevingåsen projects

In the period 09-13.01.2023, the rock cores of Drammen and Gevingåsen were logged in the laboratory. The purpose of the mapping was to map the rock type, joint types, *RQD*, joint spacing, *JRC*, and joint fillings and to assess the extent of the EDZ. In addition, the mapped joints were coupled to WPT data so that estimations of joint transmissivity and joint aperture of individual joints could be done.

9.2 Rock core-logging of the Hestnes Project

The cores were logged 21-23.02.2023. The logging procedure was the same as for the Drammen and Gevingåsen project. J_r and J_a were also mapped for potential Q-value and joint friction analysis. The rock-type boundaries were also mapped. More time was spent investigating the joint system and joint sets in the different rock types to complement the field investigations of the joint system. A typical rock core from the project can be seen in figure 9.1.

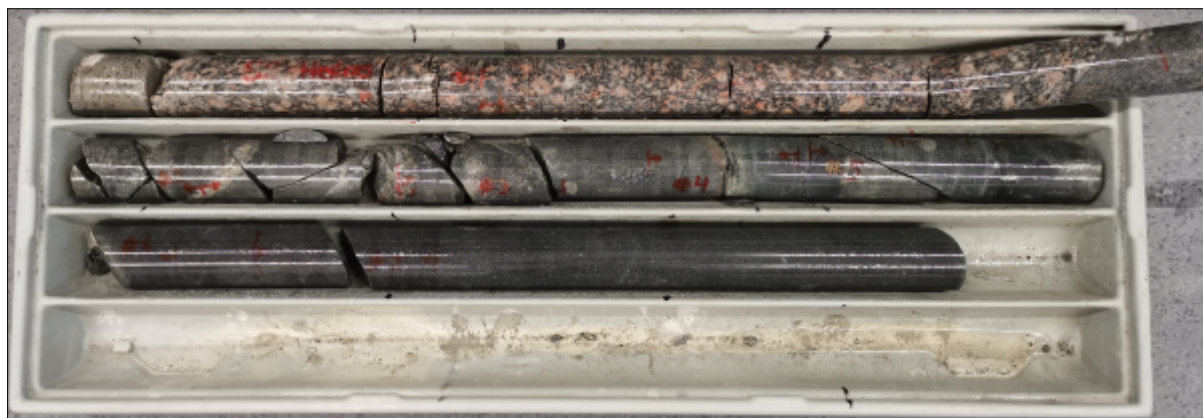


Figure 9.1: Borehole 2 from field investigations in the Hestnes project. The first meter is in characteristic augen gneiss, and the rest of the core is amphibolite.

9.3 Transmissivity estimations

Transmissivity of individual joints was estimated using Moye's formula and validated by Gustafson's equation presented in section 4.2.1. Joint apertures were calculated using the cubic law, and only the transmissivities from Moye's formula were used for the statistical representation.

9.4 Method - Rock mechanical testing

Two tests were carried out in the laboratory; Uniaxial compressive strength (UCS) and tilt test. The UCS value, Young's modulus (E-modulus), and Poisson's ratio are obtained from the UCS test. The basic friction angle ϕ_b is obtained from the tilt test.

9.4.1 Specimen preparation

A total of 6 rock core cores were collected after core logging was conducted. Three cores were collected from each rock type. An attempt was made to capture the rock's inhomogeneities by collecting cores that differed in visual appearances, such as color and foliation. The original radius of 62 mm in the cores were kept. The average length of the cores was cut to be around 165 mm. The length/core ratio is slightly above 2.6 and inside the ratio recommended by ISRM (Bieniawski and Bernede 1979). The ends were sawn-cut and then grinded to have a smooth testing surface without irregularities. Afterward, the cores were weighed, and the density and p-wave velocity was measured and calculated. All testing was performed on dry cores. The descriptive values are presented in table 9.1. The gneiss cores were labeled A1, A2, and A3. The amphibolite cores were labeled B1, B2, and B3. Photos of the cores can be viewed in figure 9.2 and 9.3.



Figure 9.2: Prepared gneiss cores, labeled A1, A2 and A3.



Figure 9.3: Prepared amphibolite cores, labeled B1, B2 and B3.

Table 9.1: Descriptives of test specimens used in UCS testing and tilt-testing

Specimen	D mm	L mm	Weight g	volume mm ³	Density g/cm ³	Travel time µm	Travel speed m/s
A1	61.94	165.49	1369.58	498.66	2.75	32	5172
A2	61.98	165.75	1353.8	500.09	2.71	32.8	5053
A3	62.03	165.76	1374.43	500.93	2.74	30	5525
B1	62.99	166.25	1472.96	501.76	2.94	28.4	5854
B2	61.97	166.38	1460.72	498.81	2.93	31.9	5184
B3	61.95	165.39	1450.33	498.52	2.91	20.4	5626

9.4.2 UCS-testing

The method used to prepare and perform the UCS test followed the guidelines ISRM describes in Bieniawski and Bernede (1979). The testing was performed in a GCTS RTR-4000 apparatus; see figure 9.4 for the test setup. The test specimen was covered in a plastic sleeve to prevent flying debris from an explosive failure. Before testing, one radial and two axial accelerometers were installed to measure axial and radial displacement while testing. The radial accelerometer was attached around the circumference of the core by a deformable chain held together by elastic straps. The radial accelerometer was placed in the middle of the test specimen.

The length of the test section, which is covered by the two axial accelerometers (approximately the middle 50 % length of the test specimen), was used as the initial length (L_0) for calculating the strain. This was done to prevent any end effects during testing. During testing, the load continuously increased at 0.8 MPa/s until yielding. An automatic radial strain control was utilized to prevent explosive yielding of the rock cores. For the amphibolite cores, which showed a very brittle behavior when yielding, the loading rate was reduced manually when the stress-strain curve flattened and approached the UCS value. This was done to reduce the risk of impairing the testing equipment.

9.4.3 Tilt-testing

Tilt testing was performed by the three core methods for which the testing methodology is described by Alejano et al. (2018) and Li et al. (2019). The testing equipment and setup can be viewed in figure 9.5. The test equipment consists of a tiltable board raised and lowered by an air-driven piston controlled by a pressure valve. An inclinometer is installed that measures the angle of the board during testing. A plastic wall locks the two bottom cores on the sides to prevent any sideways movement. A metal wall prevents the two cores from sliding downwards during testing. The third core is placed on top of the two bottom cores when the test is performed. The board was raised at an angular speed of $24^\circ/\text{min}$. When the first visual displacement occurred, the tilting was stopped, and the tilt-angle registered. A total of 5 test was performed on each core. After one core was tested, the places were swapped, and a new core was tested. The cores were split into four quadrants with a marker to ensure no surface was tested more than five times. This was done to reduce the grinding that might occur when the core slides on the same surface repeatedly.

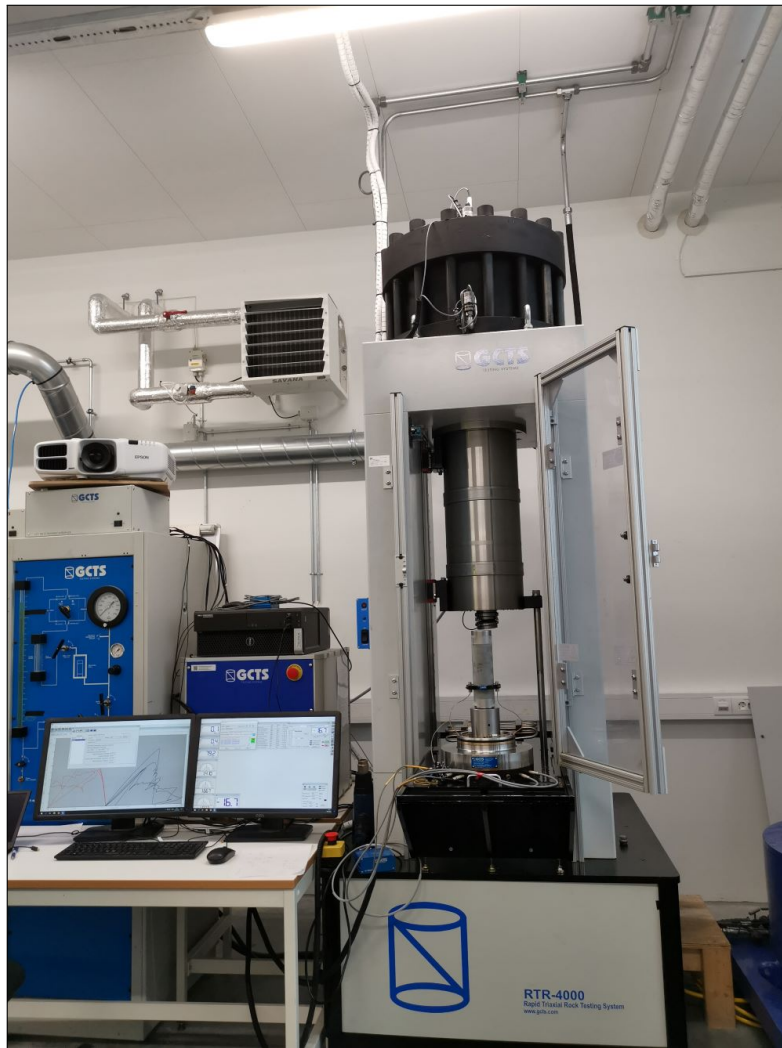


Figure 9.4: GCTS RTR-4000 testing apparatus used in the UCS testing.

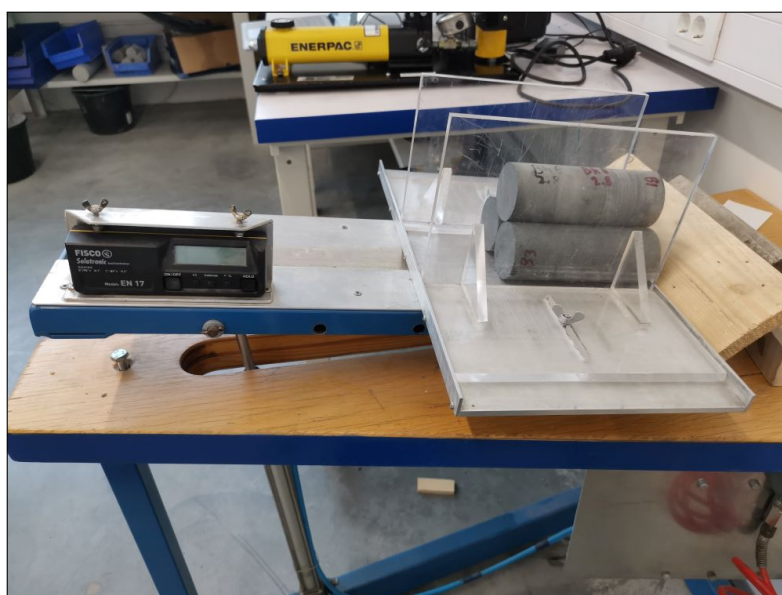
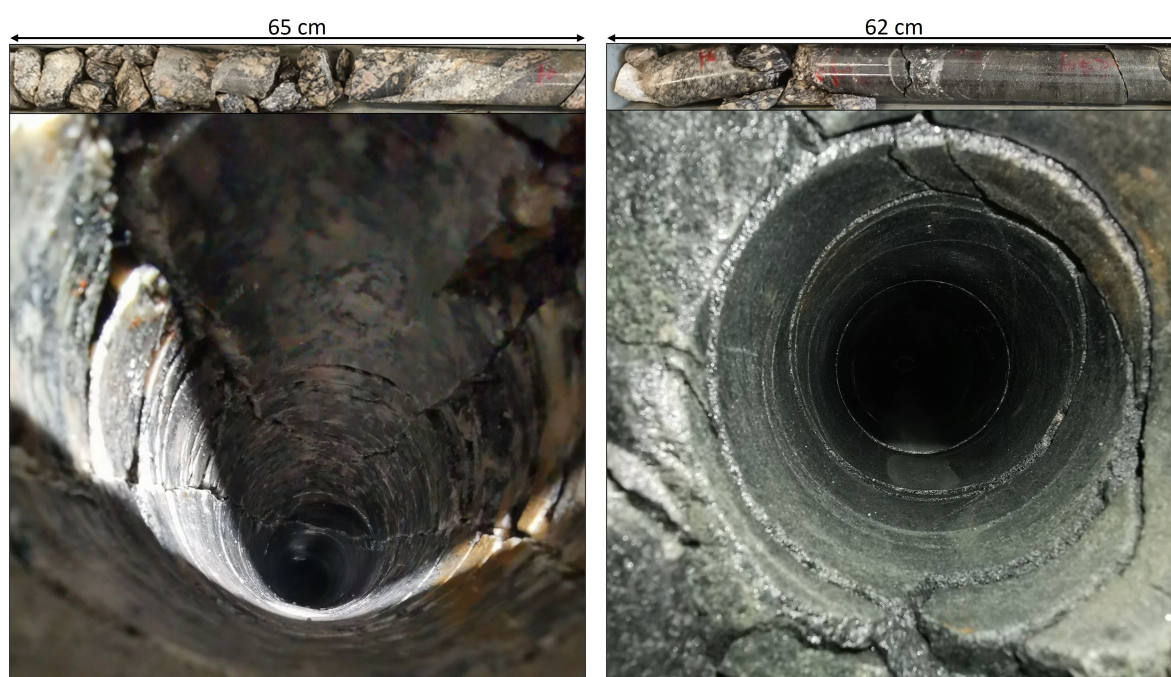


Figure 9.5: Tilt testing setup.

10 Analysis and results from field and laboratory investigations

10.1 Results of corelogging

The core log of the three projects can be viewed in appendix B, B, and B. The cores generally had a larger joint intensity close to the tunnel contour. This is probably due to the effect of blasting, which is expected to induce new and enlarge existing joints. Figure 10.1 shows an example of blasting-induced damage in two boreholes and the corresponding cores for two boreholes in Hestnes.



(a) Signs of blasting-induced damage in gneiss. (b) Open joints close to the excavation, likely due to blasting damage. Both longitudinal and parallel open joints can be seen.

Figure 10.1: Example of blasting damage in two boreholes and corresponding cores.

10.1.1 Transmissivity and aperture distribution

Figure 10.2 and 10.3 show the transmissivity and aperture distributions in the Gevingåsen, Drammen, and Hestnes project as a function of distance from the tunnel wall. As both figure 10.2 and 10.3 show, there is little to no correlation between distance, transmissivity, and aperture for the full borehole length. However, there is an increase in both transmissivity and aperture close to the start of the borehole, especially the first 0.5 m, except a few high transmissivity joints between 1-2 m. Looking at both scatter plots, the frequency of higher transmissivity joints is higher the first 0.5 m.

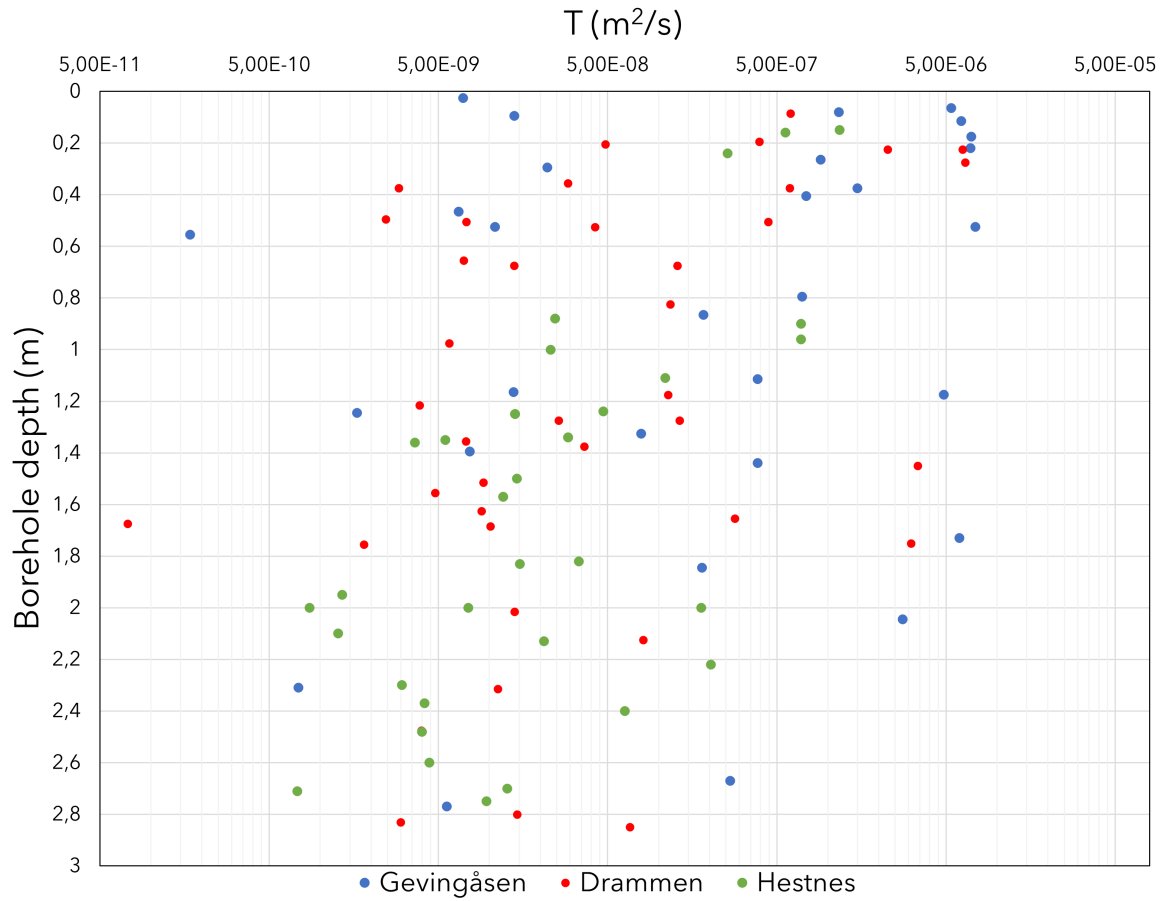


Figure 10.2: Scatterplot of transmissivity data in the Hestnes, Gevingåsen, and Drammen projects as a function of borehole depth.

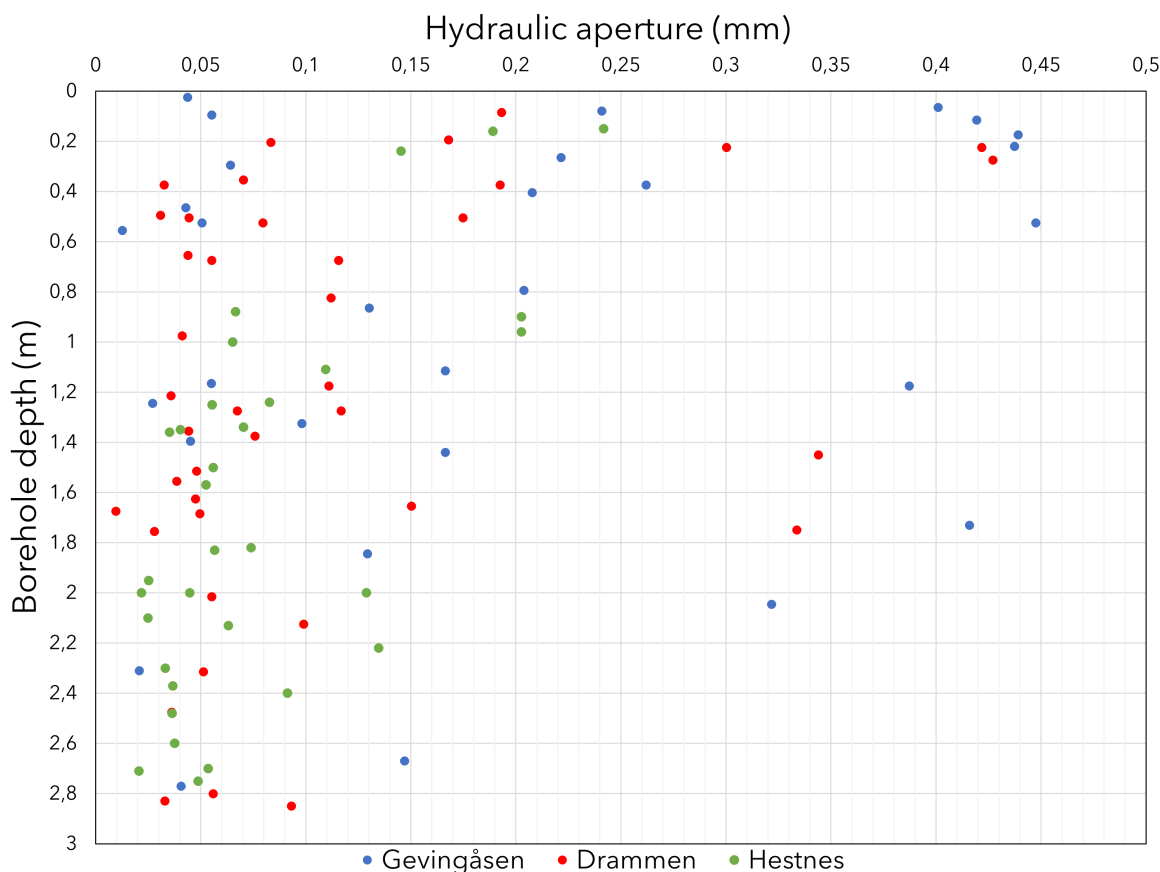


Figure 10.3: Scatterplot of estimated hydraulic aperture in the Hestnes, Gevingåsen, and Drammen projects as a function of distance from the tunnel boundary.

10.2 Results in the Hestnes project: transmissivity and aperture estimations

The gneiss had only three valid measurements in all the boreholes, and the transmissivity and corresponding aperture are summarized in table 10.1. The table also includes the only measurement in the EDZ of the amphibolite.

Table 10.1: Transmissivity and aperture estimations for all valid gneiss measurements and the one valid measurement inside the edz for the amphibolite.

gneiss			amphibolite		
Position	T	Aperture	Position	T	Aperture
[m]	[m ² /s]	[mm]	[m]	[m ² /s]	[mm]
0.15	1.8e-06	0.242	0.16	5.65e-07	0.189
0.24	2.6e-07	0.145			
2.75	9.6e-09	0.049			

Figure 10.4 shows the amphibolite's pareto distribution for joint apertures. Four measurements with transmissivities that hovered between $1e-09$ and $1e-10$ were removed for this plot, as these joints were considered impermeable. Figure 10.4 shows that the transmissivity data correlates well with a pareto distribution with a $R^2 \approx 0.92$. The probabilities for different percentiles for the transmissivity, T being higher than an arbitrary transmissivity, T_n , are given in table 10.2. The table also shows the corresponding aperture. As can be seen, the probability of the transmissivity being higher than $4.5e-09$ is 95 %, and the probability of being higher than $5.7e-07$ is 5 %. The middle value (50 %) is $1.3e-08$, equalling an aperture of 0.054 mm.

Table 10.2: Shows the probabilities of the transmissivities and corresponding aperture being higher or lower than an arbitrary transmissivity value T_n .

	$1 - P(T < T_n)$				
Probability	95 %	75 %	50 %	25 %	5 %
Transmissivity [m^2/s]	$4.5e-09$	$6.6e-09$	$1.3e-08$	$4.1e-08$	$5.7e-07$
Aperture [mm]	0.038	0.043	0.054	0.079	0.190

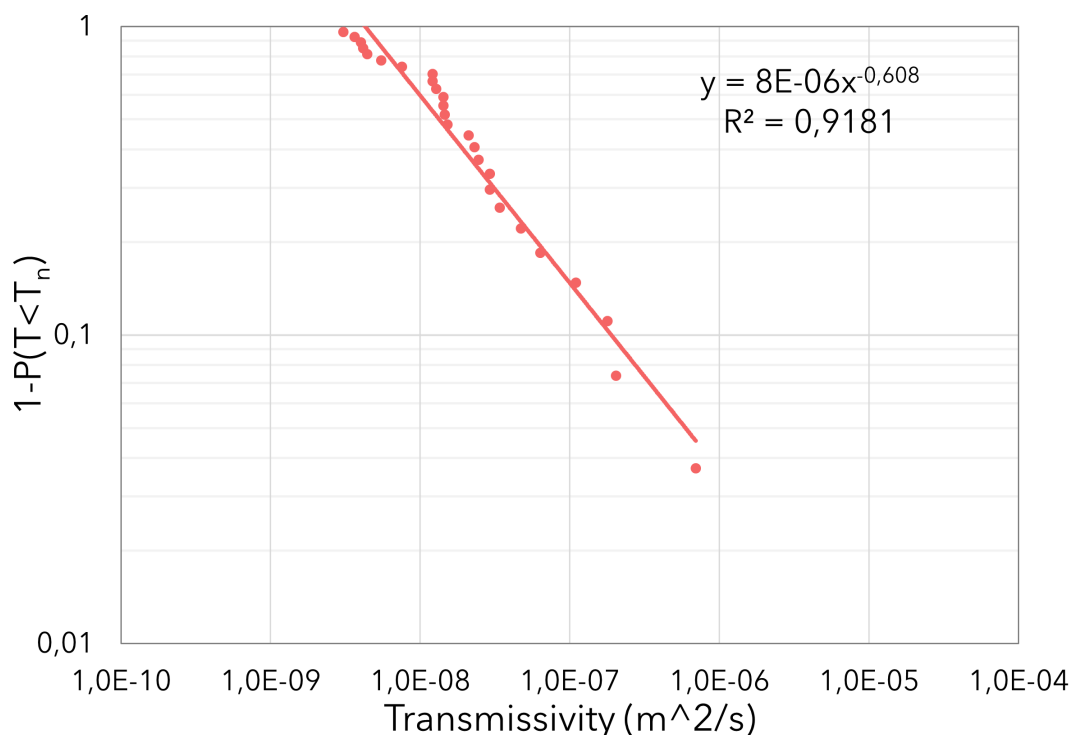


Figure 10.4: Pareto distribution for estimated joint transmissivities in the amphibolite.

10.3 Results from rock mechanical testing

10.3.1 UCS-testing

A total of 6 cores were successfully tested until failure, and the corresponding stress-strain curves are shown in figure 10.5 and 10.6. Descriptive values of UCS, Young's modulus, Poisson's ratio, and density can be seen in table 10.4. The gneiss showed a consistent UCS value with a mean of 116 MPa. The largest value was 126 MPa. The Young's modulus, as well as the Poisson's ratio, were similar between the cores, with a mean of 62 MPa and 0.27 respectively. The Amphibolite showed a larger spread in values compared to the gneiss. The largest UCS value was 170 MPa and the lowest 131 MPa. There is a discrepancy between the results of the B2 core compared to the other cores of the Amphibolite. The B2 showed a very high Poisson's ratio and a lower Young's modulus and UCS than the other cores. The calculated mean does not include these values because of observed deviations in radial displacements at the start of the test and bad linearity when measuring Young's modulus and Poisson's ratio. The failure state of all cores can be seen in figure 10.7 and 10.8. The gneiss and amphibolite showed clear signs of failure along the foliation (zig-zag pattern) and not pure shear failure, apart from core B3, which was the only core that showed crushing along the whole failure plane, which is characteristic of shear failure.

10.3.2 Tilt testing

A complete view of the test result from the tilt testing can be seen in table F.1 in appendix F. The summarized results and calculated basic friction angle (ϕ_b) are presented in table 10.3. By the recommendations of Alejano et al. (2018), the median tilt angle (α) is used to calculate ϕ_b , rather than the mean, to avoid the influence of outliers. The gneiss had a median of 27.6° , and the amphibolite had a higher median of 31.8° . The calculated ϕ_b was 24.4° for the gneis and 28.2° for the Amphibolite.

Table 10.3: Results of the tilt-testing

Rock type	Tilt angle ($^\circ$)	ϕ_b (eq.4.22)
Gneis	26.6	24.4
Amphibolite	31.8	28.2

Table 10.4: Results of the UCS-testing, A belong to the gneiss samples, B the Amphibolite.

Specimen	UCS [MPa]	Young's-modulus [GPa]	Poisson's ratio	Density [kg/m ³]
A1	126	60.2	0.25	2.75
A2	111	62.7	0.27	2.71
A3	110	63.2	0.29	2.74
Mean	116	62	0.27	2.73
B1	170	68.9	0.34	2.94
B2*	131	57	0.4	2.93
B3	149	61	0.33	2.91
Mean	150	65	0.33	2.93

*When calculating the mean the B2 results is not used for Young's modulus and Poisson's ratio because of non-linearity around the 50 % stress measuring point and deviations in radial displacement during test start.

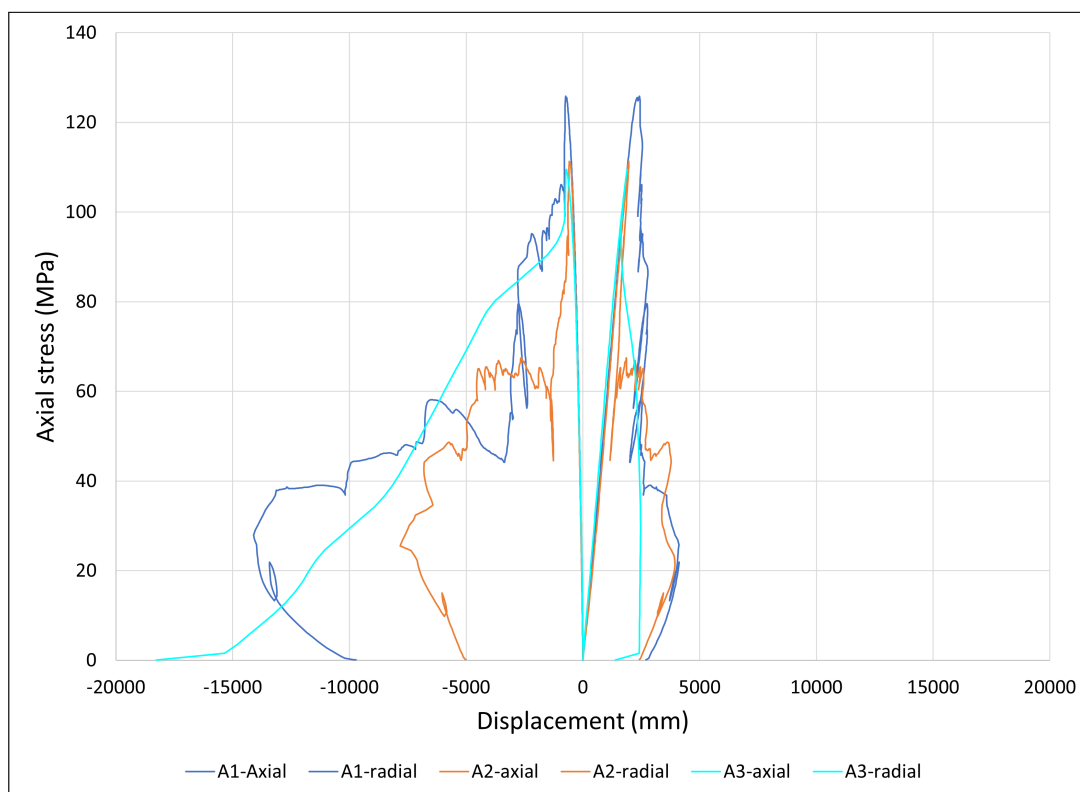


Figure 10.5: Stress-strain curves for the different rock cores belonging to gneiss, from the uni-axial compressive test.

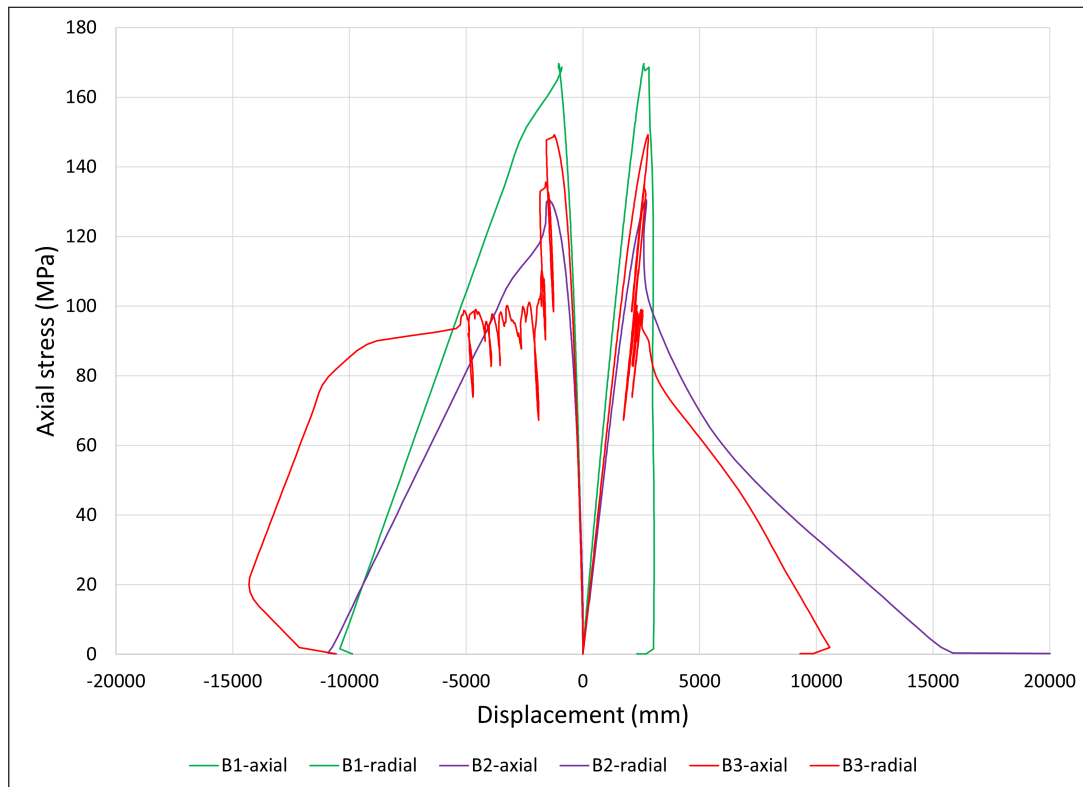


Figure 10.6: Stress-strain curves for the different rock cores belonging to amphibolite, from the uniaxial compressive test.



Figure 10.7: Yielded cores in the gneiss after UCS-testing.

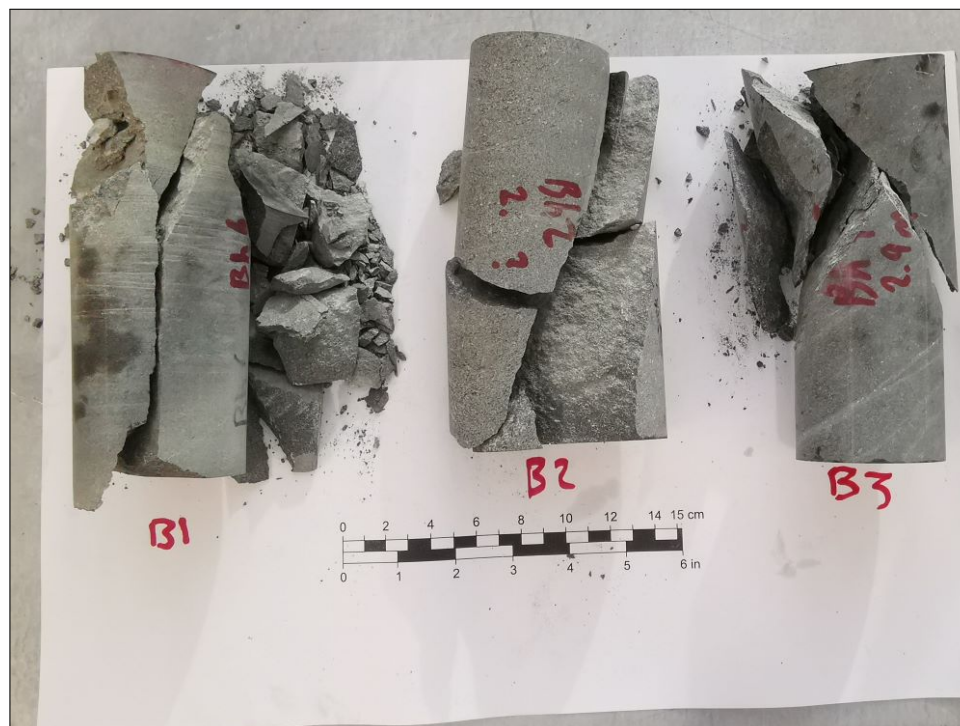


Figure 10.8: Yielded cores in the amphibolite after UCS-testing.

10.4 Joint properties estimation

10.4.1 Residual friction angle

Before the final joint input parameters K_n and K_s can be estimated, residual friction angle ϕ_r has to be estimated by the findings from field and laboratory investigations. Residual friction angle is estimated by equation 4.21. In this equation, r/R is the ratio between weathered and unweathered rock joint surfaces, i.e., R should, in principle, be equal to the UCS value of the rock. For the gneiss, which showed failure along the foliation and not a valid shear loss, the UCS is, in this case, not representative of the real rock strength and, as such, not suitable to estimate ϕ_r . However, two measurements were taken on the same joint surface of joint set J2 in the gneiss (table 8.4). Since these two sets showed significantly different rebound values, the ratio between the lowest and highest value is assumed as the weathering ratio of the joints in the gneiss.

The highest rebound value was measured on a fresh rock surface in the amphibolite. The UCS value estimated by equation 8.3 is nearly identical to the value from the lab test on the specimen that showed a valid shear failure (174 MPa and 170 MPa). Therefore, the unweathered rebound value is assumed to equal the highest reading in the amphibolite. The weathered value is considered equal to the measurement done on J3, as this was the only reading on one of the three main joint sets. The estimation of ϕ_r (based on the weathering ratio explained above) is presented in the table 10.5.

Table 10.5: Weathering degree and residual friction angle estimation from field and laboratory investigations.

Rock type	ϕ_b	r	R	Degree of weathering (r/R)	Residual friction angle (ϕ_r)
Gneis	24.4	43	49	0.88	22
Amphibolite	28.2	45	60	0.75	23.2

10.5 Discussion of joint transmissivity in Gevingåsen, Drammen, and Hestnes

The results showed little correlation between joint transmissivity and hole depth for the whole borehole. This is also to be expected because as the effect of excavation damage decreases, the transmissivity distribution should be even, independent of hole depth. This is also what figure 10.3 and 10.3 show. The results align well when compared to the findings of Ericsson et al. (2015), who found an EDZ depth of around 0.5 m. The difference in the depth of the EDZ is dependent on the charging amount, as pointed out by Ericsson et al. (2015). Hence there will be differences between different projects. Rock-type characteristics will also influence the results, for example, soft-rock versus hard-rock. The first 0.5 m had a higher frequency of high transmissive joints compared to the rest of the borehole, which supports the findings that the first 0.5 m are the most disturbed from excavation. It should be pointed out that there is no distinct separation between the in-situ rock and the EDZ; it will naturally vary along the tunnel axis and in-depth because of varying geology and other factors related to excavation.

Joint transmissivity data fit very well to a pareto distribution, as seen in figure 10.4. This also gives a reasonable estimate of the joint aperture distribution of in-situ rock, where the most probable value is around 55 μm . This is below the 100 μm aperture, which is estimated as the smallest aperture which MC can grout (if we assume $e \approx E$). This indicates that most of the finer apertures can only be grouted by CS, down to 10 μm .

A limiting factor when looking at the measured transmissivity data is the lack of data in the expected area of the EDZ. The lack of data is not due to a lack of joints but measurements that could not be analyzed. The reasons can be divided into two groups: 1) error on the part of test personnel/equipment or 2) geological factors. Some of the testing holes did experience water leakage out of the hole itself, which might indicate poor installment of the packers or longitudinal joints. However, many measurements were non-valid because water leaked into the rock mass at a rate higher than the test equipment could inject water. Some of these holes leaked out of the shotcrete; others

had no visible leakage. In one borehole, the leakage came out of an adjacent borehole around 2 m away. These observations tell us one thing; the joints in the EDZ appear open and conductive with a degree of interconnectivity or persistence. The probable transmissivity of these joints is likely several magnitudes higher than the measurements presented in figure 10.2 (for the Hestnes project).

A limiting factor in analyzing the in-situ joint transmissivity is the lack of data from the gneiss. It is observed as the main geological body at the construction site, but almost every rock core consists of amphibolite at the chosen borehole locations. Therefore the data is insufficient to analyze differences in apertures between the two rock types.

10.6 Discussion of lab results: rock mechanical properties

As pointed out in the result section, both rock types showed a lower compressive strength than expected for the respective rock types. The gneiss had a UCS value of around 116 MPa. An expected value would be closer to 200 MPa (Myrvang 2001). The recorded foliation direction was around 50° , unfavorable for getting a valid shear failure. Visual inspection also confirmed a zig-zag failure pattern along the foliation. Because of this, the real UCS value for the gneiss should be higher. The same problem was encountered in the amphibolite except for one sample, which had a valid shear failure and a UCS value of around 170 MPa (sample B3). The actual UCS value for the amphibolite probably lies around this value.

As for the tilt-testing, the values for the gneiss had a significantly lower ϕ_b than one would expect for similar rock types (Li et al. 2019). There are two possible explanations; one, the rock was very coarse-grained, which will reduce the frictional properties of the rock when the sample is smoothed. Two, the rock was observed to have low-friction minerals such as mica. The amphibolite also had lower friction angles than expected but less drastic as the calculated value is close to the standard deviation in the testing conducted by Li et al. (2019).

10.7 Conclusions regarding rock joint transmissivities and rock mechanical properties

Regarding rock joint transmissivity estimations, the following conclusions can be made:

- WPT show a higher frequency of high-transmissive joints in the first 0.5 m.
- In the Hestness project, the lack of valid measurement results close to the tunnel boundary is likely due to high-transmissive joints in the EDZ. These joints also show some persistence or interconnectivity.
- Pareto distributions fit in-situ joint transmissivity data very well.
- Estimations of hydraulic apertures indicate that most of the apertures can only be grouted by CS and not MC.

Regarding the rock mechanical results, the following conclusions can be made:

- The gneiss showed a high degree of anisotropy, and repeated failure along the foliation during testing points towards a UCS value that is likely, not representative. The same problem was encountered in the amphibolite cores, where only one measurement had a valid UCS result.
- Low friction values from the tilt-testing in the gneiss are likely due to large grain size and the presence of mica.

11 Numerical simulations

11.1 Analysis of in-situ stress and fluid flow in RS2

The simulations in RS2 includes the following models:

1. Back calculating of in-situ stresses
2. Analysis of pore pressure distribution and flow in a fluid flow-only analysis for different scenarios.

11.2 Back-calculating of insitu-stress

An important part of the input parameters in the numerical model is the in-situ stress. The magnitude and orientation of the principal stresses influence how the rock mass behaves after the railroad tunnel is excavated. The stress measurements carried out represent the stress distribution of a disturbed rock mass after excavation. Therefore a back calculating of in-situ stresses is required to estimate the in-situ stresses which are to be used in the 3DEC model. This was done by a simplified stress analysis in RS2. Table 11.1 shows the in-situ measurement data used to compare the numerical simulation results in RS2. $(\epsilon' + \epsilon'') - (\epsilon''' + \epsilon'''')$ indicate measure quality, 0 is best.

Table 11.1: Stress measurements at Hestnes.

Hole depth	E	ϵ'	ϵ''	ϵ'''	ϵ''''	$(\epsilon' + \epsilon'') - (\epsilon''' + \epsilon'''')$	σ'_v	σ'_h	Orientation from vertical
[m]	[GPa]	[μm]	[μm]	[μm]	[μm]	[μm]	[MPa]	[MPa]	[$^\circ$]
Borehole S1, with dip/dipdir of +4/302									
0.83	43.7	84	216	360	-67	7	14.8	-1	-54
1.05	54.2	49	151	261	-62	1	13.1	-2.1	-54
1.43	44.3	56	120	222	-21	-25	8.6	-0.2	-52
Borehole S3, with dip/dipdir of +4/302									
0.55	52.2	-6	-46	-21	-28	-3	-0.6	-2.3	175
0.89	58.3	48	-7	9	31	1	2.7	-0.1	11
1.19	44	28	-16	5	9	-2	1	-0.4	3

11.2.1 Method

Back calculating of in-situ stresses was done by running the model with different ratios of horizontal stresses. The vertical stress was set equal to the theoretical vertical stress

from a rock overburden of 70 m, the overburden at which the measurements were taken. The resulting principal stresses and direction around the tunnel were compared to in-situ stress measurements. The horizontal stress ratio was adjusted to find the best fit. The model was run in 2 stages to simulate the excavation, and the tolerance was set to 0.001. The constitutive behavior of the material was set as elastic Mohr-Coulomb.

11.2.2 Influence of topography

An initial assumption for the numerical simulation was a vertically orientated vertical stress equal to the overburden. The terrain is slightly sloping (16°), and the maximum height difference is around 25-30 m over 100 m in proximity to the tunnel. In general, the terrain is undulating. The topography is, therefore, likely to influence the in-situ stresses somewhat. Because the slope is deemed reasonably gentle and the tunnel overburden is significantly larger than the height difference of the slope above, the error of ignoring the topographic effect was expected to be minimal and ignored.

11.2.3 Input parameters and assumptions

The input parameters of the RS2 model can be seen in table 11.2. The stress measurements were done in the cross-cut tunnel before the split (location number 2 in figure 5.1). It is assumed that the tunnel face is sufficiently far away, so a 2D approximation is valid for the situation. The rock properties of the gneiss are used as input parameters since the gneiss was observed as the primary rock type at the site. The rock mass modulus was estimated using the equation by Palmström and Singh (2001). This equation is valid for Q-values between 1-30 and rock with $\sigma_{cm} > 150$ MPa. The lab results showed that the gneiss had a lower rock mass strength than 150 MPa, but because of non-valid shear failure along the foliation, it is reasonable to assume that the true rock strength of the gneiss is above 150 MPa. The highest mapped Q-value in the cross-cut, with a value of 22.5, was used in the calculation. Based on available maps, the cross-cut tunnel is assumed to be in the 215° direction. The direction corresponds well to the borehole direction of 302° where the stress measurements were conducted (table 11.1) if one assumes that the borehole is drilled perpendicular to the tunnel contour.

$$E_{rm} = 8Q^{0.4} \quad (11.1)$$

11.2.4 Geometry and boundary conditions

The boundaries of the model were chosen to be 6 times the excavation size. The size of the cross-cut tunnel is less than the main tunnel. The cross-cut tunnel has approx-

imately a width of 7 m, 2 m wall height, and a 3.5 m radius of the crown arc. The boundary conditions were set as rollers. The mesh was done with a graduation factor of 0.1. Figure 11.1 shows a view of the model setup.

Table 11.2: Input parameters used in the RS2 model.

Parameter	Value	Source
E_{rm}	28 MPa	Field mapping and eq. 11.1
Poisson's ratio	0.27	Lab results
Density	2.73 kg/m ³	Lab results
Peak friction angle	35°	Assumption
Peak cohesion	10.5 MPa	Assumption
Rock overburden	70 m	Site situation

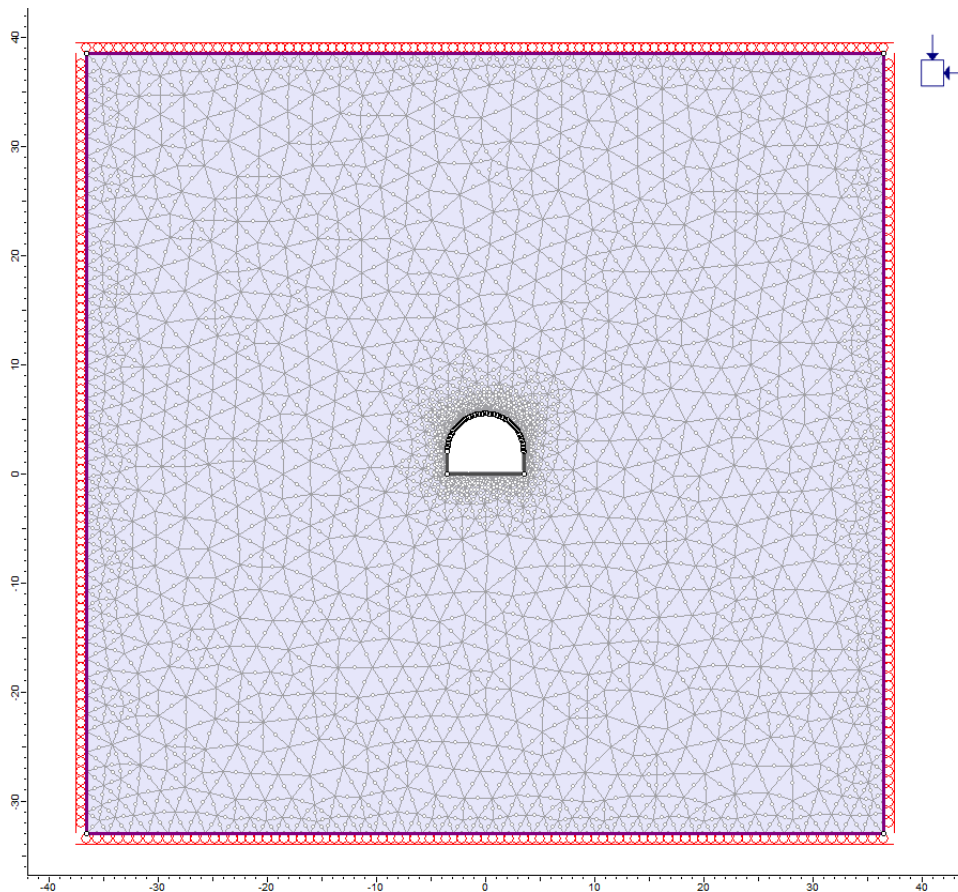


Figure 11.1: RS2 model setup. Scale in meters.

11.3 Fluid flow model

The 3DEC model included fully hydromechanical coupling and flow on rock joints, which is a complicated interaction between fluid and rock. A flow-only analysis was

done in RS2 to assess the tunnel concept in a simplified manner and for later comparison with 3DEC results.

11.3.1 Flow scenarios

A total of three scenarios was run in the fluid flow analysis:

- Scenario 1: Flow analysis with only EDZ
- Scenario 2: Flow analysis with EDZ and grouted zone
- Scenario 3: Flow analysis with EDZ, grouted zone, and permeable shotcrete

11.3.2 Geometry and boundary conditions

The model had a 50x50 boundary, identical to the 3DEC model, with a boundary distance between 3-4 the excavation size. The mechanical boundaries were fixed. The fluid boundaries had a total head of 70 m boundary condition on all boundaries to simulate constant groundwater with no drawdown. The excavation was that of the main tunnel, 14 m width, 3.5 m wall height, and 7 m radius of the crown arc. Same graduation factor as for the back-calculating model.

11.3.3 Analytical prediction of water inflow and hydraulic conductivity

Predicted water inflow was calculated for a grouted and non-grouted tunnel. The estimations serve as an important double-check of the assumed hydraulic parameters of the rock mass and the joint system in terms of the connection between the model's assumptions and the physical reality of the problem. The results of the calculations are presented in table 11.3. Hydraulic conductivity and hydraulic apertures can be found by using equation 4.6 and the principle of an equivalent hydraulic conductivity in a jointed rock mass. For this, estimations of hydraulic conductivity from literature and hydraulic apertures estimations from the lab were used. The gneiss has an estimated $k = 4.48e-08$ with a mean joint spacing of 4. The amphibolite has an estimated $k = 6.71e-08$, a mean joint spacing of 2.7. Both in-situ apertures are assumed as 55 mm, based on table 10.2.

The grouted zone hydraulic conductivity is assumed to be 1×10^{-8} m/s in rock grouted with micro cement, which is a common assumption according to Holmberg et al. (2012). It is also around the same hydraulic conductivity measured by Krokedal (2022) in rock mass grouted with micro cement. This equals an aperture of 34 μm by using Snow (1969) equation. To find the hydraulic conductivity of the silica colloidal grouted zone, an aperture of 10 μm was first assumed based on the research of Boden and Sievaenen (2005), Funehag (2008), and Hölttä et al. (2008). The calculated conduc-

tivity by using an aperture of 10 μm gave a hydraulic conductivity of 2.69×10^{-10} m/s, which is very close to the measured conductivity in the work of Krokedal (2022), and was therefore used as the joint aperture of the CS grouted zone. For the predicted inflow, only the conductivity of the CS grouted zone was used since the inflow through the invert is of less concern (the invert is only grouted with MC and drained).

Looking at table 11.3, the inflow is expected to be larger in the amphibolite, both after and before grouting, due to higher joint frequency. Both rock types are expected to have less inflow than 5 l/min/100m, and the calculated inflows are viewed as realistic for the grouted scenario. The estimations provided by different authors give close to an identical answer, which is also to be expected when $h/r > 0.3$ (El Tani 2003).

Table 11.3: Predicted inflow for solutions provided by different authors for both gneiss and amphibolite. The equations used are presented in table 4.1.

Reference	Q [m ³ /s]	LRIR [l/min/100m]	Scenario
Gneiss (S=4, k=4.48e-08)			
Karlsruud et al. (2014)	6.36e-06	38.1	non-grouted
Lei (1999)	6.36e-06	38.1	non-grouted
El Tani (1999)	6.33e-06	38	non-grouted
El Tani (2003)	6.33e-06	38	non-grouted
Karlsruud et al. (2014)	1.59e-07	0.95	grouted
Gustafson and Walke (2012)	1.56e-07	0.94	grouted
Amphibolite (S=2.7, k=6.71e-08)			
Karlsruud et al. (2014)	9.53e-06	57.2	non-grouted
Lei (1999)	9.54e-06	57.2	non-grouted
El Tani (1999)	9.5e-06	57	non-grouted
El Tani (2003)	9.5e-06	57	non-grouted
Karlsruud et al. (2014)	2.38e-07	1.43	grouted
Gustafson and Walke (2012)	2.34e-07	1.40	grouted

11.3.4 Input parameters and assumptions

Table 11.4 shows the different hydraulic conductivities given to different zones in the model. The hydraulic conductivities are based on the findings in 11.3.3 for a rock mass consisting of gneiss and a mean joint spacing of 4 m. The table also includes transition zones, with a gradual decrease in conductivity before the grouted zones, to reduce large contrasts in conductivity and synthetic flow gradients. Figure 11.2 shows how the model is built up by zones with different hydraulic conductivities.

Since there was a lack of measurements in the first 0.5 m for the Hestnes project, there is insufficient information regarding the joint transmissivities close to the tunnel boundary. The EDZ was, because of this, approximated by using the largest joint transmissivities for the whole borehole. This is likely an underestimation of the real hydraulic conductivity, considering that the joints in the EDZ might be open and conductive (section 10.7).

Table 11.4: Table shows different hydraulic conductivity and the equivalent aperture for different zones in the RS2 model. Colloidal silica (CS) is used in the walls and the crown, while micro cement (MC) is used in the invert. In addition, there is a 8 cm thick shotcrete layer with hydraulic conductivity of 5×10^{-14} m/s for scenario 3.

Distance from excavation	Hydraulic aperture	Hydraulic conductivity	Included scenario	Description
m	μm	m/s		
0 - 0.25	190	1.85E-06	1-3	EDZ
0.25 - 0.5	95	2.31E-07	1-3	EDZ
0.5 - 0.75	55	4.48E-08	2-3	in-situ
0.75 - 1	32.5	9.23E-09	2-3	CS
0.75 - 1	32.5	2,37E-08	2-3	MC
1 - 6	10	2.69E-10	2-3	CS
1 - 6	34	1.06E-08	2-3	MC
6 - 7	25	4.2E-09	2-3	CS
6 - 7	41	1.85E-08	2-3	MC
7 - 8	40	1.72E-08	2-3	CS
7 - 8	48	2.98E-08	2-3	MC

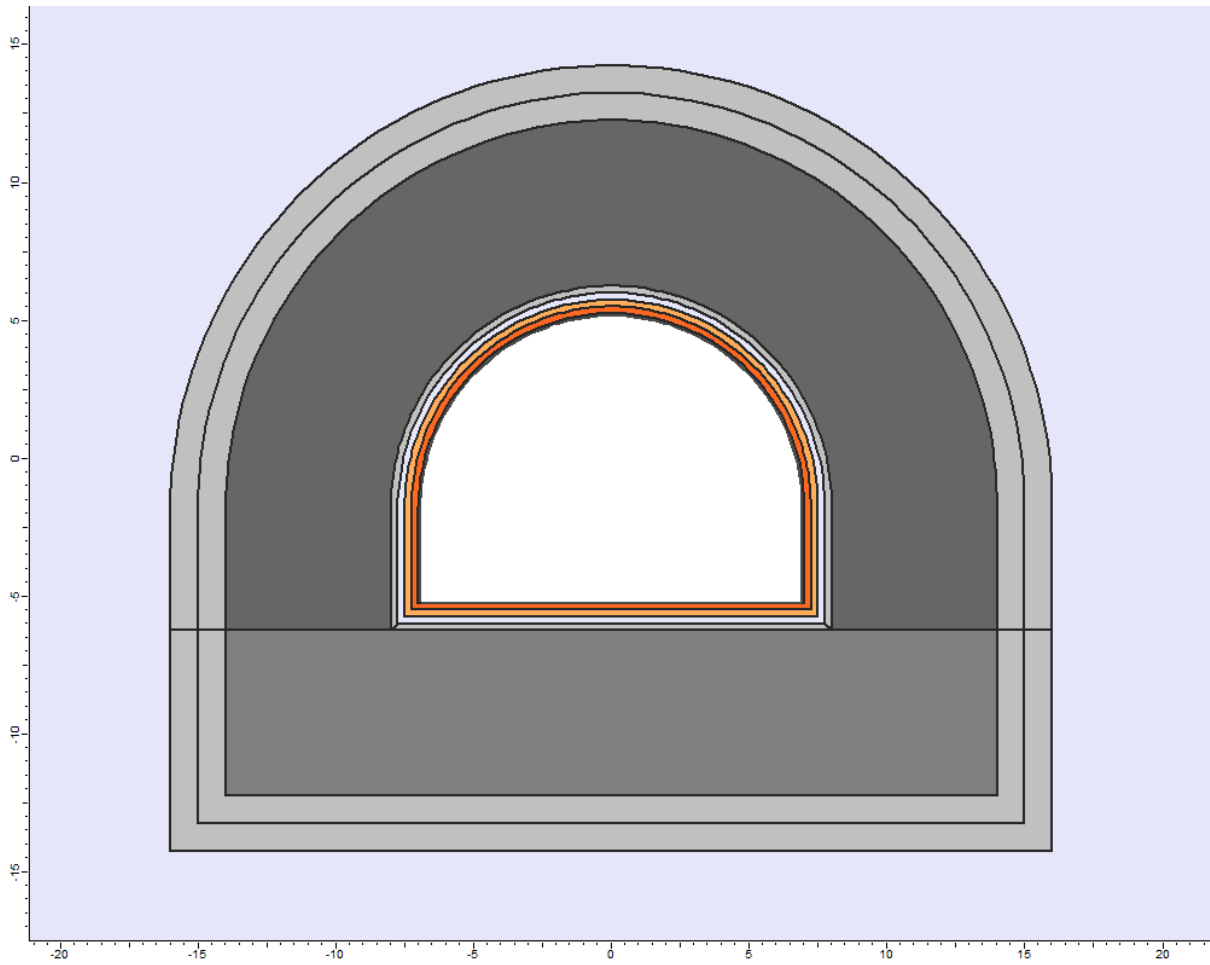


Figure 11.2: RS3 model for scenario 3 showing zones with different hydraulic conductivities. Scale in meters.

11.4 Results of in-situ stress back calculating

The result of the best fit found for the analysis can be seen in figure 11.3. The figure shows sigma one stress contours and directions around the excavations. The query on the right side shows sigma one as a function of distance from the tunnel boundary at the approximate height where in-situ measurements were done. The best fit was found using a horizontal ratio of 0.85 compared to the vertical stress. The query shows that sigma 1 varies from around 2.7-3 MPa in the area of 0-1.5 m. Compared to the stress measurement of 2.7 MPa at 0.89 m (table 11.1), the numerical results are very similar.

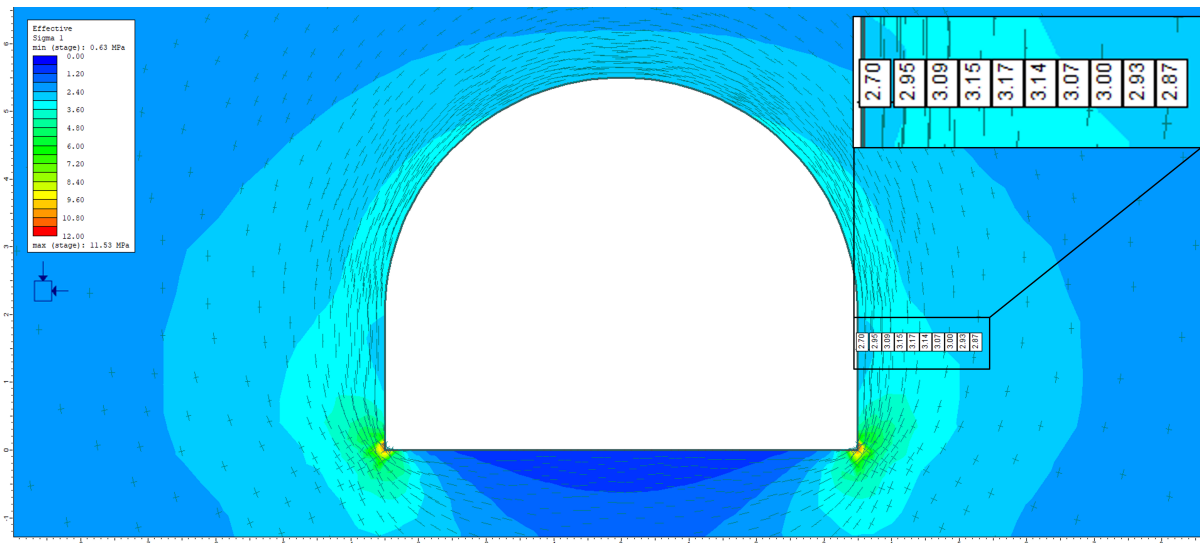


Figure 11.3: RS2 stress analysis result. Scale in meters.

11.5 Results of fluid flow analysis

Figure 11.4-11.9 shows pore pressure distribution and flowlines with total head and total discharge through the invert for scenarios 1-3. Scenario 1 only includes increased hydraulic conductivity in the first 0.5 m. Drainage is larger through the crown, which can be seen by the pore pressure distribution. The flowlines are close to uniform towards the excavation. Scenarios 2 and 3 are nearly identical regarding pore pressure and flowlines. This indicates that the grouted zone has the largest influence on the flow regime. It can be seen that for both scenarios, the flow is diverted and skewed towards the invert. For scenario 3, the discharge is increased through the invert compared to scenario 2 because of the reduced conductivity of the shotcrete. Assuming the total inflow is the same for scenarios 2 and 3, a $0.7 \times 10^{-6} \text{ m}^3/\text{s}$ difference in discharge means that the water shielding effect of shotcrete equals 4.2 liter/min/100m.

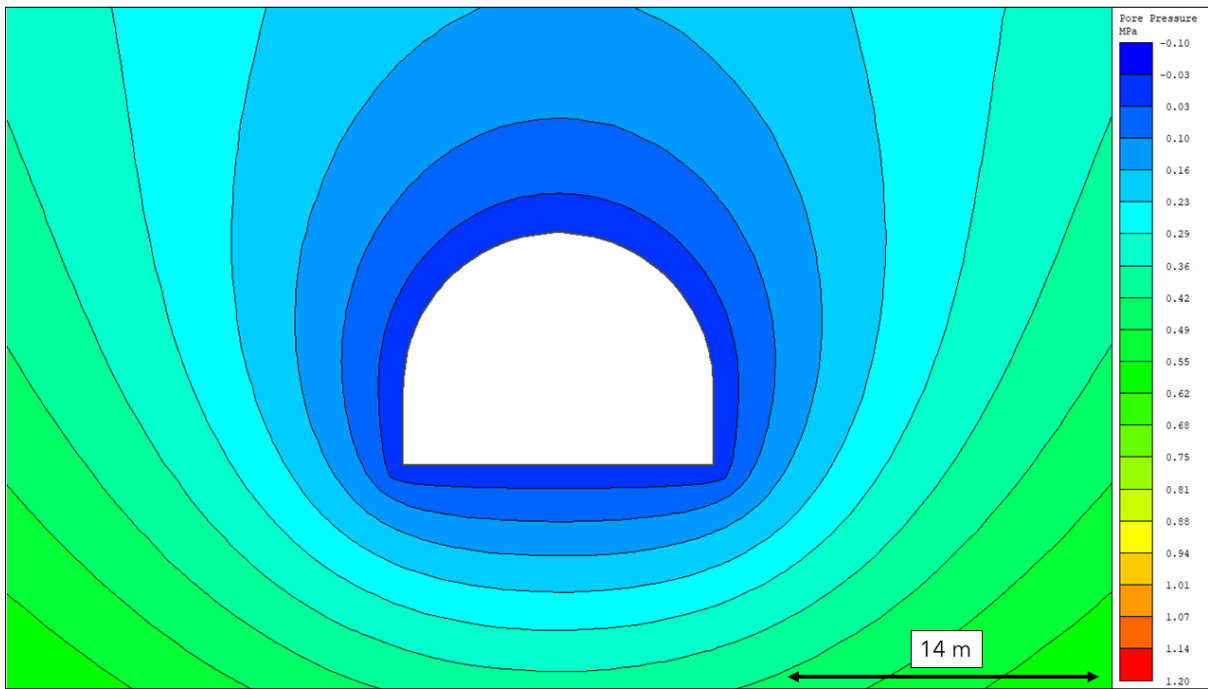


Figure 11.4: Pore pressure distribution for scenario 1 in RS2.

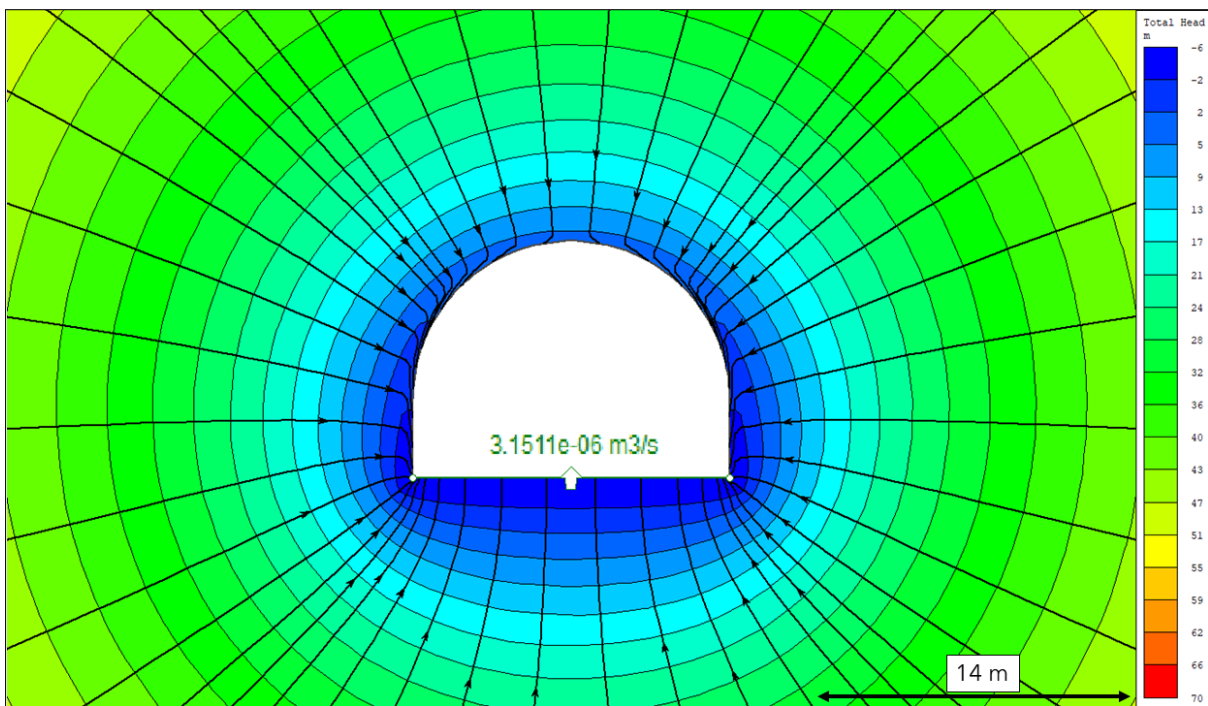


Figure 11.5: Total head and flowlines with discharge in invert for scenario 1 in RS2.

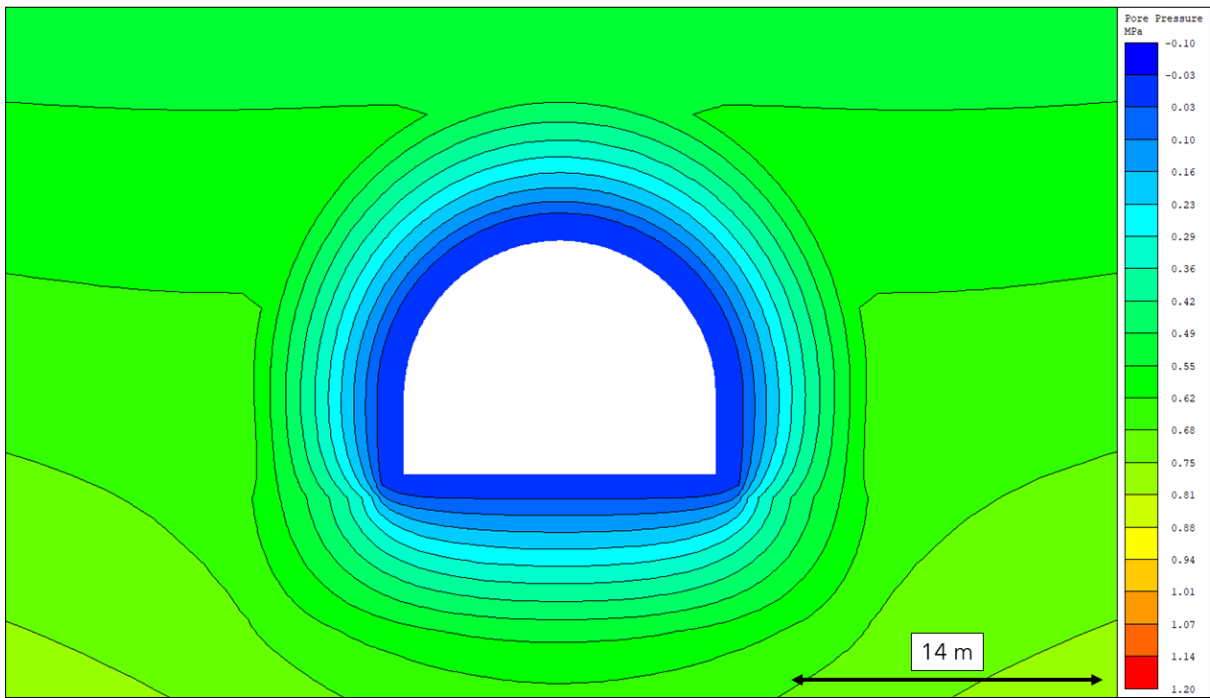


Figure 11.6: Pore pressure distribution for scenario 2 in RS2.

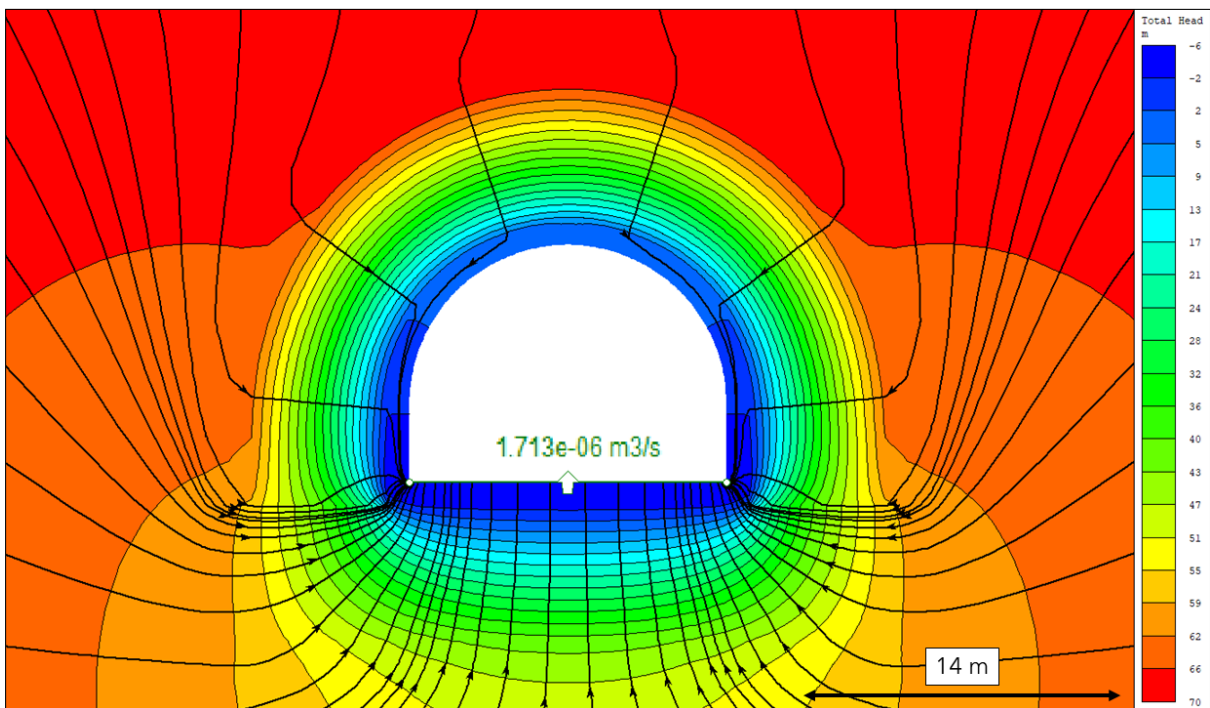


Figure 11.7: Total head and flowlines with discharge in invert for scenario 2 in RS2.

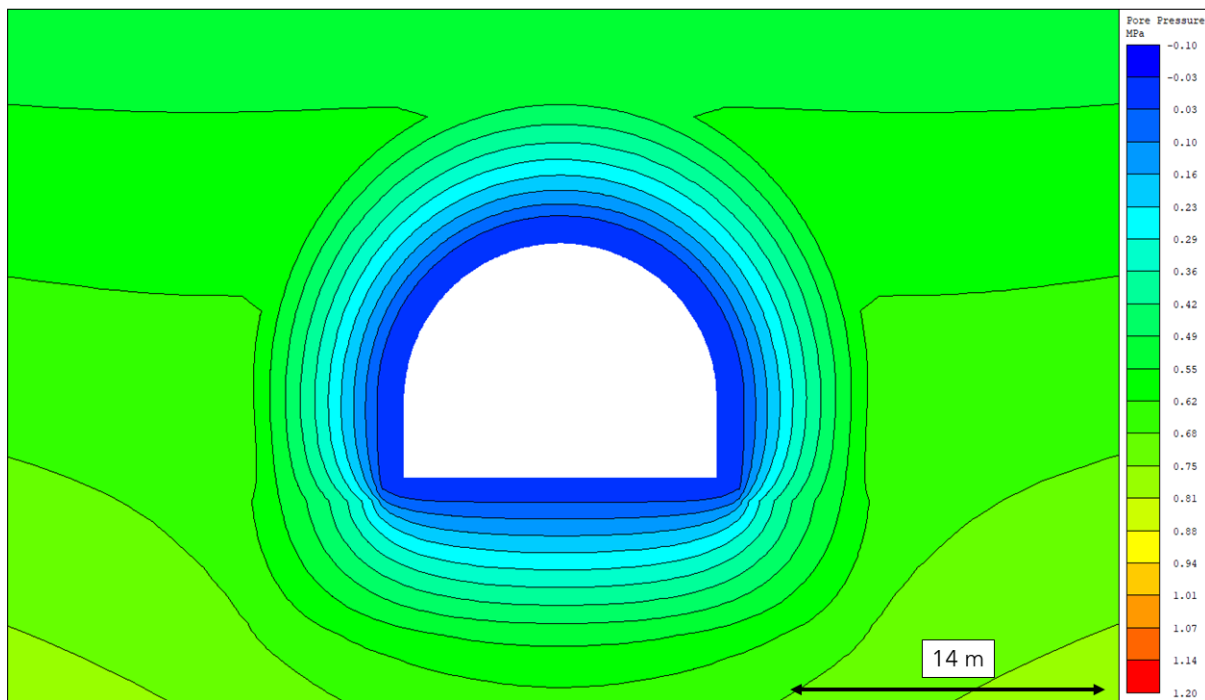


Figure 11.8: Pore pressure distribution for scenario 3 in RS2.

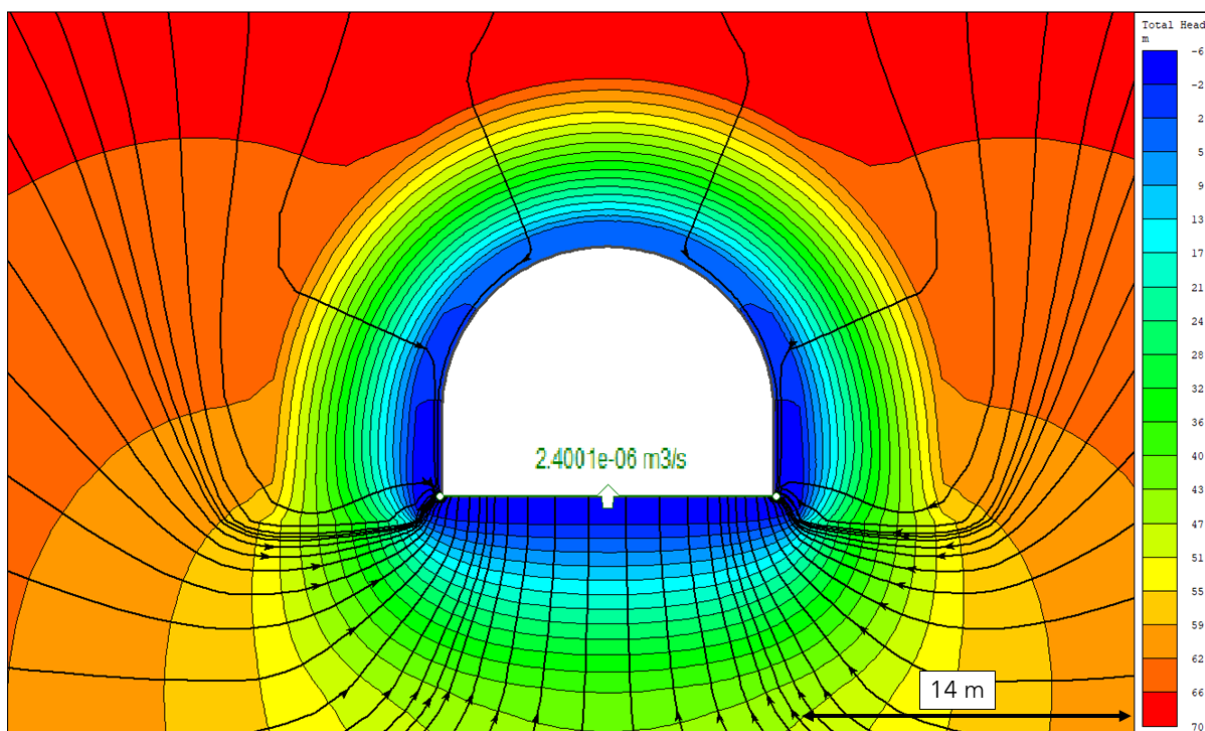


Figure 11.9: Total head and flowlines with discharge in invert for scenario 3 in RS2.

11.6 Discussion of in-situ stress analysis

By assuming a vertical stress overburden, the numerical simulation gave a similar result to one stress measurement. A closer look at the orientation estimations of σ_v in borehole s3 shows that σ_v is orientated close to vertical for all measurements. This makes a good argument for vertical-orientated stress equal to the overburden. One in-situ stress measurement fits well with the numerical result for a horizontal-to-vertical ratio of 0.85 for vertical-oriented stress. This one measurement had the best quality reading of 1 μm , calculated by the difference of displacements (0 equals a perfect reading).

An important discussion about the back-calculation results is the lack of consistency in the in-situ measurements. σ_h ranged from 0.6-14.8 MPa. A possible explanation of the disparity in σ_h estimations can be stress transfer in the joints. Because of the jointing in the rock mass, the stress distribution will depend on the joint orientation and other factors such as joint contact (e.g., zones of crushed rock will not transfer shear stress the same way as an interlocked joint, or not at all). Therefore some areas will have stress concentration and other stress relief, depending on the joints' orientation and properties.

11.7 Discussion of flow analysis

The results show that the contrast between the zone grouted with CS and MC, and only MC causes a significant alteration in the flow paths that increases the flow through the invert of the tunnel. The results also show that the shotcrete further amplifies discharge through the invert. The flowlines towards the tunnel did not change significantly from scenarios 2 and 3, most likely because of limited flow through the CS grouted zone. The model is an idealization of the tunnel concept. Since water flows primarily on joints in the rock mass, an assumption of matrix flow with a constant hydraulic conductivity simplifies the actual situation. Still, it illustrates the tunnel concept and gives a good reference scenario for the 3DEC model. Limited information about the conductivity in the EDZ region of the first 0.5 m exists. Most likely is the hydraulic conductivity higher because of open and connected joints that could not be measured.

11.8 Conclusions regarding in-situ stress and flow analysis

The following conclusions can be made from the back-calculating results:

- The assumption of vertical-orientated stress equalling the overburden seems reasonable.
- Back-calculated σ_h is approximately $0.85\sigma_v = 1.6$ MPa. With an orientation of around 125°

The following conclusions can be made from the fluid flow analysis:

- The flow paths are significantly altered by the grouted zones. The contrast between the silica colloidal grouted zone and the micro cement grouted zone causes increased flow towards the invert of the tunnel.
- The shotcrete diverts flow towards the drained invert because of its low permeability and has a significant water shielding effect.

11.9 3DEC setup

In the following chapter, the setup of the 3DEC model is presented. The following items are presented and explained; model scenarios, geometry and model size, mesh, jointing, boundary conditions, rock support, hydromechanical coupling logic, simulation stages, and model optimizations.

11.9.1 Model scenarios

Considering the complex geology at the site, it was important to find a proper way to have an appropriate representation of the geology at the construction site. The main geological body was the gneiss, with the amphibolite appearing more randomly. Because of this, a model consisting of only gneiss was chosen as the main geological model. In addition, a model with an amphibolite dyke was built, similar to the observation in figure 8.8. Early attempts at this model had unstable behavior. Because of the long calculation times in the other model, there was not enough time to build a stable model. The calculated input data for the amphibolite is still presented.

A total of three scenarios are included in the numerical simulations to evaluate the tunnel concept elaborated in section 3:

- Tunnel with stress-induced EDZ in gneiss
- Grouted tunnel with stress-induced EDZ in gneiss
- Grouted tunnel with stress-induced EDZ and impermeable shotcrete

11.9.2 Geometry and model size

A view of the model can be seen in figure 11.10. The model has a size of 50x50x50 m. To minimize numerical effects, the x- and z-direction lengths were chosen to have close to 4 times the excavation size in the model size. The excavation is a horseshoe-shaped tunnel with a radius of 7 m for the crown and a wall height of 3 m. The width of the invert is 14 m.

11.9.3 Mesh setup

Finding the proper resolution for the mesh in the model was a compromise between calculating times and model detail. A graded mesh that increases gradually with a zone size of 0.5 m from the centre to 3 m to the edge was chosen. A graded meshing allows for higher resolution close to the excavation and less detail close to the edges, where the detail is not of high concern. The resulting meshed model can be seen in figure 11.10

3DEC 7.00

©2022 Itasca Consulting Group, Inc.
Academic Model

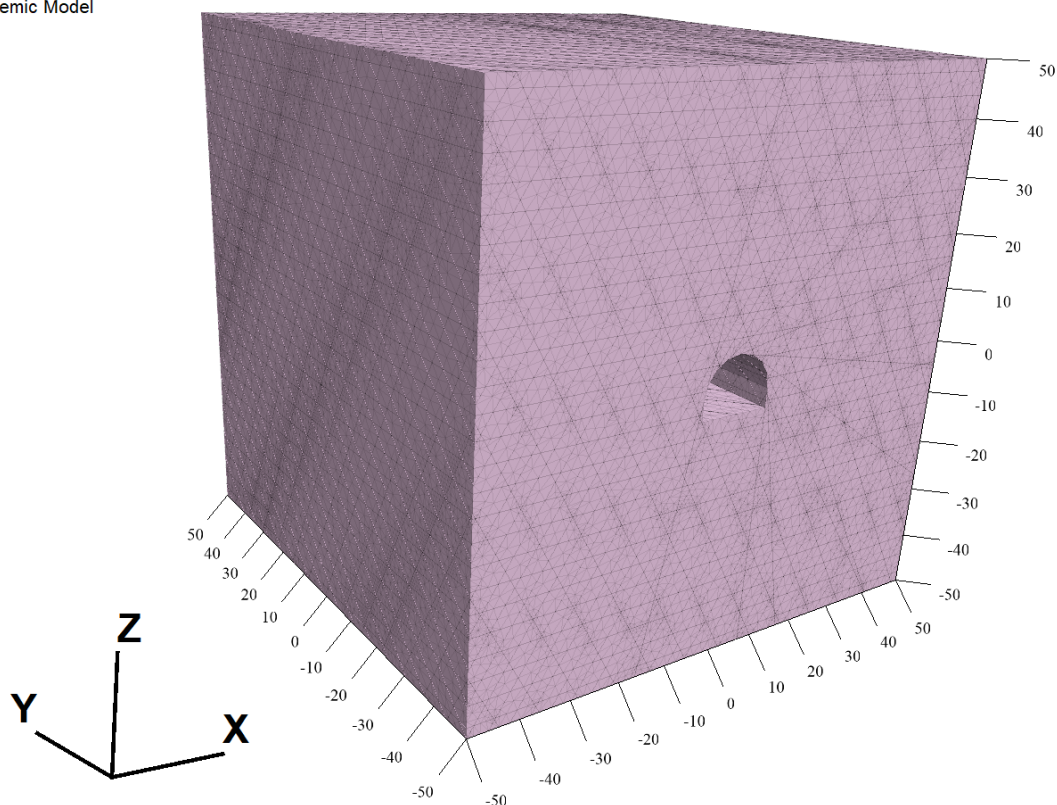


Figure 11.10: Geometry of the 3DEC model with mesh. Scale in meters.

11.9.4 Joint representation

The following joints and their properties were implemented in the 3DEC model:

- J1: 69/64 dip/dip direction. Spacing of 5
- J2: 61/258 dip/dip direction. Spacing of 3 m.
- J3: 00/00 dip/dip direction. Spacing of 4 m.

A distinct joint representation was chosen based on the mapped joint set presented in table 8.2. The joint spacings are based on field observations in 8.8 and 8.7b. All joints are represented with infinite persistence and constant spacing and orientation. The dip of joint set three had to be reduced to 0° because bad block geometries created instabilities in the initial models. Since this joint set dip is sub-horizontal, it is not expected to influence the results too much.

11.9.5 Mechanical and flow boundary conditions

All mechanical boundaries were fixed so no displacement could occur in the x , y , and z directions. According to Itasca (2019), a fixed boundary is the usual boundary condition in models where the principal stresses do not align with the boundaries of the model, which is the case in this model. The boundary conditions can potentially underestimate the stresses, opposite to a stress boundary.

The fluid boundary conditions were chosen to emulate a constant groundwater table level with no drawdown. The following boundary conditions are used:

- A constant joint pressure boundary condition was applied to the boundary planes in the x -direction and the z -direction.
- A zero discharge boundary condition was applied in the y -direction planes, normal to the tunnel direction.
- A zero pressure boundary in the tunnel invert after excavation.
- A zero discharge boundary along the tunnel wall and crown to simulate a shotcrete layer.

After excavation, a zero joint pressure to the tunnel boundary allows fluid to be drained. A zero discharge boundary was chosen to replicate a shotcrete layer with low permeability. Several considerations made this the most reasonable approach:

- The shotcrete could be replicated by giving a slice of the rock mass properties of shotcrete and turning on matrix flow. The applied shotcrete is 8 cm. Compared to the mesh size, this is a very thin layer and would generate significant problems regarding meshing and calculation times.
- The time step of the models were around 6×10^{-5} s. Expected discharge through shotcrete is around $3.5 \text{ cm}^3/\text{day}$ according to Holter and Geving (2016), which equals a discharge in the order of $10^{-11} \text{ m}^3/\text{s}$. Such a large contrast in discharge would require long solving times to reach equilibrium.

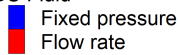
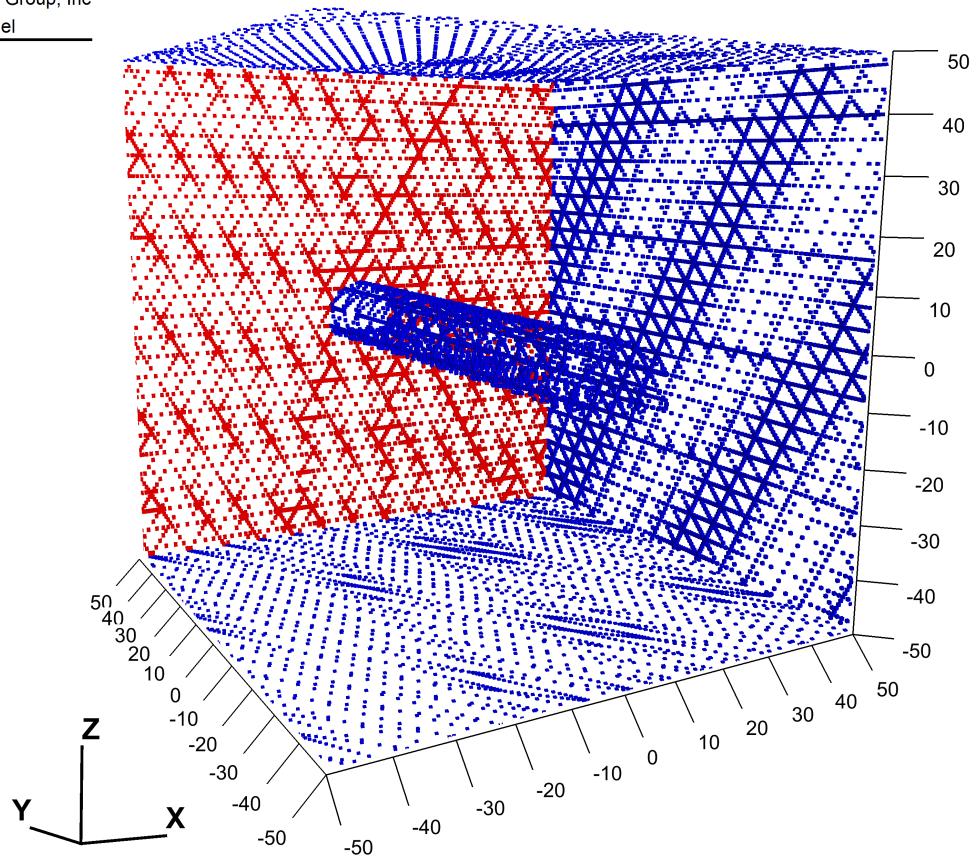
3DEC 7.00©2022 Itasca Consulting Group, Inc
Academic Model**Boundary Any**BC Fluid



Figure 11.11: Fluid boundary conditions. The x and y-planes at position -50 are cut for visibility. Scale in meters.

11.9.6 In-situ stress

Table 11.5 shows an overview of assumed in-situ stresses. σ_v and σ_h are found from the analysis in RS2, and σ_H is assumed, based on stress measurements by Pöyry in appendix A. The back-calculated stresses gave a horizontal stress of 1.6 MPa with an assumed vertical stress equal to the overburden of 1.9 MPa. Almost all stress measurements had a near-vertical stress component, making this a reasonable assumption. The direction of the cross-cut tunnel (305°) is assumed to be in the same direction as σ_H ($305 - 180 = 125$). Accordingly, the back-calculated σ_h is in the principal direction. Looking at the measured principal stresses by Pöyry, one can see that the direction of σ_H ranges from 135 - 154° , which is very close to the assumed direction of 125° . The measurements by Pöyry show that σ_H is larger than σ_v . The Pöyry measurement that gives a K around 2.5 for σ_H gave a K of 0.82 for σ_h , almost identical to the back-calculated ratio for σ_h . The direction of σ_H is 135° , very close to the assumed 125° . The chosen stresses for the model are deemed reasonable because of the good fit between the back-calculated in-situ in RS2 and the measurements by Pöyry.

Table 11.5: Back-calculated and assumed in-situ stress with magnitude and direction, at 70 m depth.

Stress	Magnitude	Direction	K
	[MPa]	[°]	[vertical/horizontal]
σ_v	1.9		
σ_h	1.6	35	0.85
σ_H	4.75	125	2.5

11.9.7 Rock mechanical properties

Table 11.6 shows the calculated rock properties used in the 3DEC model. Bulk- and shear modulus are calculated from equation 4.13-4.14. Bulk- and shear modulus is the preferred input parameter instead of Young’s modulus and Poissons’ratio because, according to Itasca (2019), the parameters (K and G) better capture the behavior of rock and prevent numerical instabilities that can occur with a higher Poisson’s ratio. Values for intact rock are used because joints are represented explicitly in the model.

The blocks are assumed to behave like isotropic elastic material. At an overburden of 70 m with relatively strong rock, rock failure is not expected outside of the discontinuities. This was also confirmed by site inspection and communication with site geologists, which confirmed that discontinuities govern the rock mass behavior. The disturbance factor is set at 0, meaning the rock properties do not change near the tunnel boundary.

Table 11.6: Rock mechanical properties.

Rock type	Density	Poisson’s ratio (ν)	Young’s modulus (E)	Bulk modulus (K)	Shear modulus (G)
	[kg/m ³]		[GPa]	[GPa]	[GPa]
Gneis	2.73	0.27	62	45	24
Amphibolite	2.93	0.33	65	64	24

11.9.8 Joint mechanical properties

The joint mechanical properties were calculated from field and laboratory investigation data. The summarized input data in the 3DEC model can be seen in table 11.7-11.8. Effective joint normal stress (σ_n) was found by decomposing the in-situ stresses in table 11.5 for the different joint sets and subtracting the joint pressure. The joint pressure was assumed to be equal to a water head of 70 m, equalling a joint pressure of 0.7 MPa. The stiffness parameters (k_n, k_s) were calculated using equation 4.27-4.32. All

joint normal stiffness values above 125 GPa/m were reduced to 125 GPa/m to maintain a reasonable ratio between k_n and k_s as recommended by N. Barton (Personal communication, May 7, 2023). Initially, the B-B criterion (equation 4.20) was used to find the joint shear strength (τ). Since the B-B criterion is not yet implemented as a constitutive model in 3DEC, the calculated parameters were linearized to the classic M-C criterion (equation 4.17) by following the procedure described by Hoek (2000).

Table 11.7: Estimated joint parameters for the Gneiss.

Gneiss									
Joint set	JRC	JCS	ϕ_r	σ_n	K_n (inter.)	K_n (mism.)	K_s	c	ϕ
		[MPa]	[°]	[MPa]	[GPa/m]	[GPa/m]	[GPa/m]	[MPa]	[°]
J1	3	140	22	1.4	268	119	0.27	0.04	27
J2	7	97	22	2.3	73	28	0.4	0.18	30
J3	5	159	22	1.2	110	46	0.23	0.06	30

Table 11.8: Estimated joint parameters for the Amphibolite.

Amphibolite									
Joint set	JRC	JCS	ϕ_r	σ_n	K_n (inter.)	K_n (mism.)	K_s	c	ϕ
		[MPa]	[°]	[MPa]	[GPa/m]	[GPa/m]	[GPa/m]	[MPa]	[°]
J1	6	105	23.2	1.4	62	26	0.27	0.1	32
J2	4	105	23.2	2.3	142	59	0.43	0.09	28
J3	4	105	23.2	1.2	74	34	0.23	0.05	29

11.9.9 Rock support

A view of the rock support parameters used in the 3DEC model can be seen in table 11.9. The diameter and bolt lengths (3 m) was obtained through communication with the site geologist. Other relevant parameters were found either through product catalogs or relevant literature. The bolts were installed with a c/c of approximately 2.

Table 11.9: Rock support parameters and source.

Rock support parameter	Value	Source
Bolt properties		
Bolt diameter	20 mm	Dywidag (2012)
Bolt cross-sectional area	315 mm ²	Dywidag (2012)
Bolt modulus	205 GPa	Modulus of steel
Bolt tensile strength	190 kN	Dywidag (2012)
Bolt strain limit	5 %	Dywidag (2012)
Grout properties		
Cohesion	1.4 MPa	Bryne et al. (2014)
Shear stiffness	7.5 GPa	Badika et al. (2022)
Liner properties		
Liner thickness	8 cm	Site geologist
Liner modulus	29 GPa	Sika (2021)
Liner Poisson's ratio	0.2	Yasir et al. (2018)
Tensile strength	4.5 MPa	Sika (2021)
Cohesion	1.4 MPa	Bryne et al. (2014)
Normal stiffness	15 GPa	Badika et al. (2022)
Shear stiffness	7.5 GPa	Badika et al. (2022)
Friction angle	59 %	Badika et al. (2022)

11.9.10 Hydraulic apertures in the model

Initially, the two rock types were planned to have different hydraulic apertures based on transmissivity estimations from WPT. Since only the amphibolite had sufficient measurements for statistical analysis, the given hydraulic apertures are based on the amphibolite data. The following apertures were chosen for the different hydraulic apertures in the model:

- An in-situ hydraulic aperture of 55 μm .
- A grouted zone aperture of 10 μm in the wall and crown and 34 μm in the invert for scenario 2-3. From section 11.3.3.

Figure 11.12 shows how the grouted zones are implemented for scenarios 2-3 before excavation. The hydraulic apertures in the two zones are forced, meaning they are constant during calculation. The thickness is 6 m. There is a transition zone between the grouted zones and in-situ rock where the apertures are set lower but allowed to open to simulate a transition zone. The first meter from the excavation can open freely to simulate stress-induced aperture changes following excavation.

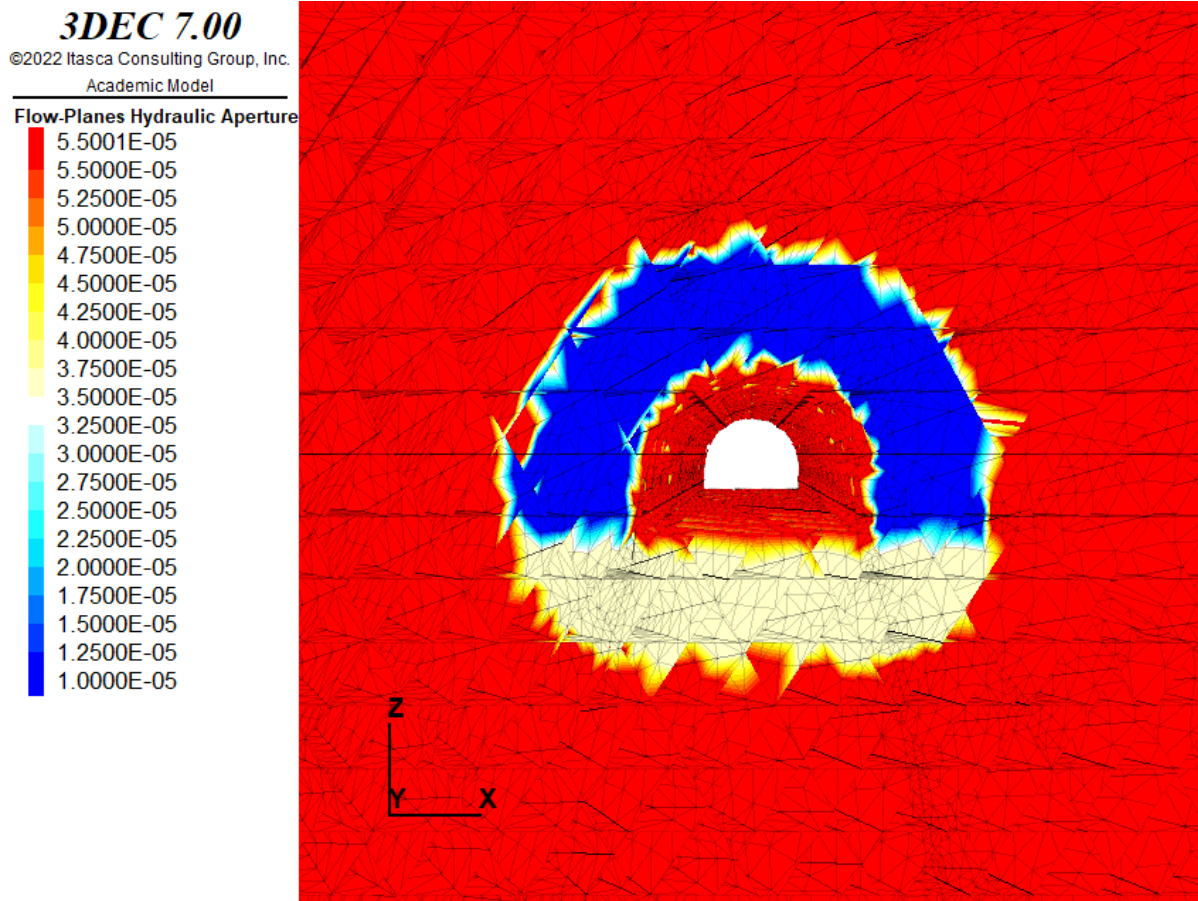


Figure 11.12: Grouted zones in the 3DEC model. Invert has forced hydraulic aperture to $34\ \mu\text{m}$, the wall and crown has forced aperture to $10\ \mu\text{m}$. There is a transition zone between the grouted zone and in-situ hydraulic apertures.

11.9.11 Hydromechanical coupling

The model was solved with fully hydromechanical coupling. The coupling logic is quasi-static, meaning the model is solved to mechanical equilibrium for each fluid step. Since this procedure would give very long solving times, the model was limited to a specific amount of mechanical substeps per fluid step, 20 in this case. This means that mechanical equilibrium is gradually achieved as the model solves through time. For the scenarios run in this study, most fluid steps were solved to a one-to-one ratio with mechanical substeps, meaning that full hydromechanical coupling was run for most of the simulation.

11.9.12 Simulation stages

The following stages were implemented to simulate the EDZ, the grouted zone and tunnel advancement:

1. Model was solved to equilibrium for the initial stress state with constant hydraulic apertures.
2. For scenarios 2-3, grouted apertures are set before the final stage. This had to be done to prevent the fluid from being trapped in the joints when forcefully decreased.
3. Fully hydromechanical simulation is done in four excavation stages to simulate tunnel advancement. Apertures can open and close.

After each excavation stage, the joint apertures that increase are given the value of $k_{n(mismatched)}$ to simulate reduced normal joint stiffness for these joints.

11.9.13 Model optimizations

The following model optimizations were implemented to reduce calculations times and increase solving efficiency:

- Limitations on the minimum flow plane area and minimum flow knot volumes to prevent small fluid time steps.
- Reduced fluid stiffness so that apparent fluid stiffness is equal to the apparent stiffness of the surrounding block material.
- The maximum joint normal stiffness is reduced (k_n) to prevent large stiffness contrasts in the model. This is also done to keep a reasonable ratio between k_n and k_s , as recommended by N. Barton. (Personal communication, May 7, 2023)
- Determinism off, meaning that the result might not be reproduced because of different round-off orders, but still within the finite-precision floating point error range and valid.

11.10 3DEC results

In the following sections, the results of the simulations will be presented. Only the most relevant properties will be presented for each scenario to limit the number of figures and information. The results will be presented in the following way:

1. Scenario one: homogenous gneiss with stress-induced apertures
 - Includes sigma one distribution, displacements, hydraulic apertures, joint pressures, and discharge lines
2. Scenario two: homogenous gneiss with stress-induced apertures and a grouted zone with reduced apertures
 - Includes joint pressures and discharge lines
3. Scenario three: homogenous gneiss with stress-induced apertures and a grouted zone with reduced apertures and impermeable shotcrete
 - Includes joint pressures and discharge lines

Stress-induced aperture changes are only presented for scenario 1, as the stress situation does not change for the different scenarios. The cut is done halfway through the model for all results showing a cross-section or an orthographic view.

For scenarios 2-3, there might be some areas in the grouted zone where the pressures are not steady state because of very low flow rates. It will likely not affect any of the conclusions drawn because it is the general trends and the big picture which is analyzed and not specific numbers.

11.11 Results scenario 1: Stress-induced EDZ in gneiss

Figure 11.13 shows sigma one stress distribution after the final excavation stage. As expected, the largest stress concentrations occur in the invert and the tunnel's crown. Relative stress relief occurs in the wall of the tunnel and propagates laterally. The largest stress is around 7-9 MPa around the excavation and the lowest around 1 MPa. Due to the effect of the joints, the stress concentrations vary greatly in different areas, even within each block. Figure 11.20 shows that displacements are larger in the walls and extend further laterally than in the crown and the invert.

A view of the hydraulic apertures is seen in figure 11.15. The maximum value is set at 80 μm , corresponding to the 75 percentile from the statistical analysis (table 10.2). Any values above are colored red. From figure 11.15 and 11.16, it can be seen that the trend is that joints open laterally from the walls but that there is variation in both the wall, crown and the invert. The joints generally close in the crown and the corner of the invert, where stress concentration occurs. Notably, the horizontal joint planes are compressed in the walls and open in the invert and the crown, see figure 11.17. In the invert, the joints open in the middle and close towards the corners. A perspective view of aperture changes can be seen in figure 11.15, showing that the apertures in the invert have asymmetrical aperture changes. This is probably a numerical effect because the in-situ stress directions are not perpendicular to the boundaries. Outside the influence zone of the tunnel, the joint apertures are in the range of 55-65 μm , indicating a slight opening of in-situ apertures.

The distribution of joint pressures and the resulting water drawdown can be seen in figure 11.18. The original hydrostatic pressure at the model's top was 0.2 MPa. From the figure, it can be seen that there is a significant drawdown of the water table because of the excavation. In the area around the tunnel excavation, the pressures are reduced by close to a magnitude of the original hydrostatic pressure due to the tunnel's draining effect. Figure 11.20 shows discharge and flowlines around the tunnel; the figure shows that the discharge is close to uniform.

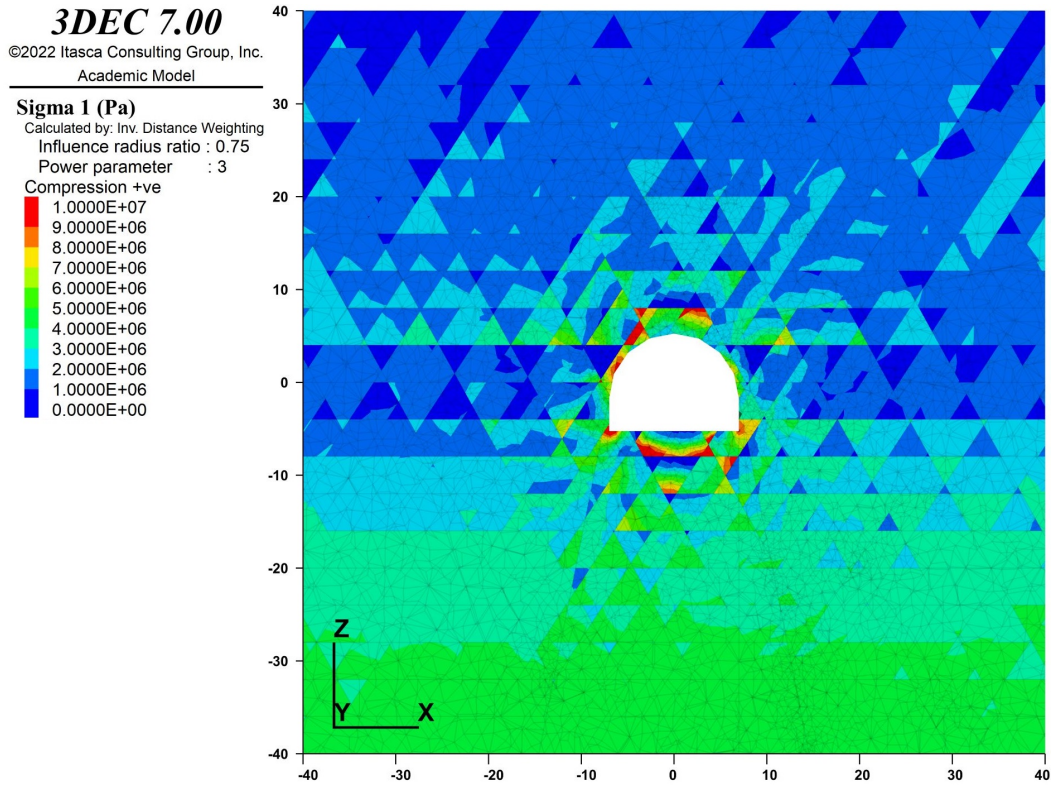


Figure 11.13: Sigma 1 stress distribution for scenario 1 after the final excavation stage. Stress concentrations happen in the invert and the crown. Stress relief occurs laterally from the wall.

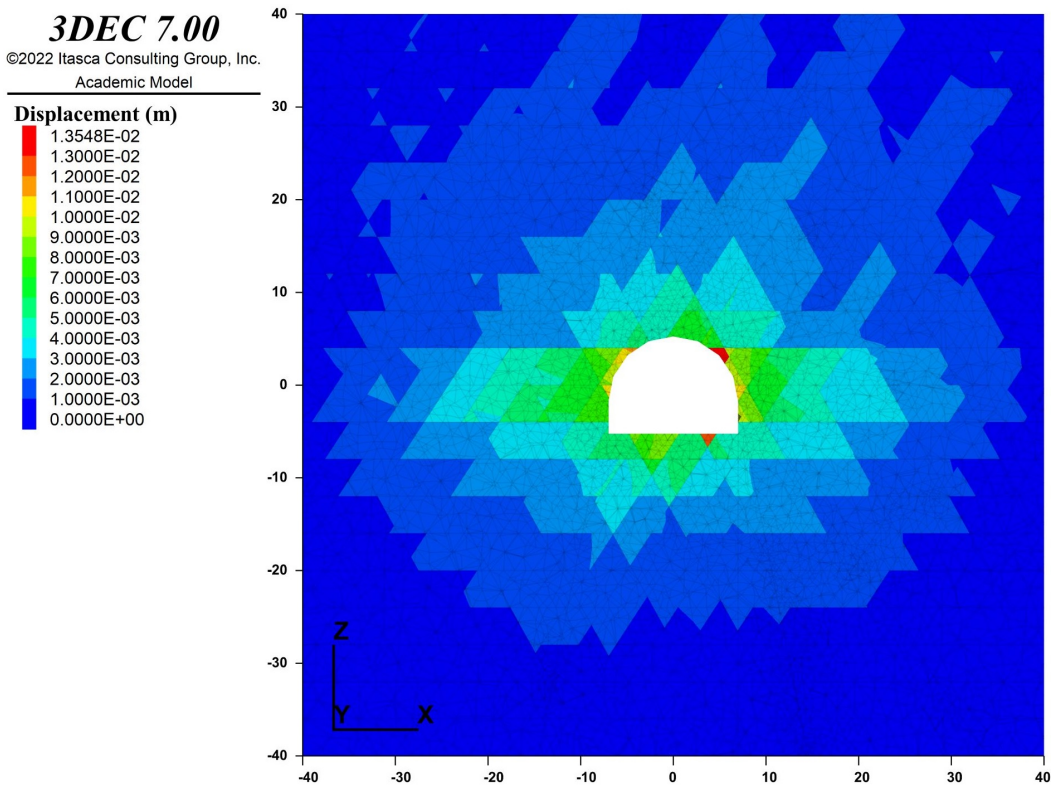


Figure 11.14: Displacements for scenario 1. The displacements are around 9 mm in the wall and extends further than in the invert and the crown.

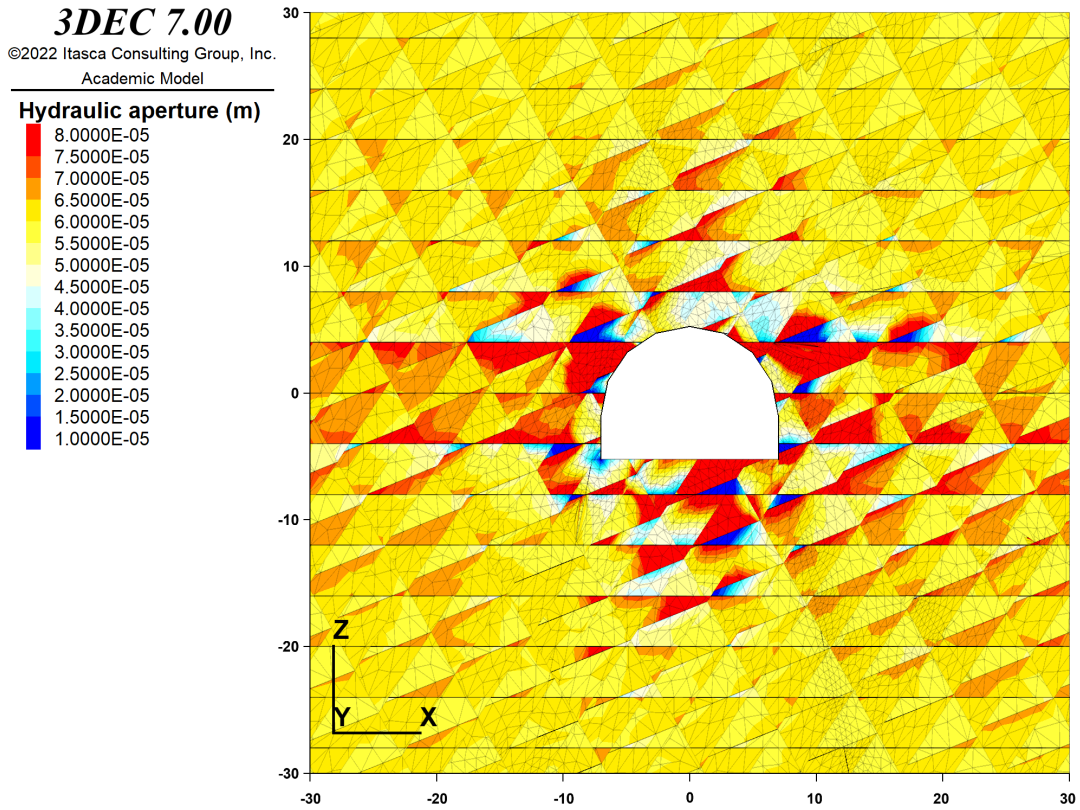


Figure 11.15: Ortopographic view of hydraulic apertures close to the excavation for scenario 1. The apertures generally open in the walls and close in the crown.

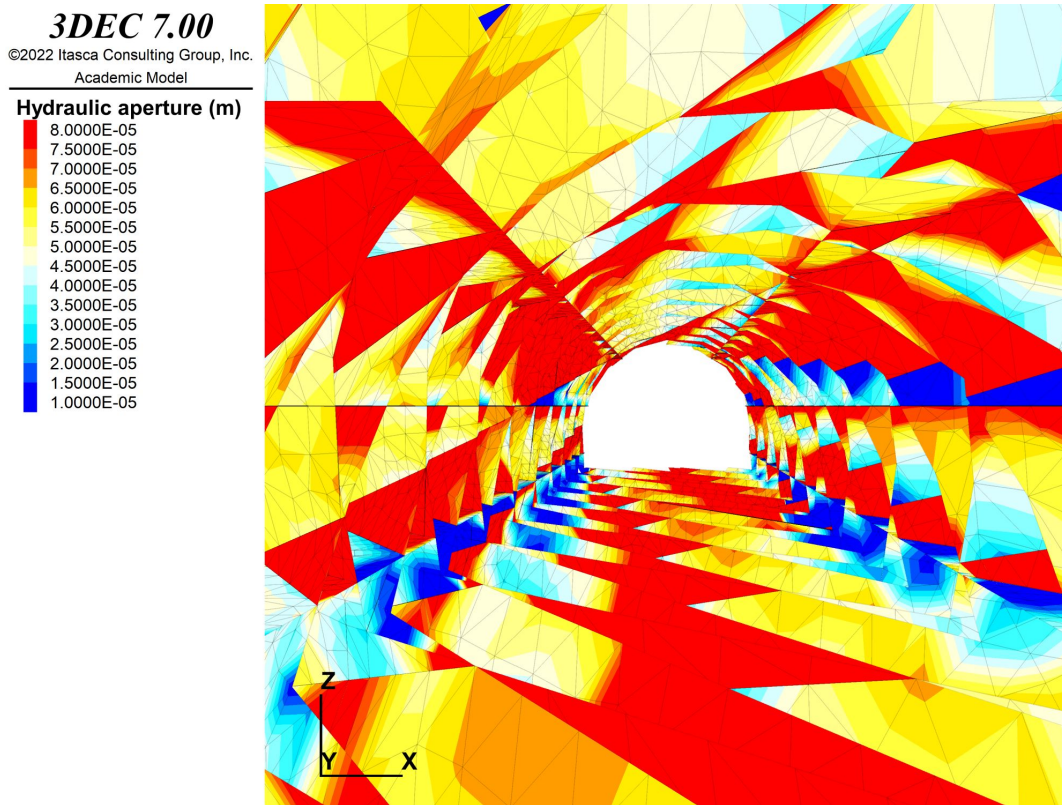


Figure 11.16: Perspective view of hydraulic apertures around the excavation contour. Joint apertures are increased in the wall and in the middle of the invert.

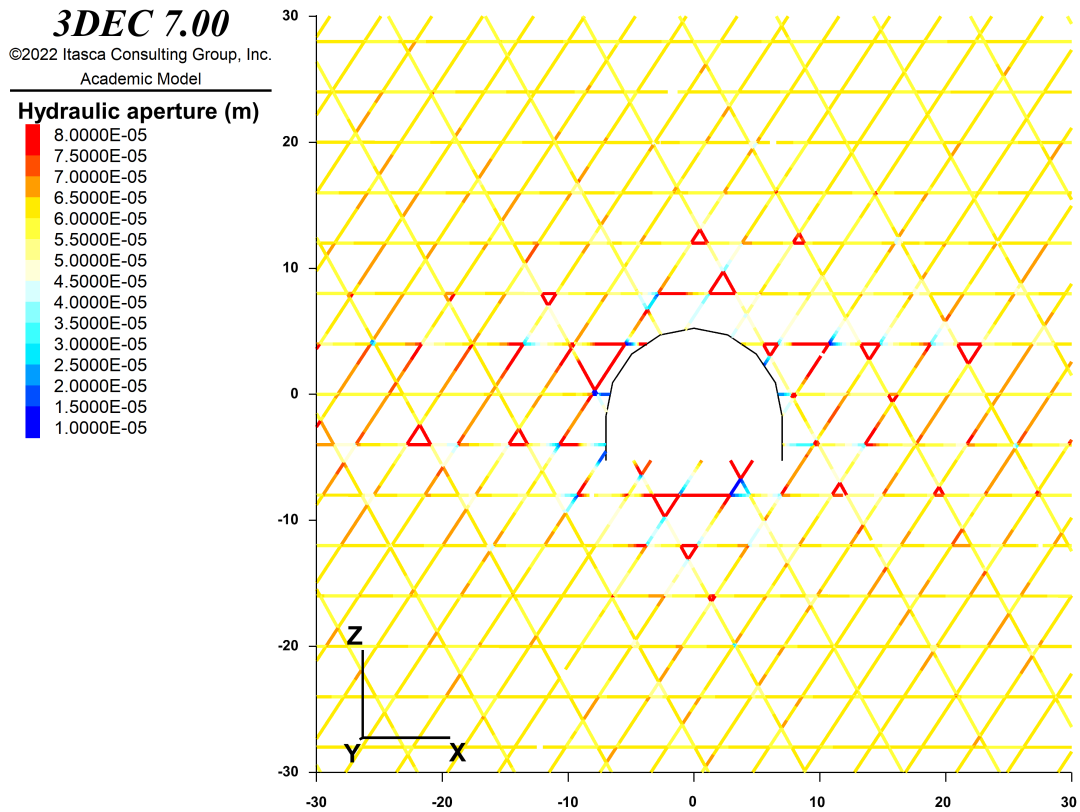


Figure 11.17: Cross-section of hydraulic apertures for scenario 1. It can be seen that the horizontal joint set opens in the invert and the crown.

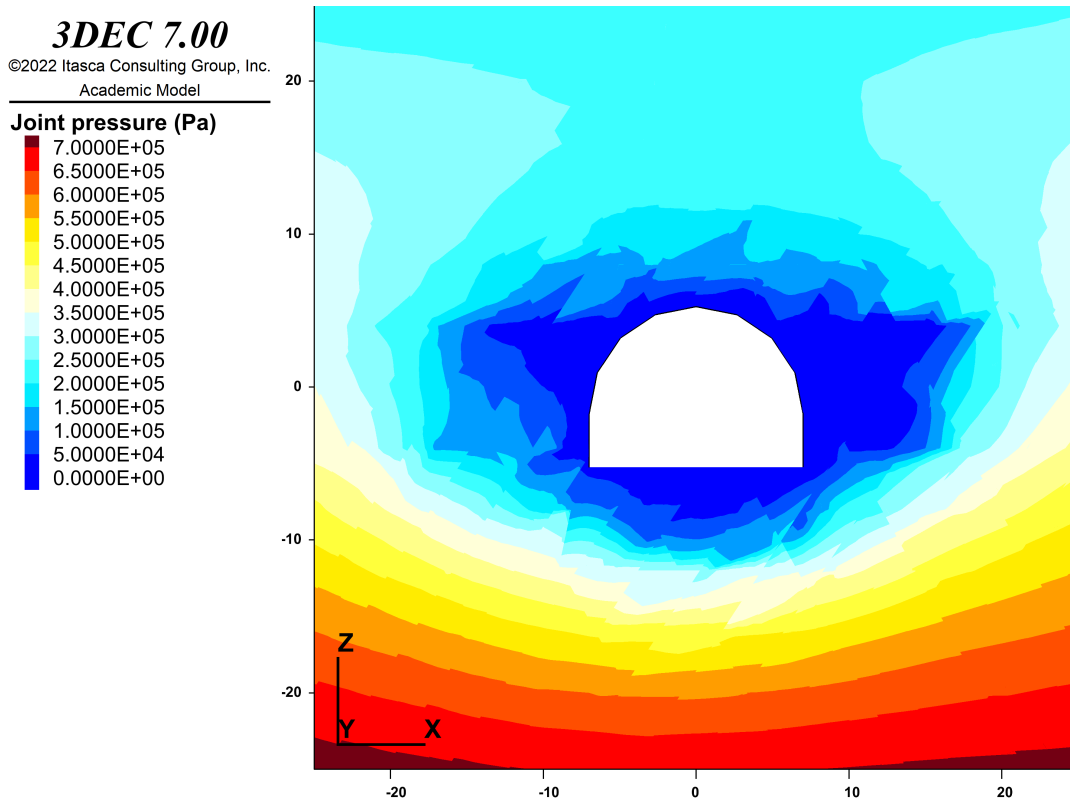


Figure 11.18: Ortographic view of joint pressures for scenario 1. There is a significant draw-down of groundwater. Pressure reduction is more prominent in the walls.

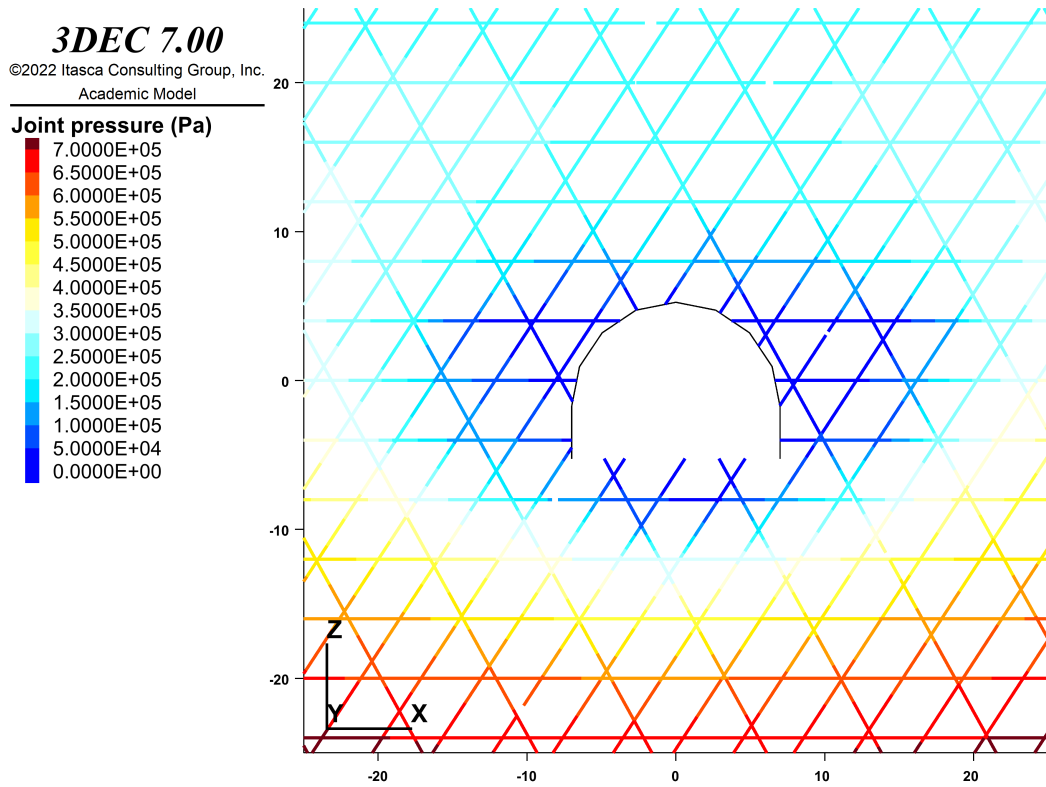


Figure 11.19: Cross-section of joint pressures for scenario 1. The pressures are lower in the wall compared to the crown.

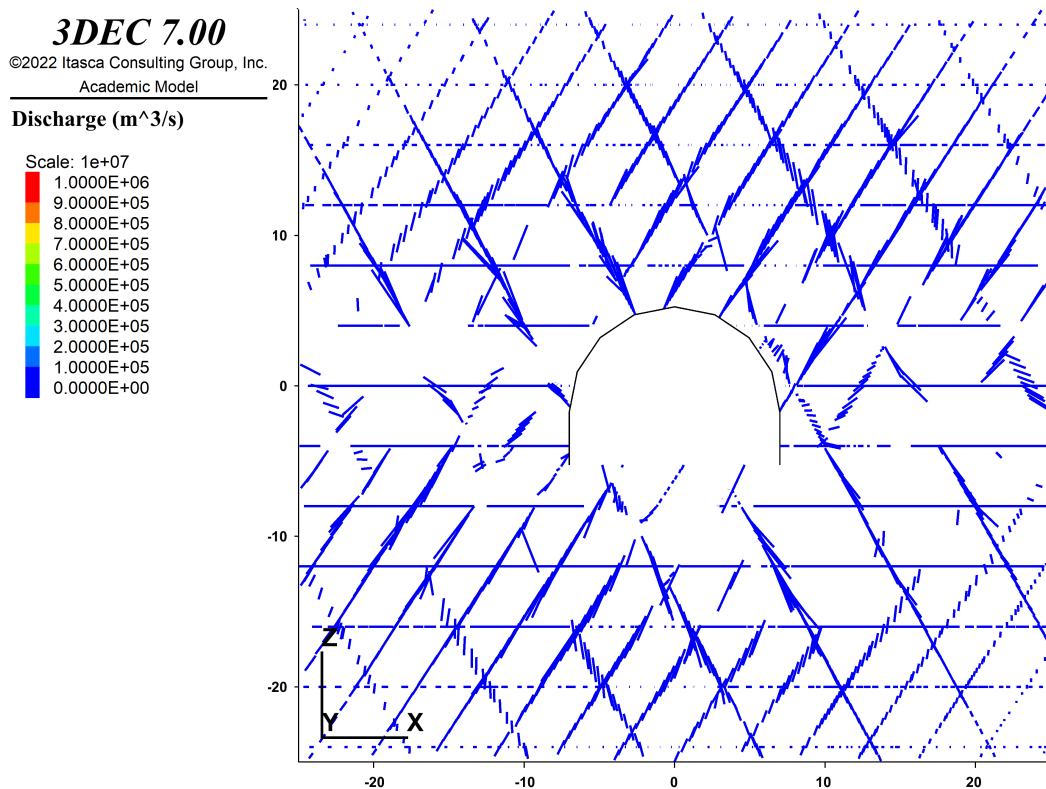


Figure 11.20: Discharge illustrated as lines for scenario 1. The lines point towards the base. The color and magnitude of the lines are given by the discharge rate. Discharge is close to uniform around the excavation.

11.12 Results scenario 2: Homogenous gneiss with grouted zone

Figure 11.21 and 11.22 shows an orthographic and cross-section view of the joint pressure distribution for scenario 2. Compared to the ungrouted scenario, the grouted scenario has less groundwater drawdown. The pressure distribution appears more uniform compared to scenario one. The low-pressure zone is also smaller for the grouted scenario than the non-grouted scenario and extends roughly as far as the grouted zone. Figure 11.23 shows the discharge flowlines. It can be seen that flow is diverted towards the invert because of the CS grouted zone and that less flow occurs in the CS grouted zone. There is also increased flow around the tunnel contour in the EDZ because of stress-induced aperture changes.

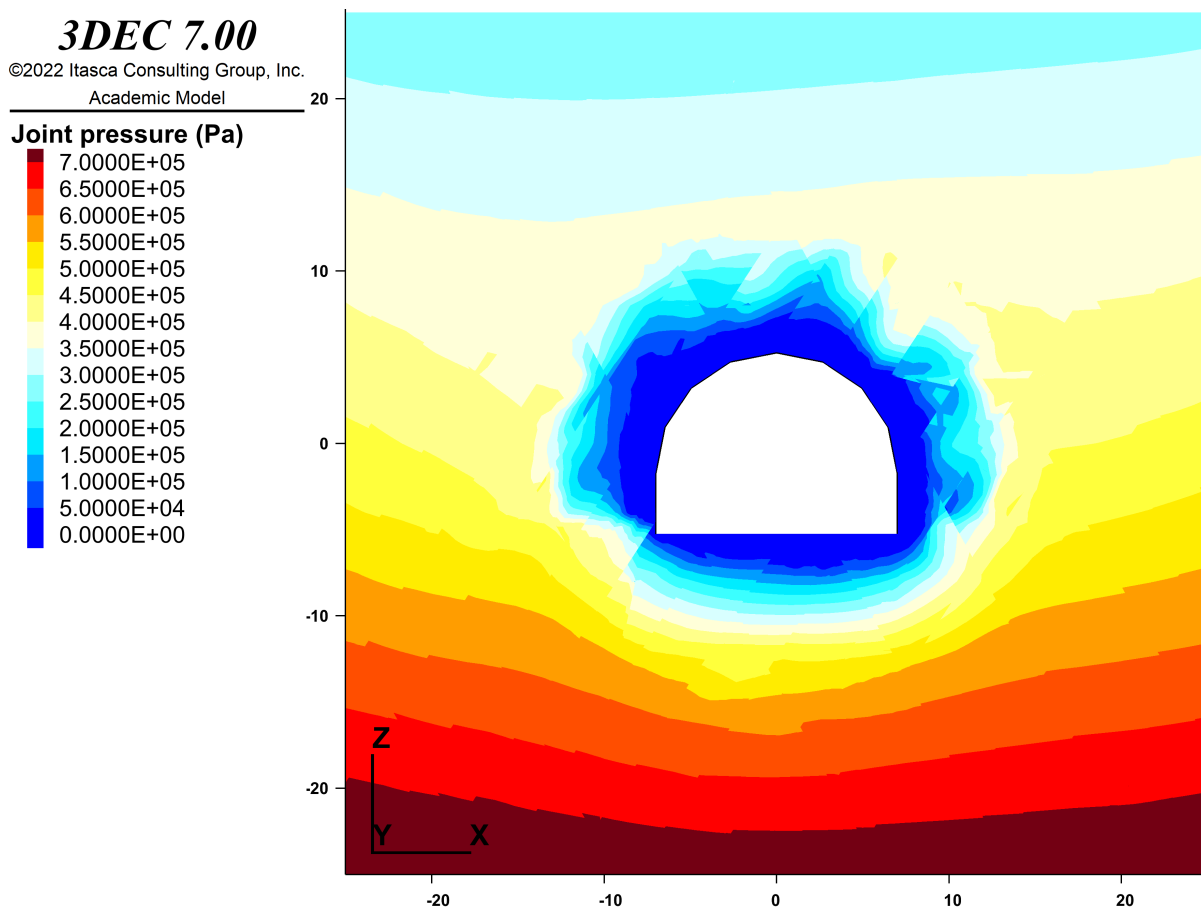


Figure 11.21: Orthographic view of the joint pore pressures in Scenario 2. A low-pressure zone around the tunnel extends roughly as far as the grouted zone.

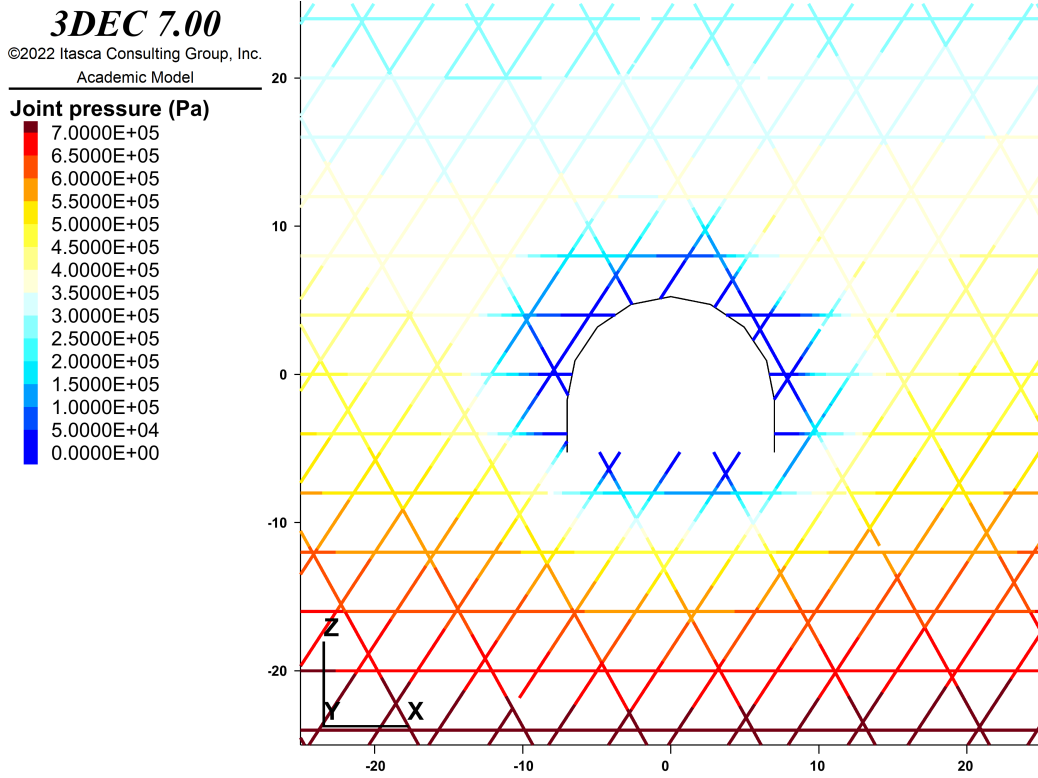


Figure 11.22: Cross-sectional view of joint pressure in the model for scenario 2. A low-pressure zone can be seen around the whole tunnel.

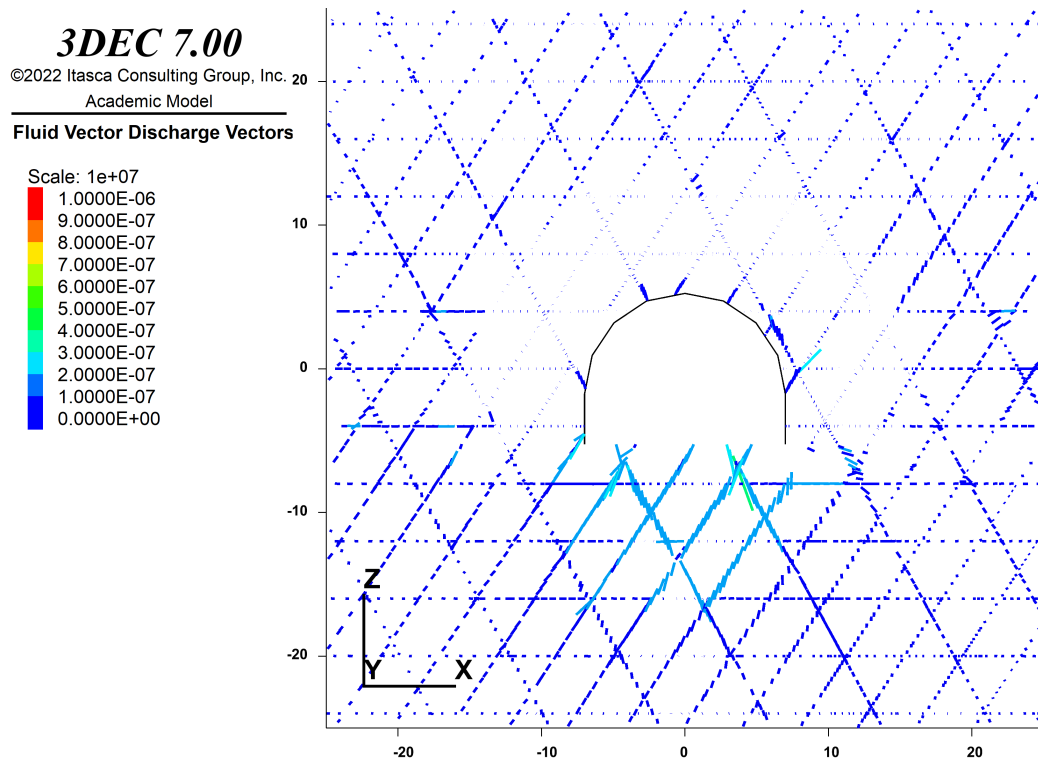


Figure 11.23: Discharge illustrated as lines for scenario 2. The lines point towards the base. The color and magnitude of the lines are given by the discharge rate. The figure shows that the flow is significantly decreased in the CS grouted zone and increased through the invert that is grouted with MC.

11.13 Results scenario 3: Homogenous gneiss with grouted zone and impermeable shotcrete

Figure 11.24 shows that the water drawdown is similar to scenario 2, indicating that more water is drained through the invert. Looking at pressure distributions in figure 11.24 and 11.25, the difference compared to scenario 2 is that the pressures are slightly higher. Still, the pressures are lowered close to the excavation, extending roughly as far as the grouted zone. This is likely due to the combined effect of the EDZ and the grouted zone. Figure 11.26 shows discharge flowlines around the tunnel. The figure shows that the flow is significantly reduced in the SC grouted zone and increased in the MC grouted zone. Flow mostly increases in the joints that open, indicating that the stress-induced aperture changes alter the flow in the EDZ. The zones with lower pressures in the first 1 m are mostly associated with the joints that open, see figure 11.15 in scenario 1 for comparison.

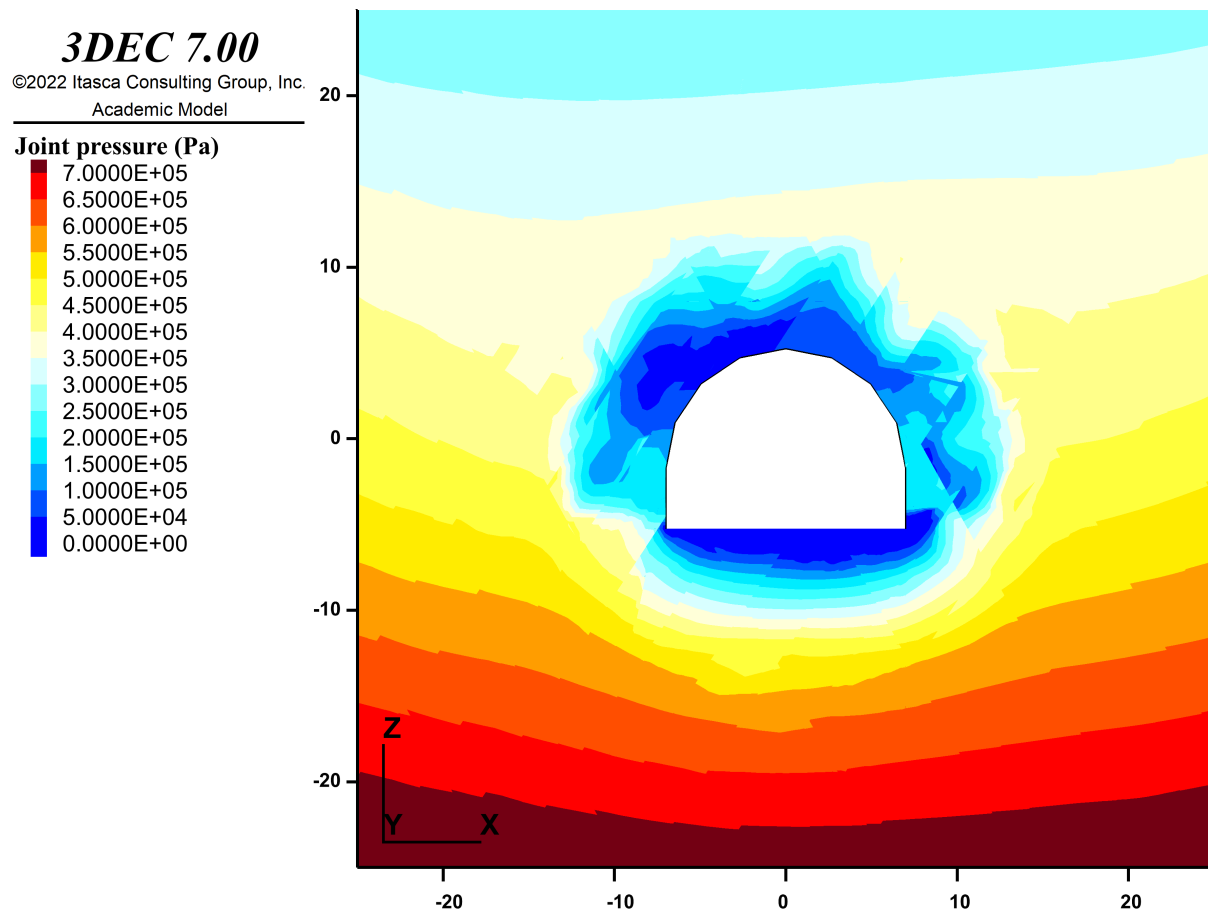


Figure 11.24: Overview of the joint pore pressures in Scenario 3. Joint pressures are reduced in the grouted zone and close to the excavation but slightly larger than for scenario 2. The largest pressure outside the shotcrete is around 0.2 MPa.

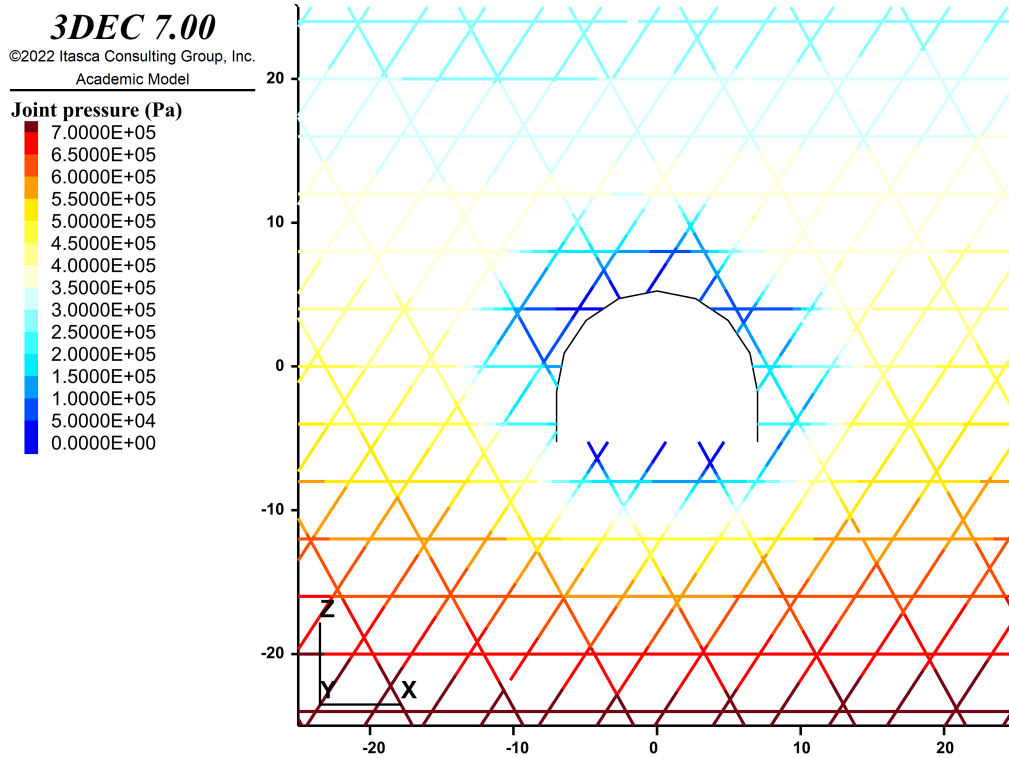


Figure 11.25: Cross-section of joint pressures for scenario 3. A low-pressure zone around the tunnel extends roughly as far as the grouted zone. Joint pressures are increased compared to scenario 2.

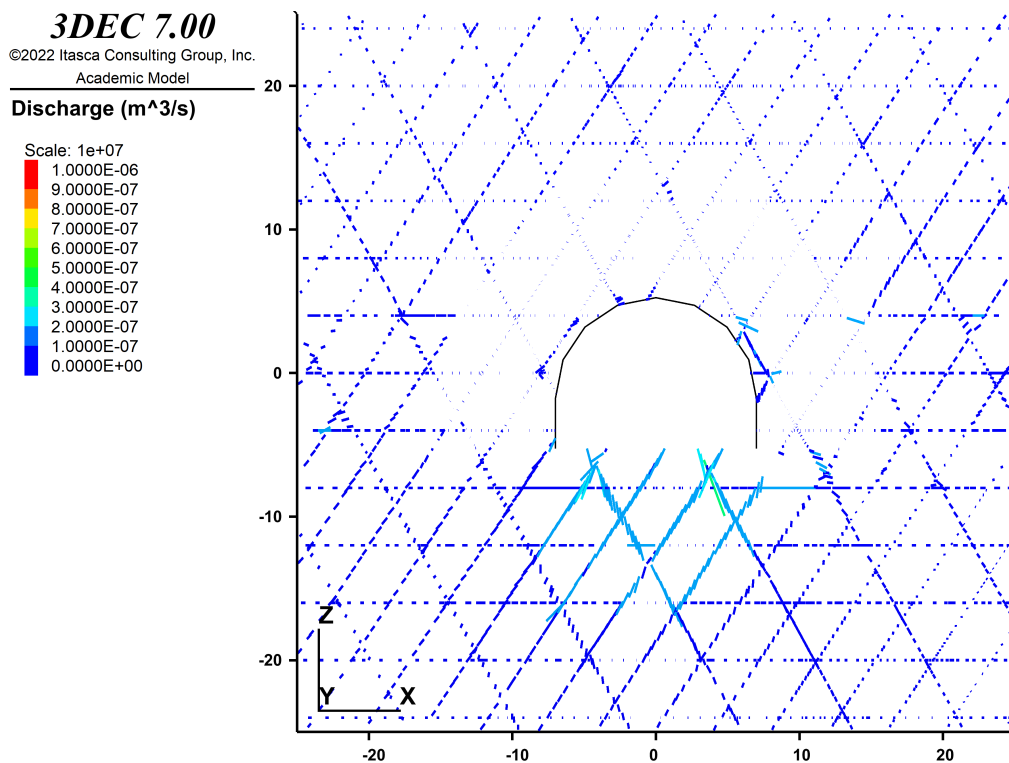


Figure 11.26: Discharge illustrated as lines for scenario 3. The lines point towards the base. The color and magnitude of the lines are given by the discharge rate. The figure shows that the flow is significantly decreased in the CS grouted zone and increased in the invert.

12 Discussion

The following sections will include a discussion of the findings in this study. Assumptions and implementation in the numerical simulations are discussed. The hydraulic properties of the EDZ based on WPT and numerical simulations are discussed. A discussion is made on the main findings concerning the tunneling concept.

12.1 Validity of joint properties

The cubic law and the hydraulic aperture are used in the flow calculations in 3DEC. The hydraulic aperture is a simplification of the larger physical joint aperture. With increasing smoothness and planarity, the physical and hydraulic aperture approaches each other, making the approximation more valid. However, as roughness increases and the asperities of the rock joints creates more contact area, the difference between the physical aperture and hydraulic aperture increases (Barton 1982). The rock joints mapped in the Hestnes tunnel are generally planar with JRC values from 4-6. Therefore, the error of using the hydraulic aperture is not expected to be large. Another aspect is how the closure or opening of joints affects the validity of the cubic law. As joints close, the contact area of the asperities decreases, and the flow complexity increases as the fluid is forced to flow between asperities.

Laboratory investigations by Witherspoon et al. (1980) show that the cubic law is valid regardless if the joints open or close. A study by Alvarez et al. (1995) found that there is a linear relationship between closure and hydraulic aperture for stresses lower than 25 MPa. Since the assumed stresses at Hestnes are well below 25 MPa, hydraulic aperture can predict flow in closing joints realistically. The assumed hydraulic aperture could predict flow well in all studies included in the review by Alvarez et al. (1995). Based on the findings of Alvarez et al. (1995) and Witherspoon et al. (1980), the error of using the cubic law in a hydromechanical scenario with closure and relief of joints is probably not too large.

The 3DEC scenarios include joints with infinite persistence and constant spacing. All joints are also saturated. This assumption is probably unrealistic compared to the in-situ situation. Several leakages at the Hestness project have been observed to be concentrated in a single spot, not constant seepage from all the joints. This indicates that the fluid flow occurs in a more channel-like flow in a 1D network, not a 2D network, which is the assumption in the numerical simulations. This is probably the case, especially in the non-grouted tunnel, which is also evident from the results, that some open joints influence the flow distribution significantly more than others. The joint properties are assumed as constant but as figure 8.12-8.14 and figure 8.16 illustrates,

the values for JRC and JCS vary within the rock types and the joint sets. Some of this is accounted for by giving different properties for the respective joint sets, but the conditions are likely not as uniform as assumed in the model.

The jointing is likely higher close to the tunnel excavation due to blasting damage. A more sophisticated DFN model could replicate this situation more accurately. This was done by Wang and Cai (2020), who created a zone within the EDZ with different fracture intensities. The study only considered mechanical response, but if the same model could be built for a hydromechanical analysis, it could solve some of the shortcomings mentioned.

12.2 Implementation of the grouted zone

There are certain limitations with the implementation of the grouted zone in 3DEC. The amount of water-bearing joints in the model is the same before and after reducing the apertures. In a real scenario, the amounts of open joints would be decreased because open joints are filled with grout material. Discharge may be exaggerated because of too many water-bearing joints in the grouted zone. A possible workaround is to disable joints above a certain aperture size after the excavation. Matrix flow could also have been enabled instead of joint flow in the grouted zone. Hydraulic conductivity of the grouted zone is easily measured in the field and easier used in numerical modeling compared to reducing apertures. Long calculation times in the order of weeks prevented experimentation of these options. The strength of the chosen implementation is that it captures how contrasts in joint apertures influence the flow directions around the tunnel boundary. The results are similar to the RS2 results in how the fluid flow, which give cause to believe that the 3DEC model captures some of the essential behavior a grouted zone will have on fluid flow.

12.3 Implementation of the EDZ

Originally the 3DEC model was planned to include excavation-induced damage. Because WPT gave very little information regarding the transmissivity in this area, blasting-induced damage was not included. Early attempts used the highest values from the WPT and set the hydraulic apertures based on these transmissivities in the first 0.5 m, like the RS2 model. Early test runs of the model showed that the stress-induced aperture changes were mostly larger than these values. Hence, it was decided to do a conservative approach and not include blasting-induced damage. Blasting-induced damage was initially planned to be implemented by setting the minimum hydraulic aperture equal to the initial aperture so that apertures in the construction damage zones are forced to be larger. There are some limitations to this method:

- Microcracks due to blasting damage are not included.
- Re-activation of healed joints is not included.
- Joints exposed to compressional stress are forced to stay open.

If the minimum aperture is increased close to the tunnel, it is expected to reduce the joint pressures. For the results of this implementation, the author refers to the work of Nilsen (2019), who included blasting-induced damage by limiting the minimum apertures in a scenario for a partially drained tunnel with an impermeable membrane. The findings showed significant joint pressure reduction close to the tunnel boundary. The work did not include the grouted zone, as is the case in this study.

12.4 Comparison between RS2 and 3DEC analysis

One of the major differences between the RS2 and 3DEC models is that RS2 uses matrix flow. Accordingly, water flow is continuous in the whole model. If the flow paths in the EDZ are continuous, it will likely be a significant draining effect. This can reduce hydrostatic pressure acting on the shotcrete, as shown by Holter (2015). Assuming a continuous and connective EDZ might be too optimistic. The literature is not clear whether the EDZ is continuous or not. Studies conducted by Ericsson et al. (2015), Mellanen et al. (2009), and Olsson et al. (2004) found no clear evidence of continuous flow paths. Hence, the RS2 should be treated as a concept model and might represent too optimistic flow in the EDZ.

Most of the joints in the 3DEC model show a significant pressure reduction in scenario 3. This indicates that stress-induced aperture changes increase flow towards the invert. Some joints have higher pressure because little flow occurs and are closed because of stress redistribution. The zone grouted with CS reduced flow significantly, and there is very little inflow in the EDZ from the CS grouted zone. The joint pressures are also reduced since the EDZ is more conductive than the CS grouted zone. A thorough investigation of groundwater pressure across the whole tunnel boundary should be done to assess connectivity in the EDZ.

12.5 Stress-induced aperture and joint pressure changes in the EDZ

The results from the numerical simulations showed that, generally, the apertures opened where stress relief occurred and closed where stress concentration occurred. This means that the apertures in the wall and lateral distance opened relative to the apertures in the roof, where they closed. An exception is the sub-horizontal joint set that closed in the walls and opened up in the roof and the invert, and the middle part of the invert. Considering that the tangential stresses will act parallel to the horizontal

joint set in the roof and the invert, it is found that the horizontal joint set is exposed to tensile forces in these areas. The results align well with the reports by Tsang et al. (2005); according to Tsang et al., bedding planes are typically opened in the roof and the invert in the EDZ. There is also stress relief in the middle of the invert, where the joints also open, but laterally, they close.

The results also show that stress directions are not the only factor that decides which joints open or close. The joint orientation also decides how the stress distribution affects the joint apertures. Therefore, individual joint orientations must be evaluated when considering aperture changes in the EDZ. The joint pressure distribution coincides with the distribution of stress. It shows that pressure is reduced laterally from the walls, where the compressional stress is lower, and is higher in the crown, where stress concentration occurs. These findings align with Read and Chandler (1999), who found that less pressure is associated where stress relief occurs and higher in regions of high compressive stress.

12.6 Numerical simulations versus in-situ measurements in the EDZ

As previously discussed, the findings in section 10 suggest that the joints in the EDZ are open and have large transmissivities (Hestnes project). This hypothesis shows good agreement with the 3DEC simulations, which indicates that several joint planes are opened beyond what was measured in situ. The initial aperture was set at 55 μm , based on the values from WPT. When the coupled solution is run, these joints can close or open. The results show that most joints open slightly but are still within the 75 percentile of the estimated joint apertures seen in table 10.2. This indicates that chosen values for rock's mechanical properties, in-situ stress, and initial apertures in the numerical model are reasonable.

12.7 Evaluation of the findings concerning the tunnel concept

The RS2 and 3DEC analysis results show that the grouting procedure, with SC and MC in the wall and crown, and only MC in the invert, diverts the flow paths towards the invert and significantly less water flow through the SC grouted zone. The results also show that groundwater pressures are reduced in the grouted zone. The results in 3DEC represent a more realistic situation: water flows on rock joints and not through the matrix with a constant hydraulic conductivity. Since the results are similar, it gives more credibility to the grouting concept. The predicted tightness (hydraulic apertures and hydraulic conductivity) is based on research from other projects. Therefore, the achieved tightness at the Hestnes project still needs to be measured to verify the numerical results and perform new simulations with the updated data.

The 3DEC analysis included stress-induced aperture changes only. Scenarios 2 and 3 in the results show a significant increase in the flow in the open apertures compared to those that close. The analysis in RS2 shows that the shotcrete has low enough hydraulic conductivity to divert flow toward the invert. The flow directions in the 3DEC model also show that water generally flows towards the invert, but in this case, the shotcrete is completely impermeable. However, the findings from the FEM analysis suggest that shotcrete will be close to impermeable. The findings from WPT and joint transmissivities in the EDZ for Gevingåsen and Drammen show that the frequency of high transmissive joints is higher close to the tunnel boundary (Figure 10.2). WPT from the Hestnes tunnel did not indicate this, but as previously discussed, the lack of measurements in Hestnes is likely due to open and conductive rock joints.

Scenario 3 in the 3DEC model shows that the joint transmissivity is not continuous across the tunnel boundary because joints open and close depending on the stress distribution. If the 3DEC model included blasting-induced joint transmissivities, there is likely to be more connectivity between the crown and the invert. The 3DEC model needs to be updated with WPT data close to the tunnel excavation so that the influence of blasting-induced damage can be verified and put into the model. Other studies suggest a significant increase of joint transmissivities in the EDZ due to blasting damage (Aas 2020; Ericsson et al. 2015; Martino and Chandler 2004). Similar simulations in 3DEC that included an estimation of blasting-induced EDZ showed that joint pressure reduction occurs more uniformly behind the shotcrete lining, depending on the stress distribution, indicating a connective EDZ (Nilsen 2019). Still, as already discussed, there are uncertainties regarding the connectivity in the EDZ.

The numerical simulations show that the horizontal stresses generally cause more joints to open in the wall, except the horizontal joint set that open in the crown and invert. Accordingly, there might be connectivity between the conductive joint sets around the tunnel boundary since the results show that conductive joints are associated with open joints. Since the horizontal joint set has a dip between 0-30°, it can transport water towards the invert. Site observations also confirmed that the horizontal joint set was injected by grout, indicating that the joint set is conducting.

12.8 Verification of conceptual model

A comparison of the concept and the results of the numerical models can be seen in figure 12.1. The results of this study agree with several principles of the tunnel concept. The numerical results show that the zone grouted with CS will significantly reduce inflow toward the walls and the crown. Water flow increases in the invert because of the contrast in hydraulic conductivity in the two grouted zones. The groundwater pressures are lowered in the grouted zone, likely because of the combined effect of the EDZ and the grouted zone. This fits well with the concept model, that groundwater is drained towards the invert in the EDZ, and that groundwater pressure acting on the shotcrete is reduced. Estimations from WPT in Drammen and Gevingåsen indicate a significant increase in joint transmissivity in the EDZ compared to in-situ transmissivity.

The numerical models do not include both stress-induced and blasting-induced damage. Still, both RS2 and 3DEC models show increased drainage outside the shotcrete. Most likely are the results conservative concerning transmissivity in the EDZ. The RS2 model confirms that shotcrete is close to impermeable if we assume that the shotcrete is intact and without cracks, which might be too optimistic (Holter et al. 2023). The study lacks in-situ measurements in the grouted zone to confirm the hydraulic conductivities in the CS and MC grouted zone. Also, flow connectivity from the crown to the invert is not investigated in this study. Interaction between joint flow and shotcrete is also not addressed properly in 3DEC.

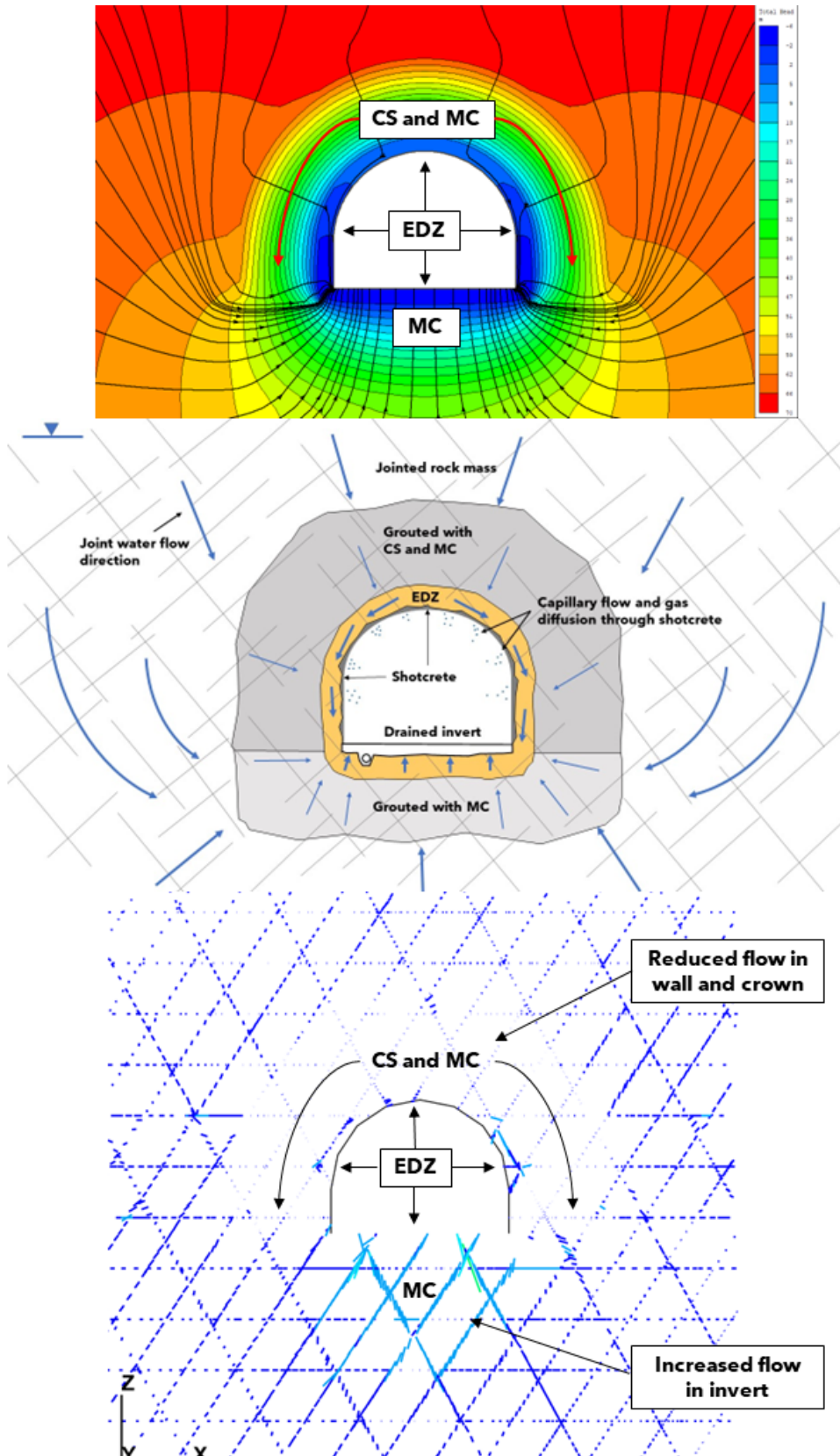


Figure 12.1: A comparison of the tunnel concept and the numerical results in RS2 and 3DEC. Both numerical models verify that flow is altered towards the invert and flow is reduced in the crown and wall, which is grouted with CS. Increased drainage in the EDZ is also seen.

13 Limitations

The author would like to highlight the following limitations:

- The 3DEC model needs to be large to be scale appropriate. At the same time, the resolutions need to be high close to the excavation. It was necessary to compromise to have the desired detail close to the excavation boundary while having a model with an acceptable solving time. Calculations times were over three weeks for certain scenarios.
- It was challenging to represent permeable shotcrete in the 3DEC model since the rock reinforcement does not participate in the fluid flow calculations.
- The hydraulic conductivity of the grouted rock mass is based on literature and not in-situ measurements, which unfortunately could not be conducted in time. Therefore there are uncertainties regarding the tightness predicted in the numerical simulations.
- Conducted WPT in the Hestnes project gave few valid measurements close to the tunnel boundary, and it was hard to quantify the transmissivities in the EDZ because of this.
- The 3DEC model only considers stress-induced aperture changes because WPT results had few measurements in the most critical area of the EDZ close to the tunnel excavation. There is expected to be a significant contribution from blasting damage in the form of re-activation of healed joints, forming of microcracks, or opening of existing joints. The joint pressures close to the tunnel excavation might be overestimated.
- Very long solving times in 3DEC prevented experimenting with different scenarios and implementing features such as permeable shotcrete.
- The models were run to equilibrium by monitoring a set number of points and their pressure history. Equilibrium is reached when pressure changes flatten out and reach a steady state. There might be some areas where the joint pressures are not steady state because of very low flow rates. This is, however, not expected to affect any of the broader conclusions reached in this study.

14 Conclusions

This thesis investigated the hydraulic properties of the excavation damage zone. The investigations include joint transmissivity estimations based on WPT data from Gevingåsen, Drammen, and Hestnes railroad tunnel. Numerical simulations were done on the main case study, the Hestnes tunnel, in 3DEC and RS2. The scenarios included a new tunneling concept, a partially drained and functionally dry tunnel, achieved by a differentiated grouting procedure so that traditional water- and frost protection measures can be neglected. This is done using CS, a low-viscous grout material that can penetrate finer apertures than traditional grout materials like MC. The main findings of this study are summarized below.

The following conclusions can be made on investigations of the EDZ from WPT:

- Estimations of joint transmissivities from WPT in Drammen and Gevingåsen tunnels show a higher frequency of high transmissivity joints close to the excavation, approximately the first 0.5 m.
- Estimated joint transmissivities in Hestnes show no conclusive difference in joint transmissivity in the EDZ compared to in-situ rock. There was a lack of valid measurements in the first 0.5 m of the boreholes. Leakage out of nearby holes and in the shotcrete indicates that the joints are open and conductive. Core material and boreholes had visible signs of blasting-induced damage.
- Estimations of hydraulic apertures in the Hestnes project indicate that most of the finer apertures can only be grouted by colloidal silica.

The main findings from the numerical simulations are as follows:

- Results from numerical simulations show a significant increase in joint apertures due to excavation-induced stress.
- Large horizontal stress compared to vertical generally causes the joint to open in the wall while closing in the invert and crown. The aperture changes vary and are not uniform. Joint orientations also influence which joints open and close. The results show that horizontal joints tend to open in the invert and the crown, and other joints close in the corners of the invert and the crown.
- Joint pressure distribution around the excavation is anisotropic, and less pressure is associated with the joints that open.
- The numerical simulations in both 2D and 3D show significantly less water flow through the zone grouted with both MC and SC. Flow is instead diverted towards the invert. Joint pressures are reduced in the grouted zone and the EDZ.

- Results from the FEM analysis indicate that the shotcrete has a significant water-shielding effect.

Conclusions concerning verification of the concept model:

- The numerical simulations show that the CS grouted zone reduced water flow significantly. Water flow is diverted through the invert because of the differentiated grouting procedure. The RS2 analysis shows that intact shotcrete without cracks is close to impermeable. Numerical simulations show that stress-induced damage can increase the water-draining effect outside the shotcrete and that joint pressures are generally reduced in the grouted zone and the EDZ.
- WPT shows that joint transmissivity increases in the EDZ due to blasting, which can increase the draining effect in the EDZ.
- The study fails to address flow connectivity in the EDZ and the influence of blasting damage in the numerical simulations. Achieved tightness by the differentiated grouting procedure is not verified.

15 Recommendations for future work

The following suggestions are recommended for future work at the Hestnes tunnel

- Another round of in-situ stress measurements to verify σ_H .
- A new round of WPT in ungrouted rock to have more valid measurements of transmissivities in the EDZ.
- WPT of the grouted zone to verify hydraulic conductivity in the grouted zone, both the foot and the wall, to see the difference between achieved tightness in CS and MC grouted areas. These investigations should also aim to verify the transmissivity of the EDZ and the transition to the grouted rock.
- Further work should investigate flow connectivity around the whole excavation boundary.

The following suggestions are made for future work in numerical simulations:

- A more sophisticated joint model with a DFN in different zones of the EDZ to have more realistic jointing and flow.
- A larger FEM model in 3D that incorporates groundwater drawdown, grouted zone, shotcrete permeability, and excavation damage. A larger model in 3DEC is perhaps unrealistic, taking the calculation time into perspective.
- Finding a proper way to introduce blasting-induced damage into the numerical simulations that capture; forming of microcracks, re-activation of healed joints, and opening of existing joints.
- Having a geological model with both gneiss and amphibolite so that the influence of a more complex geology is included.

References

- Aas, N. F. (2020). "Feltmålinger av hydrauliske egenskaper rundt sprengte tunneler". MA thesis. NTNU.
- Adamic, L. A. (2000). "Zipf, power-laws, and pareto-a ranking tutorial". In: *Xerox Palo Alto Research Center, Palo Alto, CA*, <http://ginger.hpl.hp.com/shl/papers/ranking/ranking.html>.
- Alejano, L. R., Muralha, J., Ulusay, R., Li, C. C., Pérez-Rey, I., Karakul, H., Chryssanthakis, P., and Aydan, Ö. (2018). "ISRM suggested method for determining the basic friction angle of planar rock surfaces by means of tilt tests". In: *Rock Mechanics and Rock Engineering* 51, pp. 3853–3859.
- Alvarez, T. A., Cording, E. J., and Mikhail, R. A. (1995). "Hydromechanical behavior of rock joints: A re-interpretation of published experiments". In: *The 35th US Symposium on Rock Mechanics (USRMS)*. OnePetro.
- Axelsson, M., Gustafson, G., and Fransson, Å. (2009). "Stop mechanism for cementitious grouts at different water-to-cement ratios". In: *Tunnelling and Underground Space Technology* 24.4, pp. 390–397. ISSN: 0886-7798. DOI: <https://doi.org/10.1016/j.tust.2008.11.001>. URL: <https://www.sciencedirect.com/science/article/pii/S0886779808001120>.
- Aydin, A. (2015). "ISRM suggested method for determination of the Schmidt hammer rebound hardness: revised version". In: *The ISRM Suggested Methods for Rock Characterization, Testing and Monitoring: 2007-2014*, pp. 25–33.
- Aydin, A. and Basu, A. (2005). "The Schmidt hammer in rock material characterization". In: *Engineering Geology* 81.1, pp. 1–14.
- Bäckblom, G. (2008). *Excavation damage and disturbance in crystalline rock-Results from experiments and analyses*. Tech. rep. SKB-TR-08-08. Swedish Nuclear Fuel and Waste Management Co., Stockholm (Sweden).
- Badika, M., El Merabi, B., Capdevielle, S., Dufour, F., and Saletti D. and Briffaut, M. (2022). "Influence of Concrete–Rock Bonds and Roughness on the Shear Behavior of Concrete–Rock Interfaces under Low Normal Loading, Experimental and Numerical Analysis". In: *Applied Sciences* 12.11, p. 5643.
- Bandis, S. C., Lumsden, A. C., and Barton, N. R. (1983). "Fundamentals of rock joint deformation". In: *International Journal of Rock Mechanics and Mining Sciences & Geomechanics Abstracts*. Vol. 20. 6. Elsevier, pp. 249–268.

- BaneNOR (2022). *Bane NOR; Tunneler/Prosjektering og bygging/Portaler og vannsikring, teknisk regelverk 9(4)*.
- BaneNOR (2019). *KS-1 Hestnestunnelen*. URL: <https://www.banenor.no/Prosjekter/prosjekter/kleverud-sorli/innhold/20192/hestnestunnelen/> (visited on 02/23/2023).
- Barton, N. R (1973). "Review of a new shear-strength criterion for rock joints". In: *Engineering geology* 7.4, pp. 287–332.
- Barton, N. R (1982). *Modelling rock joint behavior from in situ block tests: implications for nuclear waste repository design*. Vol. 308. Office of Nuclear Waste Isolation, Battelle Project Management Division.
- Barton, N. R. and Choubey, V. (1977). "The shear strength of rock joints in theory and practice". In: *Rock mechanics* 10, pp. 1–54.
- Barton, N. R., Lien, R., and Lunde, J. (1974). "Engineering classification of rock masses for the design of tunnel support". In: *Rock mechanics* 6, pp. 189–236.
- Barton, N. R. and Lindstrøm, M. (2003). *Teoretisk og empirisk forståelse av forinjeksjon og mulighet for redusert sikringsmengde i utvalgte tunnelstrekninger*. Vegdirektoratet.
- Barton, N. R. and Roald, S. (2023). "Pre-Grouting for Tunnels in Jointed Rock". In: *Current Trends in Civil & Structural Engineering*. ISSN: 2643-6876.
- Barton, N. R. (1972). "A model study of rock-joint deformation". In: *International Journal of Rock Mechanics and Mining Sciences & Geomechanics Abstracts*. Vol. 9. 5. Elsevier, pp. 579–582.
- Barton, N. R. (2013). "Shear strength criteria for rock, rock joints, rockfill and rock masses: Problems and some solutions". In: *Journal of Rock Mechanics and Geotechnical Engineering* 5.4, pp. 249–261.
- Bieniawski, Z. T. and Bernede, M. J. (1979). "Suggested methods for determining the uniaxial compressive strength and deformability of rock materials". In: *International journal of rock mechanics and mining sciences & geomechanics abstracts*. Vol. 16. 2. Elsevier, pp. 138–140.
- Boden, A. and Sievaenen, U. (2005). *Low-pH injection grout for deep repositories. Summary report from a co-operation project between NUMO (Japan), Posiva (Finland) and SKB (Sweden)*. Tech. rep. Swedish Nuclear Fuel and Waste Management Co.

- Bryne, L. E., Ansell, A., and Holmgren, J. (2014). "Laboratory testing of early age bond strength of shotcrete on hard rock". In: *Tunnelling and Underground Space Technology* 41, pp. 113–119.
- Cundall, P. A. (1988). "Formulation of a three-dimensional distinct element model—Part I. A scheme to detect and represent contacts in a system composed of many polyhedral blocks". In: *International journal of rock mechanics and mining sciences & geomechanics abstracts*. Vol. 25. 3. Elsevier, pp. 107–116.
- Darcy, H. (1856). *Les fontaines publiques de la ville de Dijon: exposition et application des principes à suivre et des formules à employer dans les questions de distribution d'eau... un appendice relatif aux fournitures d'eau de plusieurs villes au filtrage des eaux*. Vol. 1. Victor Dalmont, éditeur.
- Dywidag (2012). *Mechanical Anchors and Rebar Rock Bolts*. Tech. rep. URL: http://www.dywidag-norge.no/wp-content/uploads/2013/09/DSI-ALWAG-Systems_Mechanical-Anchors-and-Rebar-Rock-Bolts.pdf (visited on 03/13/2023).
- El Tani, M. (2003). "Circular tunnel in a semi-infinite aquifer". In: *Tunnelling and underground space technology* 18.1, pp. 49–55.
- El Tani, M. (1999). "Water inflow into tunnels". In: *Proceedings of the World Tunnel Congress ITA-AITES*. Oslo, Norway: Balkema, pp. 61–70.
- Ericsson, L. O., Thörn, J., Christiansson, R., Lehtimäki, T., Ittner, H., Hansson, K., Butron, C., Sigurdsson, O., and Kinnbom, P. (2015). *A demonstration project on controlling and verifying the excavation-damaged zone. Experience from the Äspö Hard Rock Laboratory*. Tech. rep. SKB R-14–30.
- Fransson, Å. (2002). "Nonparametric method for transmissivity distributions along boreholes". In: *Groundwater* 40.2, pp. 201–204.
- Funehag, J. (2008). *Injection sealing of the TASS tunnel. Progress report; Injekteringen av TASS-tunneln. Delresultat tom september 2008*.
- Gustafson, G. and Fransson, Å. (2006). "The use of the Pareto distribution for fracture transmissivity assessment". In: *Hydrogeology Journal* 14, pp. 15–20.
- Gustafson, G. and Walke, L. (2012). *Hydrogeology for rock engineers*. BeFo Stockholm.
- Hoek, E. (2000). "Practical rock engineering". In: *Internet reference: www.rocscience.com*.
- Hognestad, H. O., Fagermo, J. I., Kveen, A., Backer, L., Grøv, E., Frogner, E., and Aarset, A. (2010). "Praktisk berginjeksjon for underjordsanlegg". In: *NFF håndbok*.6.

- Holmberg, M., Tsuji, M., Stille, B., and Stille, H. (May 2012). "Evaluation of Pre-grouting For the City Line Project Using the RTGC Method". In: ISRM EUROCK. eprint: <https://onepetro.org/ISRMEUROCK/proceedings-pdf/EUROCK12/A11-EUROCK12/ISRM-EUROCK-2012-123/1642863/isrm-eurock-2012-123.pdf>.
- Holter, K., Buvik, H., Neramoen, B., and Nilsen, B. (2013). "Future trends for tunnel lining design for modern rail and road tunnels in hard rock and cold climate". In: *Proceedings of the world tunnel congress, Geneva*.
- Holter, K. G. (2015). "Properties of waterproof sprayed concrete tunnel linings". PhD thesis. Norwegian University of Science and Technology, Trondheim, p. 197.
- Holter, K. G. and Geving, S. (2016). "Moisture transport through sprayed concrete tunnel linings". In: *Rock Mechanics and Rock Engineering* 49, pp. 243–272.
- Holter, K. G., Hammer, T., Trussell, N. H., and Strømsvik, H. (2023). "New development of sprayed concrete with improved waterproofing, durability and sustainability performance". In: *Expanding Underground-Knowledge and Passion to Make a Positive Impact on the World*. CRC Press, pp. 2422–2430.
- Holter, K. G. and Strømsvik, H. (2023). *Notat Hestnestunnelen: Teknisk beskrivelse av forinjeksjon; prosedyrer og injeksjonsmasse*. Tech. rep. SINTEF-NGI [23-04-18].
- Hölttä, P. L., Hakanen, M., Lahtinen, M., Leskinen, A., Lehto, J., and Juhola, P. (2008). "Release of colloids from injection grout silica sol". In: *MRS Online Proceedings Library (OPL)* 1124.
- Itasca (2019). *3DEC 7.0 documentation*. URL: <https://docs.itascacg.com/3dec700/3dec/docproject/source/3dechome.html?node1961> (visited on 06/06/2023).
- Karaman, K. and Kesimal, A. (2015). "A comparative study of Schmidt hammer test methods for estimating the uniaxial compressive strength of rocks". In: *Bulletin of Engineering Geology and the Environment* 74, pp. 507–520.
- Karlsrud, K., Erikstad, L., and Snilsberg, P. (2014). "Undersøkelser og krav til innlekkasje for å ivareta ytre miljø". In: Vegdirektoratet Report publ.103, pp. 1–103. ISSN: 0803-6950.
- Krokedal, S. (2022). "Forinjeksjon med strenge krav til tetthet". MA thesis. NTNU.
- Kulatilake, P. H., Shreedharan, S., Sherizadeh, T., Shu, B., Xing, Y., and He, P. (2016). "Laboratory estimation of rock joint stiffness and frictional parameters". In: *Geotechnical and Geological Engineering* 34, pp. 1723–1735.

- Labuz, J. F. and Zang, A. (2012). "Mohr–Coulomb failure criterion". In: *Rock mechanics and rock engineering* 45, pp. 975–979.
- Lei, S. (1999). "An analytical solution for steady flow into a Tunnel". In: *Groundwater* 37.1, pp. 23–26.
- Li, C., Zhang, N., and Ruiz, J. (2019). "Measurement of the basic friction angle of planar rock discontinuities with three rock cores". In: *Bulletin of Engineering Geology and the Environment* 78, pp. 847–856.
- Martino, J. B. and Chandler, N. A. (2004). "Excavation-induced damage studies at the underground research laboratory". In: *International Journal of Rock Mechanics and Mining Sciences* 41.8, pp. 1413–1426.
- Mellanen, S., Hellae, P., and Loeffman, J. (2009). *EDZ programme, EDZ studies in ONKALO 2007-2008*. Tech. rep. Posiva Oy.
- Mitchell, J. K. (1982). "Soil improvement state of the art." In: *10th International Conference on Soil Mechanics and Foundation Engineering*. 4. Stockholm, Sweden.
- Myrvang, A. (2001). *Kompendium bergmekanikk*.
- NGI (2022). *Bruk av Q-systemet-Håndbok*.
- NGU (2022). *1:250 000 Berggrunskart, Norges geologiske undersøkelse*. Hentet 24.04.2023. URL: https://geo.ngu.no/kart/berggrunn_mobil/.
- Nilsen, E. (2019). "Groundwater Pressure on a Partially Drained Tunnel Lining". MA thesis. NTNU.
- NRA (2014). *Håndbok R761: Prosesskode 1 Standard beskrivelse for vegkontrakter*. Norwegian road authority, Oslo.
- NRA (2012). *Etatsprogrammet Moderne vegtunneler - Strategi for bygging av nye vegtunneler - Grunnlagsdokument*. Norwegian road authority, Oslo.
- NRA (2022). *Road standard N500; Road tunnels*. Norwegian road authority, Oslo.
- Olsson, M., Niklasson, B., Wilson, L., Andersson, C., and Christiansson, R. (2004). *Äspö HRL. Experiences of blasting of the TASQ tunnel*. Tech. rep. Swedish Nuclear Fuel and Waste Management Co.
- Palmström, A. and Singh, R. (2001). "The deformation modulus of rock masses—comparisons between in situ tests and indirect estimates". In: *Tunnelling and Underground Space Technology* 16.2, pp. 115–131.

- Ramberg, I.B., Bryhni, I., Nøttvedt, A., and K., Rangnes. (2013). *Landet blir til. Norges geologi*. Vol. 2. Norsk Geologisk Forening, p. 656. ISBN: 978-82-92-39483-0.
- Read, R. S. and Chandler, N. A. (1999). "Excavation damage and stability studies at the URL Rock mechanics considerations for nuclear fuel waste disposal in Canada". In: *Vail Rocks 1999, The 37th US Symposium on Rock Mechanics (USRMS)*. OnePetro.
- Reddy, J. N. (2019). *Introduction to the finite element method*. McGraw-Hill Education.
- Resset, R. I. (2023). *Mer miljøvennlig tunnelbygging*. URL: <https://www.banenor.no/prosjekter/alle-prosjekter/dobbeltspor-gjennom-stange-kommune/2023/tett-tunnel/> (visited on 05/26/2017).
- Rockscience (2021). *Rockscience inc*. URL: <https://www.rockscience.com/software/rs2> (visited on 05/28/2023).
- Sika (2021). *MS-D1*. Tech. rep. URL: https://can.sika.com/content/dam/dms/ca01/7/MS-D1_rev.0011_pds-en.pdf (visited on 03/13/2023).
- SINTEF (Apr. 2023). *Måling av vannsprekkekonduktiviteten for Bane Nor Hestnestunnelen*. Tech. rep.
- Siren, T., Kantia, P., and Rinne, M. (2015). "Considerations and observations of stress-induced and construction-induced excavation damage zone in crystalline rock". In: *International Journal of Rock Mechanics and Mining Sciences* 73, pp. 165–174.
- Slagstad, T. et al. (2020). "The Sveconorwegian orogeny – Reamalgamation of the fragmented southwestern margin of Fennoscandia". In: *Precambrian Research* 350, p. 105877. ISSN: 0301-9268. DOI: <https://doi.org/10.1016/j.precamres.2020.105877>.
- Snow, D. T. (1969). "Anisotropic permeability of fractured media". In: *Water resources research* 5.6, pp. 1273–1289.
- Souley, M., Homand, F., Pepa, S., and Hoxha, D. (2001). "Damage-induced permeability changes in granite: a case example at the URL in Canada". In: *International Journal of Rock Mechanics and Mining Sciences* 38.2, pp. 297–310.
- Tsang, C., Bernier, F., and Davies, C. (2005). "Geohydromechanical processes in the Excavation Damaged Zone in crystalline rock, rock salt, and indurated and plastic clays—in the context of radioactive waste disposal". In: *International Journal of Rock Mechanics and Mining Sciences* 42.1, pp. 109–125.

- Tveit, M. (2018). "Undersøkelser av sprengningsskadesonen for vurdering av hydraulisk konduktivitet i bergmassen rundt sprengte tunneler". MA thesis. NTNU.
- Wang, X. and Cai, M. (2020). "A DFN–DEM multi-scale modeling approach for simulating tunnel excavation response in jointed rock masses". In: *Rock Mechanics and Rock Engineering* 53, pp. 1053–1077.
- Witherspoon, P. A., Wang, J., Iwai, K., and Gale, J. E. (1980). "Validity of cubic law for fluid flow in a deformable rock fracture". In: *Water resources research* 16.6, pp. 1016–1024.
- Yasir, B., Rougelot, T, and Burlion, N. (2018). "Instant and delayed mechanical behaviour of sprayed concrete used on andra's url: towards an understanding of the links between formulation, implentation and in situ properties". In: *8th international symposium on sprayed concrete modern use of wet mix sprayed concrete for underground support*.
- Zimmerman, R. W. and Bodvarsson, G. S. (1996). "Hydraulic conductivity of rock fractures". In: *Transport in porous media* 23.1, pp. 1–30.

A IN-SITU STRESS MEASUREMENTS BY PÖYRY



OVERCORING ROCK STRESS MEASUREMENTS WITH BORRE III

Project Site: Uvintunnein, Eidsvoll kommun
 Borehole: K82398E och K82398E2
 Measurement: 1:1:3, 1:2:6, 1:3:7, 1:4:21
 Date: 2012-02-27 till 2012-02-27

Input data

Length [mbl]	Borehole dip [°]	Borehole bearing [°]	Ball [°]	Needle [°]	Young's modulus [GPa]	Poisson's ratio	Logging time	
							[hh:mm:ss]	[hh:mm:ss]
28.61	1	99	270	-	57.9	0.19	Start=10:00:00	Stop=00:33:51
31.59	1	99	228	-	57.9	0.19	Start=09:45:00	Stop=00:30:39
32.52	1	99	150	-	57.9	0.19	Start=10:15:00	Stop=00:48:00
32.63	-5	99	175	-	57.9	0.19	Start=08:00:00	Stop=23:20:57

Strains

Length [mbl]	$\epsilon_{r,1}$ [ustrain]	$\epsilon_{r,1}$ [ustrain]	$\epsilon_{45,1}$ [ustrain]	$\epsilon_{r,2}$ [ustrain]	$\epsilon_{r,2}$ [ustrain]	$\epsilon_{45,2}$ [ustrain]	$\epsilon_{r,3}$ [ustrain]	$\epsilon_{r,3}$ [ustrain]	$\epsilon_{45,3}$ [ustrain]
28.61	-	-	-	44	-15	-42	-	-	-
31.59	26	107	111	58	270	-4	64	-2	85
32.52	113	87	56	91	166	40	111	207	290
32.63	58	-59	32	-121	168	19	68	77	147

Medel all gauges except 270 at 31.59 and 166 at 32.52

Calculated principal stresses

Length [mbl]	σ_1 [MPa]	σ_1 -bearing [°]	σ_1 -dip [°]	σ_2 [MPa]	σ_2 -bearing [°]	σ_2 -dip [°]	σ_3 [MPa]	σ_3 -bearing [°]	σ_3 -dip [°]
28.61	-	-	-	-	-	-	-	-	-
31.59	8.5	153	11	2.3	54	38	0.5	256	50
32.52	10.6	315	9	4.2	95	79	3.6	224	7
32.63	6.9	321	16	1.9	53	6	0.3	162	73
Medel	7.1	319	2	2.7	49	22	1.5	225	68

Calculated horizontal/vertical stresses

Length [mbl]	σ_H [MPa]	σ_H -bearing [°]	σ_h [MPa]	σ_h -bearing [°]	σ_v [MPa]	σ_v -theory [MPa]
28.61	-	-	-	-	-	-
31.59	8.2	154	1.6	-	244	1.5
32.52	10.5	135	3.6	-	225	4.4
32.63	6.5	141	1.9	-	231	0.8
Medel	7.1	138	2.6	-	228	1.7

B FIELD MAPPING RESULTS

JRC measurements

Table B.1: Table of all JRC values from field investigations.

Gneiss		Amphibolite	
Strike/dip	JRC	Strike/dip	JRC
177/70W	10	030/54NW	3
178/69W	7	030/15SW	4
013/71W	7	060/85SE	6
165/88W	8	030/10SW	4
090/56N	8	090/28N	5
096/32N	5	180/70e	6
170/67E	3	150/80W	4
165/73E	4	050/64SE	7
030/78SE	2	056/60SE	6
168/80E	1		
160/56NE	5		
155/60NE	4		
140/81NE	5		

DRILLCORE LOG		Date drilled	28.02.2022
SITE:	Gevingslammullen	Core material logged by	22.03.2023
LOCATION:	Gevingsåsen	Coordinates	Fredrik Rian
HOLE NUMBER:	BH5	Hole inclination	-5
HOLE SECTION (from-to, m)	0-3.0	Hole direction	N100

Joint types	Explanation	Equation variables		
Rock joint	Natural occurring joint	L =	15,000	cm
Blasting induced	Rock joint sets	L _w =	3,100	cm
Extraction	From blasting	Hydrostatic pressure =	96,000	kpa
	Core damage related to extraction			

Bore hole section [m]	DESCRIPTION OF CORE	ROCK TYPE/PHOTO	ROD	ROCK JOINT DATA					WATER PRESSURE TESTING			Estimations				
				NUMBER OF JOINTS / m	JOINT SPACING [m]	Joint type	JRC	COATING FILLING	Comments	SECTION MEASURED [m]	WATER FLOW RATE STATIONARY [l/min]	PUMPING PRESSURE [kPa]	Pumping Head [m]	Moye's equation TRANSMISSIVITY [m ² /s]	Cubic law Joint hydr aperture [mm]	Gustafson's equation Joint transmissivity [m ² /s]
0.00				4	0.09	rock joint	20		not fractured	0.27	0.024	607	53.1	2.34652E-09	0.030	1.96424E-09
0.03										0.42	0.088	918	82.2	5.34867E-09	0.040	4.47728E-09
0.06										0.57	0.296	1209	111.3	1.32871E-08	0.054	1.11234E-08
0.09																
0.12																
0.15																
0.18																
0.21																
0.24																
0.27																
0.30				10	0.02	rock joint	17	phyllite	fresh, intersected by discontinuous joint	0.71	0.014	311	21.5	3.2533E-09	0.034	2.72329E-09
0.33										0.86	0.040	626	53	3.77067E-09	0.036	3.15637E-09
0.36										0.9	0.106	930	83.4	6.35001E-09	0.042	5.31549E-09
0.39											0.289	1214	111.8	1.29149E-08	0.054	1.08108E-08
0.42																
0.45																
0.48																
0.51																
0.54																
0.57																
0.60																
0.63																
0.66																
0.69																
0.72																
0.75																
0.78																
0.81																
0.84																
0.87																
0.90																
0.93																
0.96																
0.99																
1.02																
1.05																
1.08																
1.11																
1.14																
1.17																
1.20																
1.23																
1.26																
1.29																
1.32																
1.35																
1.38																
1.41																
1.44																
1.47																
1.50																
1.53																
1.56																
1.59																
1.62																
1.65																
1.68																
1.71																
1.74																
1.77																
1.80																
1.83																
1.86																
1.89																
1.92																
1.95																
1.98																
2.01																
2.04																
2.07																
2.10																
2.13																
2.16																
2.19																
2.22																
2.25																
2.28																
2.31																
2.34																
2.37																
2.40																
2.43																
2.46																
2.49																
2.52																
2.55																
2.58																
2.61																
2.64																
2.67																
2.70																
2.73																
2.76																
2.79																
2.82																
2.85																
2.88																
2.91																
2.94																
2.97																
3.00																
3.03																
3.06																
3.09																
3.12																
3.15																
3.18																
3.21																
3.24																

D CORE LOGGING DRAMMEN

DRILLCORE LOG			Date drilled	24/07/2022
			Core material logged	19/07/2022
			Core material logged by	Freddie Ross
			Coordinates	
			Hole inclination	-5.00
			Hole direction	N148
HOLE SECTION (from-to, m)			0.2	

BORE HOLE IMAGE PHOTO		ROCK TYPE	ROD	NUMBER OF JOINTS (n)	JOINT SPACING (m)	Joint type	JRC	COATING FILLING	Comments	SECTION MEASURED	WATER FLOW RATE STATIONARY (l/min)	HYDRAULIC PRESSURE (kPa)	Pumping head (m)	Moseley's equation Section transmissibility (l ² /s)	Cubic law Joint hyd aperture (mm)	Coatsworth's equation Section transmissibility (l ² /s)	Cubic law Joint hyd aperture (mm)
0.00			48	8	0.04-0.06	0.00			Fresh fracture. Clear blasting induced fracture	0.15	0.317	325	31	4.55676-08	0.082	3.72437E-08	0.076
0.06						0.05			Fresh fracture								
0.09						0.04			Fresh fracture								
0.12																	
0.15																	
0.18																	
0.21																	
0.24																	
0.27																	
0.30																	
0.33																	
0.36																	
0.39																	
0.42																	
0.45																	
0.48																	
0.51																	
0.54																	
0.57																	
0.60																	
0.63																	
0.66																	
0.69																	
0.72																	
0.75																	
0.78																	
0.81																	
0.84																	
0.87																	
0.90																	
0.93																	
0.96																	
0.99																	
1.02																	
1.05																	
1.08																	
1.11																	
1.14																	
1.17																	
1.20																	
1.23																	
1.26																	
1.29																	
1.32																	
1.35																	
1.38																	
1.41																	
1.44																	
1.47																	
1.50																	
1.53																	
1.56																	
1.59																	
1.62																	
1.65																	
1.68																	
1.71																	
1.74																	
1.77																	
1.80																	
1.83																	
1.86																	
1.89																	
1.92																	
1.95																	
1.98																	
2.01																	
2.04																	
2.07																	
2.10																	
2.13																	
2.16																	
2.19																	
2.22																	
2.25																	
2.28																	
2.31																	
2.34																	
2.37																	
2.40																	
2.43																	
2.46																	
2.49																	
2.52																	
2.55																	
2.58																	
2.61																	
2.64																	
2.67																	
2.70																	
2.73																	
2.76																	
2.79																	
2.82																	
2.85																	
2.88																	
2.91																	
2.94																	
2.97																	
3.00																	
3.03																	
3.06																	
1.50																	
1.53																	
1.56																	
1.59																	
1.62																	
1.65																	
1.68																	
1.71																	
1.74																	
1.77																	
1.80																	
1.83																	
1.86																	
1.89																	
1.92																	
1.95																	
1.98																	
2.01																	
2.04																	
2.07																	
2.10																	
2.13																	
2.16																	
2.19																	
2.22																	
2.25																	
2.28																	
2.31																	
2.34																	
2.37																	
2.40																	
2.43																	
2.46																	
2.49																	
2.52																	
2.55																	
2.58																	
2.61																	
2.64																	
2.67																	
2.70																	
2.73																	
2.76																	
2.79																	
2.82																	
2.85																	
2.88																	
2.91																	
2.94																	
2.97																	
3.00																	
3.03																	
3.06																	
1.50																	
1.53																	
1.56																	
1.59																	
1.62																	
1.65																	
1.68																	
1.71																	
1.74																	
1.77																	
1.80																	
1.83																	
1.86																	
1.89																	
1.92																	
1.95																	
1.98																	
2.01																	
2.04																	
2.07																	
2.10																	
2.13																	
2.16																	
2.19																	
2.22																	
2.25																	
2.28																	
2.31																	
2.34																	
2.37																	
2.40																	
2.43																	
2.46																	
2.49																	
2.52																	
2.55																	
2.58																	
2.61																	
2.64																	
2.67																	
2.70																	
2.73																	
2.76																	
2.79																	
2.82																	
2.85																	
2.88																	
2.91																	
2.94																	
2.97																	
3.00																	
3.03																	
3.06																	
1.50																	
1.53																	
1.56																	
1.59																	
1.62																	
1.65																	
1.68																	
1.71																	
1.74																	
1.77																	
1.80																	
1.83																	
1.86																	
1.89																	
1.92																	
1.95																	
1.98																	
2.01																	
2.04																	
2.07																	
2.10																	
2.13																	
2.16																	
2.19																	
2.22																	
2.25																	
2.28																	
2.31																	
2.34																	
2.37																	
2.40																	
2.43																	
2.46																	
2.49																	
2.52																	
2.55																	
2.58																	
2.61																	
2.64																	
2.67																	
2.70																	
2.73																	
2.76																	
2.79																	
2.82																	
2.85																	
2.88																	
2.91																	
2.94																	
2.97																	
3.00																	
3.03																	
3.06																	

DRILLCORE LOG		Date drilled	21/07/2022
SITE:		Core material logged by	15/07/2023
LOCATION:		Core material logged by	Fredrik Åhn
HOLE NUMBER:		Coordinates	
HOLE SECTION (from-to, m)		Hole inclination	5
		Hole direction	N148

Equation variables
 $l =$ 15,000 cm
 $r_w =$ 3,800 cm
Hydrostatic pressure = 96,000 kpa

Bore hole section [m]	CORE PHOTO	ROCK TYPE	ROCK JOINT DATA				WATER PRESSURE TESTING				Estimations																																																																																
			NUMBER OF JOINTS (m)	JOINT SPACING [m]	Joint type	JRC	COATING FILLING	Comments	SECTION MEASURED	WATER FLOW RATE STATIONARY [ml/min]	PUMPING PRESSURE [kPa]	Pumping Head Δh [m]	Moye's equation Section transmissivity [m ² /s]	Cubic law Joint hydr aperture [mm]	Govatsafoen's equation Section transmissivity [m ² /s]	Cubic law Joint hydr aperture [mm]																																																																											
0.00		Drammen granitt	95	3	blasted?		looks fresh	0,2	1,275	48	4,8	1,18365E-06	0,242	5,6744E-07	0,226																																																																												
0.03								blasted or extraction	looks fresh	0,35	3,416	83	124	170	1,17092E-05	0,520	1,49898E-06	0,262																																																																									
0.06																			blasted or extraction	looks fresh	0,43	5,551	124	170	4,25555E-06	0,371	1,51405E-06	0,263																																																															
0.09																													blasted or extraction	rough and fresh	0,7	0,769	422	521	1,49639E-07	0,122	1,22305E-07	0,114																																																					
0.12																																							blasted or extraction	rough and fresh	0,58	3,85	422	521	5,26255E-07	0,185	4,30128E-07	0,173																																											
0.15																																																	blasted or extraction	rough and fresh	0,85	6,303	521	521	6,60863E-07	0,199	5,40149E-07	0,186																																	
0.18																																																											non geological	for stress measurement	0,7	0	325	625	0	0,000	0	0,000																							
0.21																																																																					non geological	for stress measurement	0,85	0	325	625	0	0,000	0	0,000													
0.24																																																																															non geological	for stress measurement	0,85	0	325	625	0	0,000	0	0,000			
0.27																																																																																									non geological	for stress measurement	0,85
0.30	non geological	for stress measurement	0,85	0	325	625	0																																																																																				
0.33								non geological	for stress measurement	0,85	0	325	625	0	0,000	0	0,000																																																																										
0.36																		non geological	for stress measurement	0,85	0	325	625	0	0,000	0	0,000																																																																
0.39																												non geological	for stress measurement	0,85	0	325	625	0	0,000	0	0,000																																																						
0.42																																						non geological	for stress measurement	0,85	0	325	625	0	0,000	0	0,000																																												
0.45																																																non geological	for stress measurement	0,85	0	325	625	0	0,000	0	0,000																																		
0.48																																																										non geological	for stress measurement	0,85	0	325	625	0	0,000	0	0,000																								
0.51																																																																				non geological	for stress measurement	0,85	0	325	625	0	0,000	0	0,000														
0.54																																																																														non geological	for stress measurement	0,85	0	325	625	0	0,000	0	0,000				
0.57																																																																																								non geological	for stress measurement	0,85	0
0.60	non geological	for stress measurement	0,85	0	325	625	0																																																																																				
0.63								non geological	for stress measurement	0,85	0	325	625	0	0,000	0	0,000																																																																										
0.66																		non geological	for stress measurement	0,85	0	325	625	0	0,000	0	0,000																																																																
0.69																												non geological	for stress measurement	0,85	0	325	625	0	0,000	0	0,000																																																						
0.72																																						non geological	for stress measurement	0,85	0	325	625	0	0,000	0	0,000																																												
0.75																																																non geological	for stress measurement	0,85	0	325	625	0	0,000	0	0,000																																		
0.78																																																										non geological	for stress measurement	0,85	0	325	625	0	0,000	0	0,000																								
0.81																																																																				non geological	for stress measurement	0,85	0	325	625	0	0,000	0	0,000														
0.84																																																																														non geological	for stress measurement	0,85	0	325	625	0	0,000	0	0,000				
0.87																																																																																								non geological	for stress measurement	0,85	0
0.90	non geological	for stress measurement	0,85	0	325	625	0																																																																																				
0.93								non geological	for stress measurement	0,85	0	325	625	0	0,000	0	0,000																																																																										
0.96																		non geological	for stress measurement	0,85	0	325	625	0	0,000	0	0,000																																																																
0.99																												non geological	for stress measurement	0,85	0	325	625	0	0,000	0	0,000																																																						
1.02																																						non geological	for stress measurement	0,85	0	325	625	0	0,000	0	0,000																																												
1.05																																																non geological	for stress measurement	0,85	0	325	625	0	0,000	0	0,000																																		
1.08																																																										non geological	for stress measurement	0,85	0	325	625	0	0,000	0	0,000																								
1.11																																																																				non geological	for stress measurement	0,85	0	325	625	0	0,000	0	0,000														
1.14																																																																														non geological	for stress measurement	0,85	0	325	625	0	0,000	0	0,000				
1.17																																																																																								non geological	for stress measurement	0,85	0
1.20	non geological	for stress measurement	0,85	0	325	625	0																																																																																				
1.23								non geological	for stress measurement	0,85	0	325	625	0	0,000	0	0,000																																																																										
1.26																		non geological	for stress measurement	0,85	0	325	625	0	0,000	0	0,000																																																																
1.29																												non geological	for stress measurement	0,85	0	325	625	0	0,000	0	0,000																																																						
1.32																																						non geological	for stress measurement	0,85	0	325	625	0	0,000	0	0,000																																												
1.35																																																non geological	for stress measurement	0,85	0	325	625	0	0,000	0	0,000																																		
1.38																																																										non geological	for stress measurement	0,85	0	325	625	0	0,000	0	0,000																								
1.41																																																																				non geological	for stress measurement	0,85	0	325	625	0	0,000	0	0,000														
1.44																																																																														non geological	for stress measurement	0,85	0	325	625	0	0,000	0	0,000				
1.47																																																																																								non geological	for stress measurement	0,85	0
1.50	non geological	for stress measurement	0,85	0	325	625	0																																																																																				
1.53								non geological	for stress measurement	0,85	0	325	625	0	0,000	0	0,000																																																																										
1.56																		non geological	for stress measurement	0,85	0	325	625	0	0,000	0	0,000																																																																
1.59																												non geological	for stress measurement	0,85	0	325	625	0	0,000	0	0,000																																																						
1.62																																						non geological	for stress measurement	0,85	0	325	625	0	0,000	0	0,000																																												
1.65																																																non geological	for stress measurement	0,85	0	325	625	0	0,000	0	0,000																																		
1.68																																																										non geological	for stress measurement	0,85	0	325	625	0	0,000	0	0,000																								
1.71																																																																				non geological	for stress measurement	0,85	0	325	625	0	0,000	0	0,000														
1.74																																																																														non geological	for stress measurement	0,85	0	325	625	0	0,000	0	0,000				
1.77																																																																																								non geological	for stress measurement	0,85	0
1.80	non geological	for stress measurement	0,85	0	325	625	0																																																																																				
1.83								non geological	for stress measurement	0,85	0	325	625	0	0,000	0	0,000																																																																										
1.86																		non geological	for stress measurement	0,85	0	325	625	0	0,000	0	0,000																																																																
1.89																												non geological	for stress measurement	0,85	0	325	625	0	0,000	0	0,000																																																						
1.92																																						non geological	for stress measurement	0,85	0	325	625	0	0,000	0	0,000																																												
1.95																																																non geological	for stress measurement	0,85	0	325	625	0	0,000	0	0,000																																		
1.98																																																										non geological	for stress measurement	0,85	0	325	625	0	0,000	0	0,000																								
2.01																																																																				non geological	for stress measurement	0,85	0	325	625	0	0,000	0	0,000														
2.04																																																																														non geological	for stress measurement	0,85	0	325	625	0	0,000	0	0,000				
2.07																																																																																								non geological	for stress measurement	0,85	0
2.10	non geological	for stress measurement	0,85	0	325	625	0																																																																																				
2.13								non geological	for stress measurement	0,85	0	325	625	0	0,000	0	0,000																																																																										
2.16																		non geological	for stress measurement	0,85	0	325	625	0	0,000	0	0,000																																																																
2.19																												non geological	for stress measurement	0,85	0	325	625	0	0,000	0	0,000																																																						
2.22																																						non geological	for stress measurement	0,85	0	325	625	0	0,000	0	0,000																																												
2.25																																																non geological	for stress measurement	0,85	0	325	625	0	0,000	0	0,000																																		
2.28																																																										non geological	for stress measurement	0,85	0	325	625	0	0,000	0	0,000																								
2.31																																																																				non geological	for stress measurement	0,85	0	325	625	0	0,000	0	0,000														
2.34																																																																														non geological	for stress measurement	0,85	0	325	625	0	0,000	0	0,000				
2.37																																																																																								non geological			

DRILLCORE LOG		Date drilled	15.02.2023
		Core material logged by	Freddie Khan
		Coordinates	
SITE:	Hestnestunnelelen	Hole inclination	0
LOCATION:	Crosscut	Hole direction	120
HOLE NUMBER:	BH6		
HOLE SECTION (from-to, m)	0-3.2		

Joint types	Explanation	Equation variables		
Rock joint	Nature occurring joint	L =	15,000	cm
ist-id1	Rock joint sets	r_w =	3,100	cm
Foliation	Joint from foliation	Hydrostatic pressure =	300,000	kpa
Blasting induced	From blasting			
Core drilling	Core damage related to Core drilling			

Bore hole section [m]	CORE PHOTO	ROCK TYPE/PHOTO	RQD	ROCK JOINT DATA					WATER PRESSURE TESTING				Estimations						
				NUMBER OF JOINTS / m	JOINT SPACING [m]	Joint type	JRC	Jr	COATING FILLING [μ]	Comments	SECTION MEASURED [m]	WATER FLOW RATE STATIONARY [l/min]	PUMPING PRESSURE [kPa]	Pumping Head Δh [m]	Moye's equation TRANSMISSIVITY [m ² /s]	Cubic law Joint hydr aperture [m]	Gustafson's equation Joint transmissivity [m ² /s]		
0.00		augen gneiss amphibolite	77	2	Core drilling				fresh										
0.03																			
0.06																			
0.09																			
0.12																			
0.15																			
0.18																			
0.21																			
0.24																			
0.27																			
0.30																			
0.33																			
0.36																			
0.39																			
0.42																			
0.45																			
0.48																			
0.51																			
0.54																			
0.57																			
0.60																			
0.63																			
0.66																			
0.69																			
0.72																			
0.75																			
0.78																			
0.81																			
0.84																			
0.87																			
0.90																			
0.93																			
0.96																			
0.99																			
1.02																			
1.05																			
1.08																			
1.11																			
1.14																			
1.17																			
1.20																			
1.23																			
1.26																			
1.29																			
1.32																			
1.35																			
1.38																			
1.41																			
1.44																			
1.47																			
1.50																			
1.53																			
1.56																			
1.59																			
1.62																			
1.65																			
1.68																			
1.71																			
1.74																			
1.77																			
1.80																			
1.83																			
1.86																			
1.89																			
1.92																			
1.95																			
1.98																			
2.01																			
2.04																			
2.07																			
2.10																			
2.13																			
2.16																			
2.19																			
2.22																			
2.25																			
2.28																			
2.31																			
2.34																			
2.37																			
2.40																			
2.43																			
2.46																			
2.49																			
2.52																			
2.55																			
2.58																			
2.61																			
2.64																			
2.67																			
2.70																			
2.73																			
2.76																			
2.79																			
2.82																			
2.85																			
2.88																			
2.91																			
2.94																			
2.97																			
3.00																			
3.03																			
3.06																			
3.09																			
3.12																			
3.15																			
3.18																			
3.21																			
3.24																			
3.27																			
3.30																			
3.33																			
3.36																			
3.39																			
3.42																			
3.45																			

F LABORATORY RESULTS - ROCK MECHANICAL TESTING

Tilt testing

Table F.1: Results from the tilt testing

Specimen	Tilt angle (α)					Median	std (+/-)
A1	27.7	26.5	26.5	27.6	29.20	27.6	
A2	27.1	30.7	31.8	32	33.20	31.8	
A3	27.4	24.5	26.5	29.8	26.5	26.5	
						27.6	2.4
B1	30	34.3	32.8	34.1	32.1	32.8	
B2	29.3	32	27.5	28.5	27.6	28.5	
B3	27.3	34.4	29.3	32.3	31.8	31.8	
						31.8	2.5

